

Cite this: *Chem. Sci.*, 2023, 14, 13629

# Cu-based catalyst designs in CO<sub>2</sub> electroreduction: precise modulation of reaction intermediates for high-value chemical generation

Liangyiqun Xie,<sup>b</sup> Yujing Jiang,<sup>c</sup> Wenlei Zhu,<sup>c</sup> Shichao Ding,<sup>d</sup> Yang Zhou<sup>\*a</sup> and Jun-Jie Zhu<sup>id</sup><sup>\*b</sup>

The massive emission of excess greenhouse gases (mainly CO<sub>2</sub>) have an irreversible impact on the Earth's ecology. Electrocatalytic CO<sub>2</sub> reduction (ECR), a technique that utilizes renewable energy sources to create highly reduced chemicals (e.g. C<sub>2</sub>H<sub>4</sub>, C<sub>2</sub>H<sub>5</sub>OH), has attracted significant attention in the science community. Cu-based catalysts have emerged as promising candidates for ECR, particularly in producing multi-carbon products that hold substantial value in modern industries. The formation of multi-carbon products involves a range of transient intermediates, the behaviour of which critically influences the reaction pathway and product distribution. Consequently, achieving desirable products necessitates precise regulation of these intermediates. This review explores state-of-the-art designs of Cu-based catalysts, classified into three categories based on the different prospects of the intermediates' modulation: heteroatom doping, morphological structure engineering, and local catalytic environment engineering. These catalyst designs enable efficient multi-carbon generation in ECR by effectively modulating reaction intermediates.

Received 20th August 2023  
Accepted 13th October 2023

DOI: 10.1039/d3sc04353c

rsc.li/chemical-science

## 1. Introduction

The excessive emission of greenhouse gases has resulted in various environmental degradations, posing a significant threat to the delicate balance of Earth's ecosystem.<sup>1-4</sup> Among these greenhouse gases, CO<sub>2</sub> is the primary constituent responsible for the majority of environmental issues.<sup>5-7</sup> Consequently, the scientific community has set its sights on reducing CO<sub>2</sub> emissions and transforming excessive CO<sub>2</sub> into high-value chemicals.<sup>8-17</sup> Over the past few decades, scientists have diligently pursued the development of advanced technologies that enable the environmentally friendly conversion of CO<sub>2</sub> into

<sup>a</sup>State Key Laboratory for Organic Electronics and Information Displays & Institute of Advanced Materials IAM, Nanjing University of Posts & Telecommunications, Nanjing, 210023, China. E-mail: iamyangzhou@njupt.edu.cn

<sup>b</sup>State Key Laboratory of Analytical Chemistry for Life Science, School of Chemistry and Chemical Engineering, Nanjing University, Nanjing, 210023, China. E-mail: jjzhu@nju.edu.cn

<sup>c</sup>State Key Laboratory of Pollution Control and Resource Reuse, The Frontiers Science Center for Critical Earth Material Cycling, School of the Environment, Nanjing University, Nanjing, 210023, China

<sup>d</sup>Department of Nanoengineering, University of California, La Jolla, San Diego, CA 92093, USA



Liangyiqun Xie

Liangyiqun Xie received her bachelor's degree in Analytical Chemistry from East China University of Science and Technology in 2021. Now she is a direct PhD student at Nanjing University under the supervision of Prof. Jun-Jie Zhu. Her research focuses on catalyst preparation and the investigation of catalytic mechanisms for electrocatalytic CO<sub>2</sub> reduction.



Yujing Jiang

Yujing Jiang received her doctorate degree from Nanjing University in 2022, under the guidance of Prof. Liping Jiang. She is currently a postdoctoral researcher in Professor Wenlei Zhu's research group. Her research interests concern the preparation of functional nanomaterials and their applications in microbial electrochemical systems.



valuable chemical products.<sup>18–28</sup> With the utilization of renewable energy sources, ECR has emerged as a promising avenue for converting CO<sub>2</sub> into value-added multi-carbon products, facilitating the attainment of carbon neutrality (Fig. 1).<sup>29–35</sup>

Conventional ECR experiments typically involve an electrolytic cell divided into two primary sections: the working electrode section (cathode) where CO<sub>2</sub> is reduced, and the counter electrode section (anode) where the O<sub>2</sub> oxidation reaction occurs. These sections are separated by an ion exchange membrane, which effectively prevents the cathode products from migrating to the anode and undergoing oxidation. Moreover, the ion exchange membrane facilitates the charge balance of the electrolytic system.<sup>36</sup> One commonly employed ECR device is the H-cell, where CO<sub>2</sub> gas must traverse the cathode electrolyte. In this configuration, CO<sub>2</sub> gas exists as carbonate and other ionic forms, migrating toward the cathode surface. However, the solubility of CO<sub>2</sub> in typical aqueous electrolytes is approximately 10<sup>-3</sup>–10<sup>-2</sup> M; such low CO<sub>2</sub> concentrations restrict the reaction rate within the H-cell and hinder efficient CO<sub>2</sub> conversion. To address this limitation, a Kenis-type structured electrolytic device has been developed to mitigate the

hindering effect of the electrolyte on CO<sub>2</sub>. These electrolyser devices comprise an anode, a gas diffusion electrode (GDE) serving as the cathode, and an ion exchange membrane (Fig. 2a). In these electrolyser systems, CO<sub>2</sub> gas rapidly diffuses through a thin GDE layer and undergoes reduction at the gas-liquid-solid three-phase interface.<sup>37</sup>

The liquid-phase electrolyser, also known as the flow cell, enhances CO<sub>2</sub> conversion efficiency by adjusting the flow rate of the electrolyte fluids (Fig. 2b). The gas-phase electrolyser prevents electrolyte penetration into the GDE and improves the stability of the catalytic system (Fig. 2c). Notably, the diffusion distance of CO<sub>2</sub> from the GDE to the catalyst surface in the flow cell (50 nm) is approximately three orders of magnitude shorter than that in the H-cell (30–60 μm).<sup>38–40</sup> This reduced distance reduces CO<sub>2</sub> solubility in the aqueous electrolyte, enabling greater absorption of CO<sub>2</sub> into the catalyst and subsequent reduction into multi-carbon products. Moreover, incorporating the GDE layer significantly enhances the catalytic current density, which surpasses 100 mA cm<sup>-2</sup> at the surface level compared to using the H-cell. Various methods, such as air-brushing, drop casting, or electrodeposition, can be used to



Wenlei Zhu

*Wenlei Zhu has been a professor at the School of the Environment in Nanjing University since 2021. He graduated from Brown University in 2015, with a PhD degree in chemistry. His research interests include the synthesis of nanomaterials, photo/electrochemical analytical methods, and carbon neutrality related applications.*



Yang Zhou

*Professor Yang Zhou received her PhD from Washington University in St. Louis in 2017. She has been a Professor at Nanjing University of Posts & Telecommunications since 2021. Her research is mainly focused on physical chemistry, surface chemistry and green chemistry.*



Shichao Ding

*Shichao Ding received his PhD degree from Washington State University in 2022. Now he is a postdoctoral researcher at the University of California San Diego. His current research interests focus on designing functional nanomaterials for catalysis, sensing, and wearable electronics. He has published over 60 peer-reviewed papers in high-impact journals.*



Jun-Jie Zhu

*Jun-Jie Zhu is a full professor at Nanjing University. He obtained his PhD degree at the same university. He served as a post-doctoral fellow at Bar Ilan University, Israel. His research work focuses on Nano Science and Analytical Chemistry including nanobioanalytical chemistry, nanobioelectrochemistry, optical analysis of nanomaterials, bio-application of nanomaterials, cell, DNA, and biomarker analysis etc. He was named in Elsevier's annual list of China's Most Cited Researchers in chemistry for the years 2014–2022. He serves as an associate editor of "Analyst", "Biosensors", "Frontiers in Sensors" and "Current Smart Materials".*





Fig. 1 Schematic illustration of Cu-based catalyst engineering for improving the ECR performance.



Fig. 2 (a) Schematic diagram of a gas diffusion electrode. (b) Schematic diagram and cross-sectional view of a liquid phase electrolyser. (c) Schematic diagram and cross-sectional view of a gas phase electrolyser. Reproduced from ref. 36. Copyright 2021 Wiley-VCH.

apply the catalyst onto the GDE layer. Gas phase products are analysed by Gas Chromatography (GC), while the liquid phase products obtained from the cathode layer can be analysed *via*

techniques such as Nuclear Magnetic Resonance (NMR) or Liquid Chromatography-Mass Spectrometry (LC-MS).

However, the high energy input, intense competition from the hydrogen evolution reaction (HER), and poor product selectivity significantly hinder the efficiency of CO<sub>2</sub> conversion in the ECR process. Therefore, researchers consistently tried to seek high-performance electrocatalysts that can enhance catalyst activity and selectivity. In 1985, Hori and colleagues made a ground-breaking discovery by demonstrating that metal electrodes can efficiently reduce CO<sub>2</sub> to various products, including CO and hydrocarbons.<sup>41</sup> Since then, extensive investigations have been conducted to explore the properties of different catalysts and optimize their performance. Currently, Cu-based catalysts stand out as prominent candidates due to their moderate absorption capability for \*C<sub>1</sub> intermediates and their ability to couple two adjacent \*C<sub>1</sub>.<sup>42–44</sup> Moreover, they hold greater application potential compared to other C<sub>1</sub>-produced catalysts such as Au and Ag, which primarily yield CO.<sup>45</sup> Over the past three decades, significant research efforts have been dedicated to Cu-based catalysts in ECR, leading to innovative developments in catalytic devices, product monitoring methods, and optimal catalyst design.

The CO<sub>2</sub> electroreduction process is a complex surface chemical process that involves multiple intermediates whose behavior cannot be fully described through theoretical calculations or simulations alone.

As a result, an increasing variety of *in situ* characterization instruments are being employed to monitor these intermediates visually.<sup>46</sup> Techniques such as time-resolved Attenuated Total Reflectance-Surface Enhanced Infrared Absorption Spectroscopy (ATR-SEIRAS),<sup>47</sup> *in situ* Raman Spectroscopy,<sup>48–51</sup> *in situ* X-ray Absorption Spectroscopy (XAS),<sup>52</sup> *operando* Electrochemical Scanning Transmission Electron Microscopy (EC-



STEM),<sup>53</sup> and other tools are used to observe the behavioural trajectories of intermediates.<sup>54</sup> Detecting catalyst surface dynamics through these techniques provides an objective scientific basis for the construction of catalyst structures.<sup>55</sup> Noteworthy intermediates detected using the aforementioned techniques include \*CO,<sup>56,57</sup> :\*CO,<sup>58,59</sup> \*CHO,<sup>60</sup> \*COOH (HCOO\*),<sup>49</sup> \*OCCO, \*COCHO and \*CH<sub>3</sub>CHO.<sup>61</sup> These intermediates give rise to various products such as CO,<sup>58</sup> CH<sub>4</sub>,<sup>62,63</sup> HCHO,<sup>64</sup> HCOOH,<sup>65,66</sup> C<sub>2</sub>H<sub>4</sub>,<sup>58,67</sup> CH<sub>3</sub>COOH,<sup>68</sup> C<sub>2</sub>H<sub>5</sub>OH,<sup>69</sup> C<sub>3</sub>H<sub>7</sub>OH,<sup>70</sup> CH<sub>3</sub>COCH<sub>3</sub> (ref. 71) *etc.* The rational design of Cu-based catalysts plays a crucial role in determining the behaviour of reaction intermediates,<sup>72–74</sup> which, in turn, influences the selectivity of multi-carbon products.

Evaluating different catalyst designs for controlling reaction intermediates is highly reliant on the adsorption and desorption energies of specific intermediates at catalytic sites. Heteroatom doping comprises strategies that directly modify the structural properties of active sites, thereby affecting the interaction strength between these sites and reaction intermediates. While morphological structure engineering doesn't alter the composition or properties of catalytic active sites, it does control the spatial arrangement of these sites on a macroscopic scale, subsequently regulating the adsorption energies and retention time of reaction intermediates, leading to the production of high-value products. Moreover, localized catalytic environmental engineering indirectly impacts the interaction of specific sensitive intermediates with active sites by modifying the catalytic environment surrounding these sites from a holistic perspective, including factors like the acidity or alkalinity of the catalytic electrolyte, and reactant coverage. Based on these various perspectives for controlling the interaction strength of intermediates at catalytic sites, we categorize these strategies into three primary groups and arrange them accordingly.

This review begins with a systematic description of catalyst evaluation parameters and recognized reaction mechanisms in ECR. To address different modification targets, the latest Cu-based catalyst designs for modulating intermediates are categorized into three groups: heteroatom doping engineering, encompassing metallic and non-metallic heteroatom doping; morphological structure engineering, involving grain boundary effects, geometric confinement of pores, hierarchical structures, facets, defects, and chemical state effects; and local catalytic environment engineering, including tandem catalyst effects, substrate effects, surface additive effects, coverage effects, and local electrolyte environment effects. This article thoroughly analyses the challenges faced by existing ECR systems and offers novel insights into the design of Cu-based catalysts for regulating the behaviour of intermediates.

## 2. Basic outline of electrocatalytic CO<sub>2</sub> reduction

### 2.1. Evaluation parameters for electrocatalytic CO<sub>2</sub> reduction

The electrocatalytic reduction of CO<sub>2</sub> to fuels and feedstocks presents a promising avenue for converting renewable

electricity into chemical energy for storage. However, the catalytic performance of ECR can be influenced by various factors, including the catalyst type, electrolyte selection, reactant delivery method, and catalytic equipment design. Among these factors, the catalyst properties play a paramount role. To comprehensively evaluate the performance of an electrocatalytic system, several experimental parameters are commonly employed. Key parameters encompassing overpotential, current density, faradaic efficiency, Tafel slope, and others hold significant importance and are widely utilized.

**2.1.1 Overpotential.** The onset potential refers to the experimentally determined potential at which the formation of a product initiates during electrocatalytic CO<sub>2</sub> reduction (ECR). Typically, it is lower than the standard reduction potential of CO<sub>2</sub> due to kinetic hysteresis in the reaction. The disparity between these values is known as the overpotential, denoted as  $\eta$ , and can be mathematically expressed as follows (eqn (1)):

$$\eta = E - E_{\text{eq}} \quad (1)$$

Here,  $E$  represents the onset potential of the product measured in the experiment, while  $E_{\text{eq}}$  denotes the standard reduction potential of that product under the given experimental conditions. The Cu<sub>2</sub>S<sub>1-x</sub> catalyst with abundant Cu<sup>δ+</sup> ( $0 < \delta < 1$ ) species exhibited an exceptionally low overpotential ( $\eta$ ) of 0.19 V. This overpotential represents the disparity between the theoretical potential for ethanol electrosynthesis (0.09 V vs. RHE) and the onset potential (-0.1 V vs. RHE). The diminutive overpotential further illustrates the catalyst's ability to facilitate C<sub>2</sub>H<sub>5</sub>OH production from CO<sub>2</sub> with minimal energy input.<sup>75</sup>

**2.1.2 Current density.** Current density ( $j$ ) is a pivotal parameter in CO<sub>2</sub> electrocatalysis, signifying the number of electrons that traverse the electrode surface within a given time frame. Typically,  $j$  is normalized to the catalyst's surface area or mass. Additionally,  $j$  provides insights into the rate of CO<sub>2</sub> reduction.

**2.1.3 Faradaic efficiency (FE).** Faradaic efficiency (FE) serves as a direct indicator of product selectivity in CO<sub>2</sub> electrocatalysis and can be mathematically expressed through eqn (2):

$$\epsilon_{\text{faradaic}} = \frac{\alpha n F}{Q} \quad (2)$$

In this equation,  $\alpha$  represents the number of electrons transferred to produce a specific product. For instance, when reducing CO<sub>2</sub> to CO, 2 electrons are required, thus  $\alpha$  is 2. Meanwhile,  $n$  denotes the molar amount of the obtained product,  $F$  represents the faradaic constant with a value of 96 485 C mol<sup>-1</sup>, and  $Q$  signifies the total amount of charge transferred.

Moreover, a relationship exists between the partial current density of a product and its corresponding FE, as depicted by eqn (3):

$$j_{\text{partial}} = \epsilon_{\text{faradaic}} \times j \quad (3)$$



Here,  $j_{\text{partial}}$  refers to the partial current density of the product, which is obtained by multiplying the total current  $j$  by the respective FE.

**2.1.4 Tafel slope.** The Tafel slope ( $b$ ) serves as an empirical parameter derived from the Butler–Volmer equation, which characterizes the kinetics of electron transfer in electrocatalysis. It can be determined by plotting the reaction potential against the logarithm of the partial current density of a product, with  $b$  representing the slope of the linear region. The Tafel slope indicates the increase in overpotential required to achieve a specific current density. Generally, a smaller Tafel slope implies faster electrocatalytic reaction kinetics and superior catalytic performance. Furthermore, the Tafel slope reflects the rate-determining step in the formation of desired products. For instance, a Tafel slope of  $59 \text{ mV dec}^{-1}$  suggests that the rate-determining step does not involve electron transfer, and only one electron is transferred in all preceding steps. Conversely, a Tafel slope of  $116 \text{ mV dec}^{-1}$  indicates that the rate-determining step is a single electron transfer, with no electron transfer occurring before this step. The Tafel equation can be expressed as follows:

$$\eta = a + b \log |j| \quad (4)$$

In this equation,  $\eta$  represents the overpotential,  $a$  is a constant, and  $j$  signifies the current density. Zheng *et al.* demonstrated a progressive decrease in the CO Tafel slope (from  $244$  to  $146 \text{ mV dec}^{-1}$ ) and  $\text{C}_2\text{H}_4$  Tafel slope (from  $104$  to  $35 \text{ mV dec}^{-1}$ ), indicating a gradual slowdown in  $\text{CO}_2\text{RR}$  electrocatalytic kinetics.<sup>76</sup> Moreover, as Tafel slope values reveal the rate-determining step of the catalytic reaction, we can discern the evolution of the reaction mechanism through these changing slopes. In contrast, Surendranath *et al.* observed a  $\text{C}_2\text{H}_4$  Tafel slope of  $27 \text{ mV dec}^{-1}$  in aprotic solvents, signifying a markedly distinct reaction mechanism characterized by a quasi-equilibrium PCET step compared to that in protic solvents.<sup>77</sup>

**2.1.5 Other parameters.** In addition to the previously mentioned parameters, there exist other parameters that are not extensively utilized but can be used to assess catalytic systems from unconventional perspectives. For instance, the electrochemically active surface area (ECSA) reflects the surface structural characteristics of the catalyst, and is derived from double-layer capacitance ( $C_{\text{dl}}$ ) measurements. Typically, ECSA serves as a metric for assessing the exposure of active sites on the catalyst surface. Consequently, ECSA values within an appropriate range tend to exhibit a positive correlation with  $\text{CO}_2$  electrocatalytic performance.<sup>78,79</sup> The construction of a highly porous and rough catalyst surface morphology can lead to an increase in ECSA.<sup>80</sup> Occasionally, to investigate the specific influence of a non-electrochemically active area factor, the ECSA values of both the experimental and control groups are adjusted in a manner nearly identical to control the active site variables.<sup>70,81</sup> The turnover number (TON), representing the product yield per unit catalyst, and turnover frequency (TOF), representing the product yield per unit catalyst over a specific time period, are additional parameters that can offer insights into

catalyst utilization and stability. These two physical parameters are commonly employed to assess both the catalytic performance and the visible light harvesting capacity of catalysts in photocatalytic systems.<sup>82</sup> Han *et al.* developed an effective photosensitizer for  $\text{CO}_2$  reduction by directly coordinating redox-active metal centers with natural organic dyes. For instance, the CuPP/FeTDHPP system achieves more than  $16\,100$  turnovers of CO with a maximum TOF of  $7650 \text{ h}^{-1}$ , surpassing a reported  $\text{Ir}(\text{ppy})_3/\text{FeTDHPP}$  system (TON =  $140$  in  $55 \text{ h}$ ) by two orders of magnitude, demonstrating exceptional photocatalytic activity in  $\text{CO}_2$  reduction.<sup>83</sup> TON/TOF is also employed to assess product formation rates in specific electrocatalytic systems utilizing molecular catalysts. Buonsanti *et al.* developed a tandem catalyst,  $\text{Cu}_{\text{cub}}/\text{Fe-Por}$ , consisting of the CO-producing component iron porphyrin (Fe-Por) and Cu nanocubes ( $\text{Cu}_{\text{cub}}$ ). This tandem catalyst displayed an approximately 22-fold increase in  $\text{C}_2\text{H}_4$  selectivity compared to pristine  $\text{Cu}_{\text{cub}}$ , which was attributed to the integration of molecular catalysts with tuneable  $\text{TOF}_{\text{CO}}$ .<sup>84</sup> It is crucial to apply diverse evaluation parameters judiciously, considering various aspects, to comprehensively characterize the catalytic effect of the catalyst from different dimensions.

## 2.2. Possible mechanisms in $\text{CO}_2$ electroreduction

Chemical reactions occurring on the metal surface involve three fundamental steps: (1) the physical or chemical adsorption of reactants onto the surface; (2) the catalytic transformation on the surface; and (3) the desorption from the surface and formation of the product.<sup>85</sup> In the case of multi-carbon products derived from  $\text{CO}_2$  electrocatalysis, the reactions taking place on the catalyst surface are highly intricate and diverse. The resulting reaction intermediates span from common  $\text{C}_1$  intermediates like  $^*\text{CO}$ ,  $^*\text{CHO}$ , and  $^*\text{COOH}$  to recognized  $\text{C}_2$  intermediates such as  $^*\text{C}_2\text{O}_2$ ,<sup>86</sup>  $^*\text{COCO}$ ,  $^*\text{CH}_2\text{OH}$ <sup>87</sup> and others. These intermediates evolve from the fundamental  $^*\text{CO}$  generated during the earlier electrolysis of  $\text{CO}_2$ . Metals such as Au or Ag exhibit weak absorption towards  $^*\text{CO}$  and  $^*\text{H}$ , favouring the desorption of  $^*\text{CO}$  and consequently promoting the generation of CO rather than multi-carbon products. In contrast, metals like Pt or Fe, which excessively adsorb  $^*\text{CO}$  and  $^*\text{H}$ , tend to compete with  $\text{CO}_2$  electroreduction through intense HER. Therefore, when compared to other metals, only Cu exhibits the ability to produce a wide array of hydrocarbon products. This is due to its affinity for  $^*\text{CO}$  and  $^*\text{H}$  adsorption, striking a balance between preserving active site functionality and enabling the intermediates' facile desorption from the catalyst surface.<sup>88</sup> Based on the preceding analysis, controlling the quantity and distribution of catalytic active sites that can enrich  $^*\text{CO}$  can significantly enhance the catalyst's selectivity for the desired products.

**2.2.1 Reaction mechanism of  $\text{C}_1$  products.** The initial stage in the generation of  $\text{C}_1$  products involves the adsorption and activation of a  $\text{CO}_2$  molecule on the catalyst surface, resulting in a bent state denoted as  $^*\text{CO}_2^-$ . Subsequently,  $^*\text{CO}_2^-$  can undergo hydrogenation to yield either  $^*\text{COOH}$  or  $^*\text{OOCH}$ , which can further convert to  $\text{HCOOH}$  or  $\text{CO}$ , respectively. The



latter transformation entails the dehydrogenation of  $^*\text{COOH}$ .<sup>89</sup> These products, namely  $\text{H}_2$ ,  $\text{HCOOH}$ , and  $\text{CO}$ , dominate at lower negative potentials due to the simplicity of the reduction process and the small number of electron transfers required. According to the Computational Hydrogen Electrode (CHE) model proposed by the Nørskov group,<sup>85</sup> the crucial step for the formation of  $\text{CH}_4$  and other higher-order hydrocarbons is the hydrogenation of  $^*\text{CO}$  to  $^*\text{CHO}$ , which occurs at  $-0.74$  V vs. RHE. This suggests that a more negative potential favours the production of products derived from  $^*\text{CHO}$ . Subsequently,  $^*\text{CHO}$  can be further reduced to  $^*\text{CH}_2\text{O}$  and  $^*\text{CH}_3\text{O}$ , leading to the production of  $\text{CH}_4$ . Notably, a small amount of  $\text{CH}_3\text{OH}$  is also generated during this process, however, its thermodynamic stability is comparatively lower than that of other  $\text{C}_1$  products.

**2.2.2 Reaction mechanism of  $\text{C}_{2+}$  products.** The generation of  $\text{C}_{2+}$  products involves the coupling of adsorbed  $^*\text{CO}$  species on the catalyst surface. Comprehending the mechanisms and factors influencing the C–C coupling and hydrogenation processes is pivotal for the rational design of highly active and selective catalysts.<sup>90–92</sup> Hwang *et al.*, using time-resolved Attenuated Total Reflectance-Surface Enhanced Infrared Absorption Spectroscopy (ATR-SEIRAS), observed a kinetically linked dimer intermediate denoted as  $^*\text{OCCO}$ , which they identified as the key intermediate for the generation of  $\text{C}_{2+}$  products.<sup>47</sup> Wang *et al.* proposed a hydrogen-assisted C–C coupling mechanism, wherein adsorbed  $^*\text{CHO}$  couples to form  $\text{OCHCHO}$  over a Cu catalyst modified with fluorine.<sup>93</sup> Head-Gordon *et al.* suggested  $\text{COCHO}$  as another possible intermediate resulting from the coupling of  $^*\text{CO}$  and  $^*\text{CHO}$ , which determines the selectivity between  $\text{C}_2\text{H}_4$  and  $\text{C}_2\text{H}_5\text{OH}$ .<sup>94</sup> Additionally, aside from these conventional intermediates, certain studies have investigated the role of  $\text{CO}(\text{g})$  in the C–C coupling reaction under specific conditions. It has been proposed that  $\text{CO}(\text{g})$  could form unconventional intermediates with  $^*\text{COOH}$  or  $^*\text{CO}/\text{CO}(\text{g})$ , potentially competing with the  $^*\text{OCCO}$  dimerization pathway.<sup>95</sup>

The selectivity of  $\text{C}_{2+}$  products relies on the involvement of intermediates in the C–C coupling and hydrogenation reactions. Various studies have proposed different intermediates, including  $^*\text{OCCO}$ ,<sup>47</sup>  $^*\text{OCHCHO}$ ,<sup>93</sup> and  $^*\text{CO}^*\text{CHO}$ .<sup>92,94</sup> These intermediates originate from proton and electron transfers of  $^*\text{CO}$  or  $^*\text{OCCOH}$ , resulting in various  $\text{C}_2$  products such as  $\text{C}_2\text{H}_4$  and  $\text{C}_2\text{H}_5\text{OH}$ .<sup>86,94</sup> The formation barriers for these products are closely situated, leading to varied production tendencies under different conditions. Another potential intermediate is  $^*\text{CHCOH}$ , derived from the hydrogenation of  $\text{OC}^*\text{COH}$ . Goddard *et al.* suggested that this intermediate is the crucial determinant of the selectivity of  $\text{C}_{2+}$  products.<sup>96</sup> It can either undergo dehydrogenation to form  $\text{CCH}$  and generate  $\text{C}_2\text{H}_4$  or hydrogenation to produce  $^*\text{CHCHOH}$  and form  $\text{C}_2\text{H}_5\text{OH}$  (Fig. 3).

The selectivity between  $\text{C}_2\text{H}_4$  and oxygenated products is influenced by the reaction pathways of different intermediates involved in the C–C coupling and hydrogenation reactions, as well as the microenvironment of the catalyst surface, such as substrate coverage and alkaline conditions in the electrolyte.<sup>92</sup> For instance, Sargent *et al.* discovered that a lower  $\text{CO}$  coverage favoured the dehydrogenation of  $^*\text{OCCO}$  or  $^*\text{OCHCHO}$  to form  $\text{C}_2\text{H}_4$ .<sup>97</sup> Meanwhile, the formation of  $\text{C}_3$  products has been



Fig. 3 Possible C–C coupling mechanisms in the electrocatalytic  $\text{CO}_2$  reduction (above). Mechanisms of forming  $\text{C}_2\text{H}_4$  and  $\text{C}_2\text{H}_5\text{OH}$  after C–C coupling (below). Reproduced from ref. 92. Copyright 2021 Royal Society of Chemistry.

observed on Cu-based catalysts.<sup>98–100</sup> The mechanism of  $\text{C}_3$  formation remains elusive as no  $^*\text{C}_2$  intermediates have been detected through various characterizations. Theoretical calculations have proposed several potential pathways for  $\text{C}_3$  formation.<sup>99,101</sup> For example, Zheng *et al.* demonstrated that double sulphur vacancies on hexagonal CuS (100) planes could serve as active sites for ECR, enabling the stabilization of  $^*\text{CO}$  and  $^*\text{OCCO}$ , leading to the coupling of  $^*\text{CO}$  and  $^*\text{OCCO}$  and the formation of the crucial  $^*\text{C}_3$  intermediate  $\text{CH}_3\text{CH}_2\text{CH}_2\text{OH}$ . The double sulphur vacancy-rich CuS catalyst they synthesized exhibited a faradaic efficiency of  $15.4 \pm 1\%$  for  $\text{CH}_3\text{CH}_2\text{CH}_2\text{OH}$  production.<sup>98</sup> Therefore, a plausible hypothesis for generating  $\text{C}_3$  products is that an adsorbed  $^*\text{CO}$  couples with an adjacent  $^*\text{OCCO}$  to form a  $^*\text{C}_3$  intermediate, which then undergoes proton and electron transfer to yield the final  $\text{C}_3$  product.

The synthesis of a wide range of chemicals and fuels from  $\text{CO}_2$  is a complex process, influenced by several factors, such as the electrolyte environment, applied potential, and, most significantly, the properties of the catalyst. Therefore, the precise and systematic design of catalysts that can effectively manipulate crucial intermediates by extending their residence time or modifying their structural conformation is essential for enhancing selectivity toward desired products. Frequently employed approaches for catalyst modification to control critical carbon-based intermediates encompass, but are not restricted to, the following: (1) fine-tuning the electronic properties of the catalytic active site. (2) Creating unique spatial structures to enhance the concentration of key intermediates. (3) Enhancing microenvironment alkalinity to suppress competition for hydrogen precipitation. (4) Adjusting the local  $\text{CO}^*$  concentration by varying the reactant concentration. These approaches correspond to the modulation of specific



intermediates in the aforementioned reaction mechanisms, either directly or indirectly, resulting in improved selectivity for multi-carbon target compounds.

### 3. Heteroatom doping engineering

Among the current state-of-the-art approaches for designing Cu-based catalysts capable of modulating intermediates, heteroatom doping stands out as the most effective strategy. Heteroatom doping brings about selective alterations in the electronic and geometrical structure of the catalyst surface. These modifications in the electronic structure impact the binding strength of reaction intermediates, while changes in the geometrical structure influence the exposure of active sites to intermediates.<sup>102–104</sup> Consequently, composite catalysts exhibit distinct catalytic properties when compared to their mono-metallic counterparts.<sup>67,105</sup> This section classifies heteroatom doping into two subcategories based on the type of heteroatom: metallic heteroatom doping and non-metallic heteroatom doping (Table 1).

#### 3.1. Metallic heteroatom doping

Alloying, the practice of introducing an additional metal atom into a Cu-based catalyst, is a commonly employed strategy for

designing catalysts that can harness the synergistic effects of multiple metals. The lattice mismatches between Cu and the alloying metal can induce strain at the interface, consequently influencing the binding energy barriers of carbonate intermediates on the catalyst surface. The geometric and electronic properties of the catalyst are contingent upon the type and quantity of doped metal atoms, making alloying one of the most direct and widespread catalyst design approaches for modulating intermediates.<sup>102</sup>

Through metallic heteroatom doping, electron transfer occurs at the interface due to the difference in electronegativity between the two metals. This leads to varied binding energies for essential intermediates involved in the formation of C<sub>2+</sub> products. For instance, Xiong *et al.* successfully doped amorphous CuTi alloy (a-CuTi@Cu) with coordinatively unsaturated Cu to produce C<sub>2–4</sub> products. Theoretical simulations and *in situ* characterization demonstrated that subsurface Ti transfers electrons to Cu, enhancing the affinity for \*CO and lowering the reaction barrier energies of \*CO dimerization and trimerization (Fig. 4a).<sup>106</sup> Metallic heteroatom doping not only facilitates electron transfer but also modifies the electronic environment of the entire catalyst. For instance, doping mesopore-rich Cu oxide nanofibers (Cu–Al MONFs) with Al significantly improved the electrocatalytic performance in CO<sub>2</sub> electroreduction to

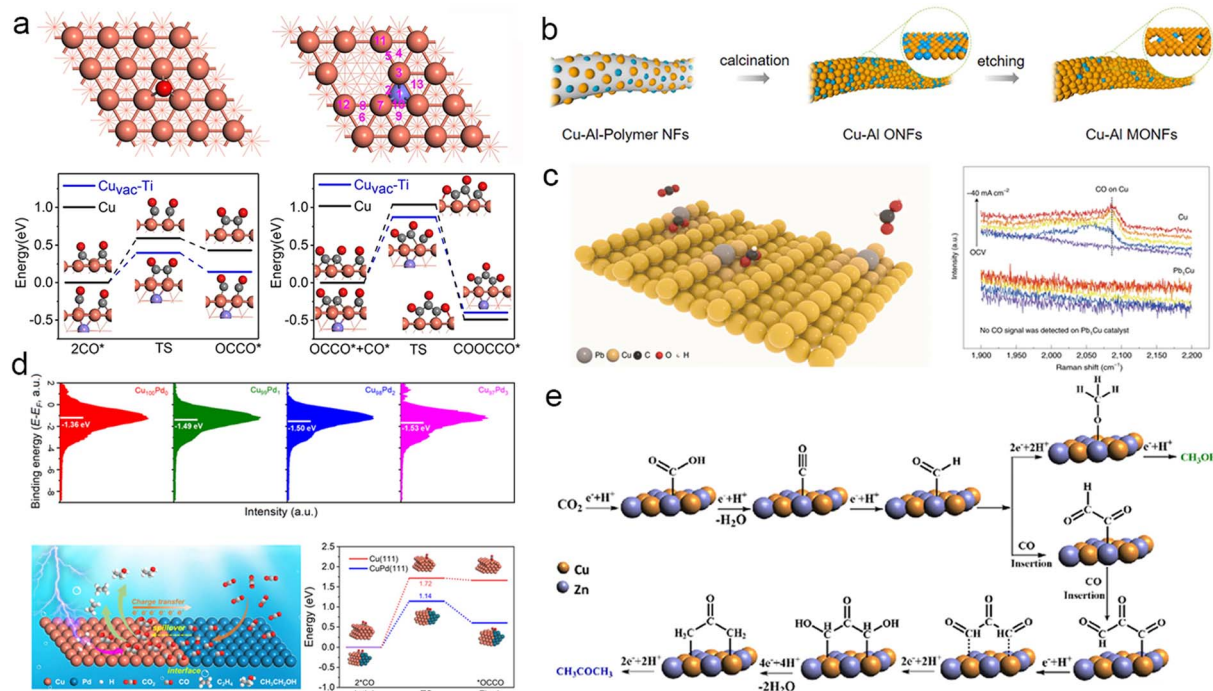


Fig. 4 (a) Adsorption energies of \*CO at Cu and Cu<sub>vac</sub>-Ti sites (above). Energy profiles for \*CO dimerization and trimerization at the Cu and Cu<sub>vac</sub>-Ti sites (below). The purple, orange, red, and gray spheres represent Ti, Cu, O, and C atoms, respectively. Reproduced from ref. 106. Copyright 2021 Wiley-VCH. (b) Schematic representation of the preparation of Cu–Al MONFs. Reproduced from ref. 107. Copyright 2022 American Chemical Society. (c) Schematic illustration of CO<sub>2</sub> conversion into HCOOH over a Pb<sub>1</sub>Cu SAA (left). *In situ* Raman spectra recorded at different current densities for Cu and Pb<sub>1</sub>Cu SAA catalysts, showing the absence of CO formation on the Pb<sub>1</sub>Cu catalyst (right). OCV, open-circuit voltage. Reproduced from ref. 108. Copyright 2022 Nature. (d) Surface valence band photoemission spectra of different CuPd catalysts (above). Schematic diagram of the mechanism of the Cu–Pd catalyst for facilitating the production of C<sub>2+</sub> products from ECR. Energy profile of \*CO coupling at the Cu domain and phase-separated Cu–Pd interface (below). Reproduced from ref. 113. Copyright 2023 Wiley-VCH. (e) Possible mechanisms for producing methanol and acetone on the Cu/Zn nanoalloys. Reproduced from ref. 71. Copyright 2022 Royal Society of Chemistry.



generate  $C_{2+}$  products. The Cu–Al MONFs achieved a remarkable  $C_{2+}$  faradaic efficiency of 76.4%, surpassing CuO nanofibers (with an FE of only  $\sim 10\%$ ) under the same conditions (Fig. 4b). Further investigation revealed that Al reconstructed the surface charge distribution of Cu, optimizing the energy barrier of  $^*CO$ – $^*COH$  coupling.<sup>107</sup> Doping Pb into Cu (Pb<sub>1</sub>Cu) alters the electronic environment of Cu active sites. These activated Cu sites modulate the adsorption free energy of HCOO\*, diverting the CO<sub>2</sub>RR toward the HCOO\* pathway rather than the COOH\* pathway and enhancing the selectivity of HCOOH with a high activity exceeding  $1 \text{ A cm}^{-2}$  (Fig. 4c).<sup>108</sup> Furthermore, the improved performance in ECR can be attributed to the direct adsorption of crucial intermediates at distinct atomic interfaces. For example, when Cu is doped with a second metal Sb (Sb<sub>1</sub>Cu), it stimulates a surface promotion effect for intermediates. Computational simulations indicate that Sb doping promotes CO<sub>2</sub> adsorption and activation while facilitating the desorption of  $^*CO$  during the reaction, significantly improving CO selectivity.<sup>59</sup> Introducing Pd to Cu creates a strong affinity for CO\* and effectively inhibits hydrogen precipitation, resulting in a single-pass carbon efficiency of 60% for CO<sub>2</sub> to  $C_{2+}$  at  $500 \text{ mA cm}^{-2}$  under acidic conditions.<sup>109</sup> Doping Cu with another metal atom can impact not only the charge distribution of the Cu surface but also other aspects like the catalyst's morphology. For instance, Cao *et al.* synthesized Cu nanowires decorated with a small quantity of Au nanoparticles (Cu–Au NWs) *via* a homonuclear method. The presence of Au nanoparticles increased the surface roughness of the catalyst, exposing more active sites, which enhances the adsorption of  $^*CO$  on the electron-deficient Cu surface. This in turn improved the selectivity towards  $C_{2+}$  products, resulting in an increase in faradaic efficiency from 39.7% (Cu NWs) to 65.3% (Cu–Au NWs).<sup>114</sup> Doping with other metals can also reduce the formation energy barrier of certain rare intermediates, enabling their production and even altering the reaction pathway towards desired products.<sup>61,110</sup> For example, CuAg thin films with nonequilibrium Cu/Ag alloying were fabricated *via* physical vapor deposition. This approach surpassed the limitations of thermodynamic miscibility and enhanced the interphase mixing of Ag into the Cu-rich catalyst. The improved miscibility optimized the binding energies of adsorbates and reaction intermediates on the catalyst surface, thereby increasing the selectivity for liquid carbonyl products such as CH<sub>3</sub>CHO and CH<sub>3</sub>COOH compared to bare Cu.<sup>111</sup> Expanding on the discovery of interphase miscibility, Jaramillo *et al.* investigated the impact of Ag doping on Cu (CuAg–NF) and its influence on the selectivity between CH<sub>3</sub>CHO and C<sub>2</sub>H<sub>5</sub>OH in electrochemical CO reduction. Utilizing density functional theory calculations, they attributed the higher selectivity towards CH<sub>3</sub>CHO rather than C<sub>2</sub>H<sub>5</sub>OH to the reduced formation energy barriers of relevant intermediates induced by Ag doping.<sup>112</sup> Cu, being the most promising metal for polycarbonate production, can experience CO “spillover” at the interface when doped with metals that predominantly produce C<sub>1</sub> products. This leads to further C–C coupling on Cu. For instance, the doping of Cu with Pd reduces the average d-band of the CuPd bimetallic catalyst below the Fermi level, facilitating CO spillover at the CuPd interface for

subsequent coupling (Fig. 4d).<sup>113</sup> Similarly, doping Cu with Au, another metal that primarily produces CO, can also result in CO spillover.<sup>114</sup> In addition, the presence of Zn in Cu<sub>1–x</sub>Zn<sub>x</sub> alloys has been observed to facilitate the spillover of CO. The introduction of Zn alters the catalyst's electronic structure by shifting the position of the d-band center, making  $^*CO$  desorption from the surface easier and promoting the formation of  $^*COCHO$  and even  $^*COCOCHO$ . This “CO insertion process” enhances the selectivity for CH<sub>3</sub>COCH<sub>3</sub> (Fig. 4e).<sup>71</sup> Doping Cu-based catalysts with a second metal is a straightforward strategy to selectively modify the electronic distribution by varying the type and amount of dopant. However, since metallic heteroatom doping is often costly, this approach is not economically feasible for large-scale industrial applications. There is a need to develop more cost-effective design strategies for non-precious metals.

### 3.2. Non-metallic heteroatom doping

Doping Cu-based catalysts with non-metallic elements induces interfacial strain and alters the electronic structure of the catalyst. This modification impacts the oxidation state of Cu, particularly when the electronegativity of the dopant exceeds that of Cu. As a result, the selectivity towards  $C_{2+}$  products is significantly enhanced. Compared to metallic heteroatom doping, non-metallic heteroatom doping reduces the overall costs of catalyst preparation due to the abundance of non-metallic elements. Consequently, non-metallic heteroatom doping has gained widespread application in recent years.<sup>115–118</sup>

By doping Cu-based catalysts with non-metallic heteroatoms, particularly halogen elements with higher

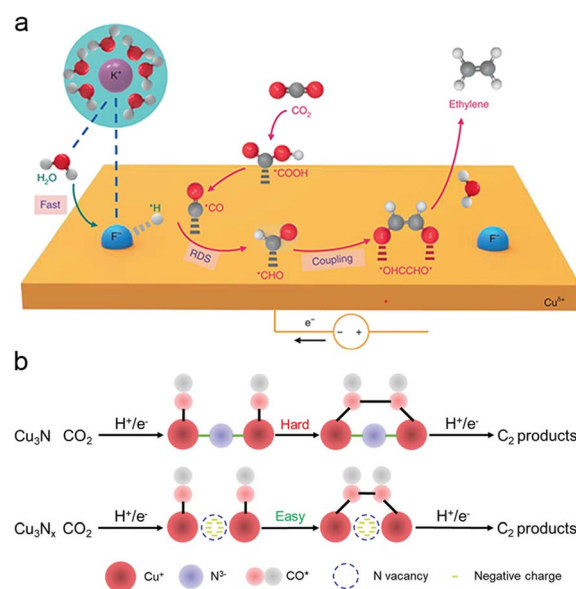


Fig. 5 (a) Schematic illustration of the possible reaction mechanism for C<sub>2</sub>H<sub>4</sub> generation over F–Cu catalysts. The purple, blue, red, gray, and white spheres represent K, F, O, C, and H atoms, respectively. Reproduced from ref. 93. Copyright 2020 Nature. (b) Schematic illustration of the simplified ECR mechanism towards C<sub>2</sub> products demonstrated by the Cu<sub>3</sub>N<sub>x</sub> model with nitrogen vacancies. Reproduced from ref. 122. Copyright 2021 Wiley-VCH.





electronegativity than Cu, the regulation of the d-band center of Cu can be achieved, thereby enhancing the absorption of key intermediates. For instance, fluorine-doped Cu-based catalysts exhibit enhanced capabilities in water dissociation, \*CO adsorption, and hydrogenation of \*CO to \*CHO (Fig. 5a). Notably, this fluorine-modified Cu catalyst achieved an impressive faradaic efficiency of approximately 80% for C<sub>2</sub> products (primarily C<sub>2</sub>H<sub>4</sub> and C<sub>2</sub>H<sub>5</sub>OH), with a remarkable current density of 1.6 A cm<sup>-2</sup>.<sup>93</sup> Similarly, iodide-derived copper (ID-Cu) benefits from high-density defects and surface roughness, which enhance \*CO adsorption by elevating the d-band center of Cu and facilitating C–C coupling on ID-Cu.<sup>119</sup> The doping of halogen elements induces the formation of Cu oxidation states while preserving the phase structure, resulting in strong adsorption of \*CO and other carbonate intermediates on Cu<sup>δ+</sup>. Cui *et al.* demonstrated that Cu<sup>+</sup> can be dynamically stabilized by I<sup>-</sup> in HCO<sub>3</sub><sup>-</sup> electrolytes through the formation of CuI, leading to the formation of atypical Cu(CO)<sup>+/0</sup> complexes with strong binding of *in situ* formed \*CO. This system achieved a remarkable 3.0-fold increase in faradaic efficiency towards C<sub>2</sub> compared to the system without I<sup>-</sup>.<sup>120</sup> Moreover, introducing halogen elements into Cu creates a synergistic effect that impacts the coordination microenvironment on active catalytic centers, thereby influencing the behavior of intermediates. Lan *et al.* constructed a stable crystalline single-chain catalyst model system consisting of four homomorphic one-dimensional chain-like compounds (Cu-PzH, Cu-PzCl, Cu-PzBr, and Cu-PzI). The difference in Pz ligands' electronegativity originates from the substituents of halogen atoms. This variation in the coordination microenvironment results in different D<sub>Cu-Cu</sub>

distances and β<sub>Cu-Cu</sub> dihedral angles between neighbouring Cu active sites, leading to linear regulation of catalyst selectivity for CH<sub>4</sub> and C<sub>2</sub>H<sub>4</sub>.<sup>121</sup>

Non-halogen heteroatom doping is another effective method to promote Cu oxidation states, leading to enhanced selectivity for C<sub>2+</sub> products. For example, Cu-based compounds with heteroatoms (N, P, S, O) underwent significant structural reconstruction to form heteroatom-derived Cu under CO<sub>2</sub>RR conditions. The N-engineered Cu (N-Cu) catalyst achieved the best CO<sub>2</sub>-to-C<sub>2+</sub> production rate at -1100 mA cm<sup>-2</sup> with a faradaic efficiency of 73.7%, outperforming most reported Cu-based catalysts.<sup>116</sup> Cubic copper nitrite (Cu<sub>3</sub>N<sub>x</sub>) with high-density nitrogen vacancies exhibits improved \*CO adsorption and subsequent \*CO-\*CO coupling, facilitating the enrichment of key C<sub>2</sub> intermediates (Fig. 5b). The Cu<sub>3</sub>N<sub>x</sub> catalyst, abundant in nitrogen vacancies, achieves an impressive faradaic efficiency of 81.7 ± 2.3% for C<sub>2</sub> products at 307 ± 9 mA cm<sup>-2</sup>.<sup>122</sup> In a similar vein, Oh *et al.* doped boron in copper oxide (B-CuO) to create multiple Cu<sup>δ+</sup> sites for electrochemical CO reduction. ATR-SEIRAS measurements directly revealed stronger \*CO adsorption on B-CuO compared to CuO, thereby promoting the C–C coupling of CO and resulting in a C<sub>2+</sub> faradaic efficiency of 62.1% at -0.62 V vs. RHE, a significant improvement over CuO with 48% faradaic efficiency.<sup>123</sup> The incorporation of non-metallic elements through heteroatom doping presents new opportunities for enhancing CO<sub>2</sub> to C<sub>2+</sub> conversion efficiency by modifying the local electronic environment on the catalyst surface. Non-metallic heteroatom doping is a widely adopted catalyst design strategy that allows easy regulation of the d-band center of Cu and the occurrence of Cu<sup>δ+</sup>, thereby modulating the

Table 1 Summary of the ECR performance of various Cu-based electrocatalysts

| Catalyst                              | Electrolyte  | Cell type | E (V vs. RHE) | j (mA cm <sup>-2</sup> ) | Main C <sub>2+</sub> product      | FE (%)     | Ref. |
|---------------------------------------|--|-----------|---------------|--------------------------|-----------------------------------|------------|------|
| <b>Metallic heteroatom doping</b>     |  |           |               |                          |                                   |            |      |
| Cu <sub>3</sub> Ag <sub>1</sub>       | 0.5 M KHCO <sub>3</sub>  | H-Cell    | -0.95         | 25                       | C <sub>2</sub> H <sub>5</sub> OH  | 63         | 61   |
| Cu-Sn <sub>x</sub>                    | 0.1 M KHCO <sub>3</sub>  | H-Cell    | -1.4          | 15.05                    | C <sub>2</sub> H <sub>5</sub> OH  | 25.93      | 69   |
| Cu <sub>1-x</sub> Zn <sub>x</sub>     | 0.1 M NaHCO <sub>3</sub>   | Flow cell | -0.4          |                          | CH <sub>3</sub> COCH <sub>3</sub> | 19         | 71   |
| a-CuTi@Cu                             | 0.1 M KHCO <sub>3</sub>  | H-Cell    | -0.8          |                          | C <sub>2-4</sub>                  | 48.82      | 106  |
| Cu-Al MONFs                           | 1 M KOH  | Flow cell | -1.7          | 458                      | C <sub>2+</sub>                   | 76.4       | 107  |
| Pb <sub>1</sub> Cu                    | 0.5 M KHCO <sub>3</sub>  | H-Cell    | -0.80         | 800                      | HCOOH                             | 96         | 124  |
| Sb <sub>1</sub> Cu-5                  | 0.5 M KHCO <sub>3</sub>  | Flow cell | -1.16         | 452                      | CO                                | 91         | 59   |
| Pd-Cu catalyst                        | 0.5 M K <sub>2</sub> SO <sub>4</sub> (pH adjusted to 2.0 with H <sub>2</sub> SO <sub>4</sub> ) | Flow cell |               | 500                      | C <sub>2+</sub>                   | 89 ± 4     | 109  |
| <b>Non-metallic heteroatom doping</b> |  |           |               |                          |                                   |            |      |
| Cu-Au NWs                             | 0.1 M KHCO <sub>3</sub> & 0.1 M KCl  | H-Cell    | -1.25         | 12.1                     | C <sub>2+</sub>                   | 65.3       | 114  |
| BaO/Cu                                | 1 M KOH  | Flow cell | -0.75         | 244                      | C <sub>2+</sub> alcohol           | 61         | 110  |
| CuAg thin film                        | 0.1 M KHCO <sub>3</sub>  | H-Cell    |               | 16                       | Carbonyl products                 | 8.1        | 111  |
| CuAg                                  | 0.1 M KOH  | Flow cell | -0.536        | 20                       | CH <sub>3</sub> CHO               | 50         | 112  |
| CuOHfCl NSs                           | 0.1 M KHCO <sub>3</sub>  | H-Cell    | -1            | 53                       | C <sub>2+</sub>                   | 53.8       | 125  |
| Sputtered Cu                          | 0.1 M KHCO <sub>3</sub> & 0.1 M KI   | H-Cell    | -0.95         | 13                       | C <sub>2+</sub>                   | 55         | 120  |
| ID-Cu                                 | 0.1 M KHCO <sub>3</sub>  | Flow cell | -1.1          | 290                      | C <sub>2+</sub>                   | 71.16      | 119  |
| Cu-PzX                                | 1 M KOH  | Flow cell | -0.9          | 346.46                   | C <sub>2</sub> H <sub>4</sub>     | 39.4       | 121  |
|                                       |  |           | -1            | 287.52                   | CH <sub>4</sub>                   | 25.35      |      |
| N-Cu                                  | 1 M KOH  | Flow cell | -1.15         | 1100                     | C <sub>2+</sub>                   | 73.7       | 116  |
| Cu <sub>3</sub> N <sub>x</sub>        | 1 M KOH  | Flow cell | -1.15         | 307 ± 9                  | C <sub>2</sub>                    | 81.7 ± 2.3 | 122  |
| B-CuO                                 | 1 M KOH & 1 M KHCO <sub>3</sub>  | Flow cell | -0.62         | 135                      | C <sub>2+</sub>                   | 62.1       | 123  |



adsorption strength of intermediates, particularly enhancing CO adsorption. Non-metallic heteroatom doping provides valuable insights into the low-cost preparation of catalysts that can achieve electrocatalytic activity comparable to that of catalysts prepared *via* metallic heteroatom doping.

## 4. Morphological structure engineering

Among the current cutting-edge designs for Cu-based catalysts aimed at regulating intermediates, the second major category is morphological structure engineering, which is equally prevalent as heteroatom doping. The manipulation of catalyst morphologies can significantly influence the exposure configuration and abundance of active sites on the catalyst surface, thereby exerting a critical and complex impact on the behaviour of key intermediates and even the distribution of products.<sup>126</sup> Particularly, the geometric confinement effect plays a significant role in enhancing the localized retention of key intermediates, effectively promoting the formation of multi-carbon products and deepening the extent of product reduction. Considering these advantages, morphological structure engineering holds greater promise for practical applications than heteroatom doping. The reported works in this field can be categorized as follows: grain boundary effect, geometric confinement through pores and hierarchical structures, facet engineering, defect engineering, and the influence of chemical state (Table 2).

### 4.1. Grain boundary effect

In general, the activity of catalysts in CO<sub>2</sub> and CO reduction is proportional to the abundance of grain boundaries (Fig. 6a).<sup>127–130</sup> Therefore, it is widely accepted that grain boundaries play a crucial role in modulating the absorption energy barriers of intermediates, thereby promoting the formation of multi-carbon products.<sup>57,131–134</sup> Grain boundaries typically form between different crystalline phases of copper with the same valence state.<sup>135</sup> Gong *et al.* fabricated copper catalysts rich in grain boundaries (GB-Cu) *via* additive-controlled electrodeposition. *In situ* attenuated total reflectance surface-enhanced infrared absorption spectroscopy (ATR-SEIRAS) demonstrated that the presence of enriched grain boundaries enhanced the adsorption of the key intermediate CO on copper surfaces, enabling GB-Cu to achieve a C<sub>2</sub> faradaic efficiency of up to 70% over a wide potential range (Fig. 6b and c).<sup>136</sup> Similarly, Zheng *et al.* created a CuO electrocatalyst with high-density grain boundaries and micron-strains by rapidly cooling in liquid nitrogen (Fig. 6d). With an increased cooling rate, the CuO catalyst exhibited remarkable faradaic efficiency for C<sub>2</sub> products, mainly C<sub>2</sub>H<sub>5</sub>OH, with partial current densities reaching up to 300 mA cm<sup>-2</sup>.<sup>137</sup> Grain boundaries can also exist between different facets of Cu with the same valence state and between Cu with different valence states.<sup>138</sup> Through the simple reduction of Cu(OH)<sub>2</sub> and carbonization, Han *et al.* prepared a series of Cu-based composites with a range of gradient grain boundary densities and Cu<sup>+</sup>/Cu<sup>0</sup> ratios. The enhanced adsorption of CO\* on Cu<sup>+</sup> and

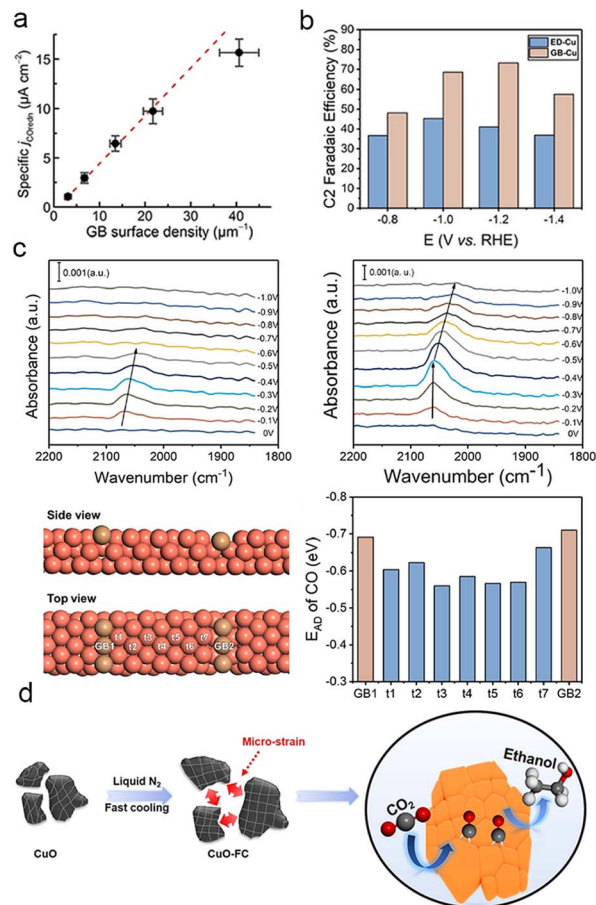


Fig. 6 (a) Modelled linear relationship between GB surface density and CO-specific activity, the potential is at  $-0.4$  V vs. RHE. Reproduced from ref. 131. Copyright 2016 American Chemical Society. (b) Different faradaic efficiencies for C<sub>2</sub> products on ED-Cu and GB-Cu. (c) *In situ* ATR-SEIRAS spectra of ED-Cu and GB-Cu (above). Different binding sites on the schemed atomic structure and corresponding \*CO binding energies of GB-Cu (below). Reproduced from ref. 136. Copyright 2020 American Chemical Society. (d) Schematic illustration of the construction of CuO electrocatalysts with high-density grain boundaries by a fast cooling strategy. Reproduced from ref. 137. Copyright 2020 Elsevier.

the high density of grain boundaries resulted in a faradaic efficiency of 64.5% for C<sub>2</sub> products at 26.2 mA cm<sup>-2</sup>.<sup>139</sup>

An effective approach to enhance the production of C<sub>2</sub> products is the construction of electrocatalysts with abundant grain boundaries, which directly facilitate the adsorption of CO\* on the surface.<sup>140–142</sup> However, control over the construction and density of grain boundaries is challenging due to the uncertainty of *in situ* catalyst growth and the difficulty of characterization.<sup>143</sup> This presents a significant challenge in developing catalysts rich in grain boundaries.

### 4.2. Geometric confinement of pore and hierarchical structure

The design of catalysts with abundant pores and hierarchical structures offers two key advantages: it increases the surface area-to-volume ratio, exposes more active sites for the reaction,



and enhances the mass transport of reactants.<sup>144–146</sup> The porosity of catalysts can be classified into three types: macropores (>50 nm), mesopores (2–50 nm), and micropores (<2 nm). Macropores expand the specific surface area of the catalyst and facilitate the diffusion of electrolyte and reactant molecules. Mesopores and micropores both configure the intermediates and prevent their leakage,<sup>147–150</sup> while creating an OH<sup>−</sup>-rich microenvironment that promotes C–C coupling.<sup>151–153</sup> In summary, constructing porous catalysts is a straightforward and effective approach to control the concentration and residence time of intermediates.<sup>154–158</sup>

One effective approach to enhance the performance of ECR is to design catalysts with a high degree of porosity, which increases the concentration of CO and facilitates their coupling. Ma *et al.* successfully synthesized a series of uniform hollow oxide-derived Cu (OD-Cu-H) catalysts with varying degrees of porosity by a simple method. They observed a positive correlation between porosity density and C<sub>2</sub> selectivity, while C<sub>1</sub> products and H<sub>2</sub> formation showed a negative correlation. This phenomenon was attributed to the localization of CO\* and the promotion of C–C coupling on the porous surface (Fig. 7a).<sup>159</sup> Similarly, Deng *et al.* utilized mechanically polished Cu foils to expose highly reactive Cu sites that effectively confined \*CO and other intermediates for the subsequent generation of C<sub>2+</sub> products.<sup>160</sup> In addition, Geng *et al.* investigated the effect of

pore size on the regulation of \*CO intermediates using core-shell Ag@Cu catalysts. They discovered that moderately sized mesopores (4.9 nm) on the Cu shell provided optimal confinement for \*CO (Fig. 7b), leading to an improved catalytic performance for C<sub>2+</sub> products, with a yield of approximately 73.7% at 300 mA cm<sup>−2</sup>.<sup>147</sup> Zeng *et al.* documented a correlation between CO<sub>2</sub>-to-C<sub>2+</sub> conversion and the nanoconfinement effect of Cu hollow multi-shell structures. Specifically, an increase in the number of shells is positively associated with the selectivity and activity of the C<sub>2+</sub> species. Simulations using the finite element method demonstrated that an increase in the number of shells enhances the C–C coupling process by reducing diffusion kinetics, enabling a higher concentration of CO adsorbates to accumulate within the nanovoids.<sup>153</sup>

In addition to regulating key intermediates associated with the reaction, the porosity of catalysts also plays a crucial role in stabilizing the active species during ECR.<sup>41,90,148</sup> For instance, Yu *et al.* successfully constructed Cu<sub>2</sub>O catalysts with nanocavities, effectively preventing the overflow of carbon intermediates and maintaining high coverage of easily reduced Cu<sup>+</sup> species. The high concentration of Cu<sup>+</sup> species greatly enhanced the selectivity for C<sub>2+</sub> products, resulting in a remarkable C<sub>2+</sub>/C<sub>1</sub> ratio of approximately 7.2 at high reaction rates (Fig. 7c). Raman spectroscopy and X-ray absorption studies confirmed the stability of Cu<sup>+</sup> species during the catalytic process.<sup>148</sup> The suitable and

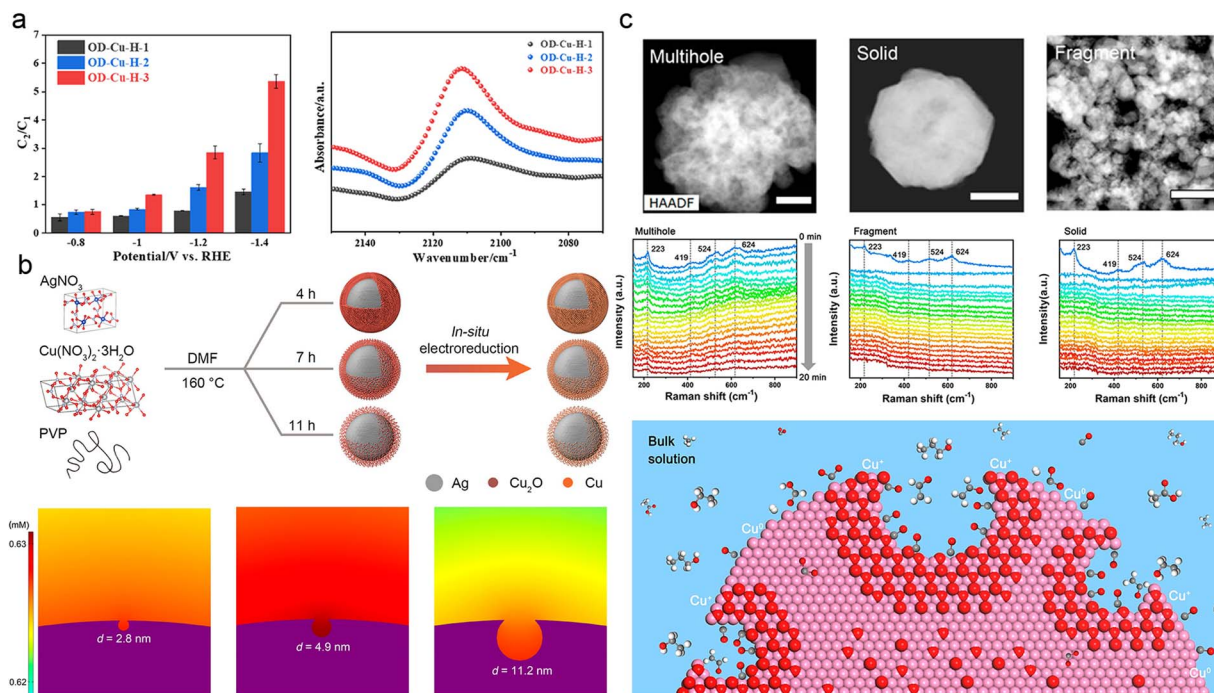


Fig. 7 (a)  $FE_{C_2}/FE_{C_1}$  for OD-Cu-H-1, OD-Cu-H-2, and OD-Cu-H-3 at varied potentials (left). Comparison of *in situ* ATR-SEIRAS spectral intensities of OD-Cu catalysts in the range 2140–2080 cm<sup>−1</sup> at −0.1 V vs. RHE (right). The hollowness of OD-Cu-H-1, OD-Cu-H-2, and OD-Cu-H-3 is progressively increasing. Reproduced from ref. 157. Copyright 2022 American Chemical Society. (b) Schematic diagram of the synthesis of Ag@Cu catalysts with different pore sizes in porous copper shells (above). Simulated concentration distribution of local CO on porous Cu surfaces with different pore diameters: 2.8 nm, 4.9 nm, and 11.2 nm (below). Reproduced from ref. 145. Copyright 2022 American Chemical Society. (c) *Operando* Raman spectra of multihollow, fragmental, and solid Cu<sub>2</sub>O at −0.61 V vs. RHE as a function of reaction time (above). Schematic representation of a nanocavity limiting the spillage of carbon intermediates, which also protected the oxidized state of copper from reduction during ECR (below). The white, grey, red, and violet spheres represent H, C, O, and Cu atoms, respectively. Reproduced from ref. 146. Copyright 2020 American Chemical Society.



abundant porosity of the catalyst, along with the presence of stable active species, provides geometric confinement for the intermediates. Additionally, the hierarchical structure of the catalyst influences the residence and reaction pathways of intermediates, as well as the kinetics of the protonation process.<sup>81,146,161</sup> Zhang *et al.* developed multi-shelled CuO microboxes and investigated the effect of the hierarchical structure on active sites' exposure and the adsorption of carbonate intermediates.<sup>162</sup> They discovered that small and uniform multi-shelled CuO microboxes exhibited significantly improved performance in converting CO<sub>2</sub> into C<sub>2</sub>H<sub>4</sub>, which was attributed to the enrichment of \*CO.

Constructing moderate pores or hierarchical structures is a promising strategy for regulating the behaviour of key intermediates and promoting the formation of C<sub>2+</sub> products in ECR. However, the type of intermediate, rather than the retention time, is the primary factor and is influenced by geometric and hierarchical confinement. Therefore, to achieve high selectivity for desirable products, more complex morphological structures are required, which can precisely control the type of reaction intermediate.

#### 4.3. Facet

The facet structure of Cu is an important factor that influences the behaviour of intermediates on its surface. Copper (Cu) is a metallic material that exhibits multiple crystalline facets, typically consisting of low-index facets unless specifically modified. Different crystal facets of Cu exhibit distinct periodic arrangements of atoms and surface electronic structures, leading to varying adsorption strengths for reaction intermediates.<sup>43,163</sup> Unlike the commonly observed low-index facets, relatively high-index crystal facets such as Cu(511) and Cu(611) possess abundant step-like sites and kinks on their surfaces. These step-like sites and kinks on these facets exhibit low coordination numbers for Cu reaction sites, resulting in higher catalytic activity than Cu reaction sites on low-index facets.<sup>164</sup>

Different facets of Cu exhibit distinct catalytic orientations in ECR. Extensive research indicates that Cu(100) and Cu(110) facets are preferred for generating C<sub>2+</sub> products due to their enhanced adsorption of \*CO, leading to the formation of \*OCCO and \*CH<sub>2</sub>CHO.<sup>165</sup> In contrast, the Cu(111) facet promotes the formation of C<sub>1</sub> products, such as CH<sub>4</sub>, by facilitating the generation of \*COOH and \*CO.<sup>43,165–167</sup> Sun *et al.* investigated the influence of the Cu(100) facet on CO<sub>2</sub> electroreduction by employing hierarchical micro/nanostructured Cu(100)-rich copper hollow fibers as a gas penetration electrode. Theoretical calculations (Fig. 8a) confirmed a significant enhancement in the adsorption of \*CO on the Cu(100) facet, enabling efficient C–C coupling and yielding a remarkable selectivity of 62.8% towards C<sub>2+</sub> products at an ultra-high current of 2.3 A cm<sup>-2</sup>, surpassing that of existing Cu-based catalysts.<sup>168</sup> Several recent studies have reported the enhanced adsorption of \*CO on Cu(100) and Cu(110) crystalline surfaces.<sup>169–171</sup>

The synergistic effect of different crystalline sites is worth considering to modulate the behaviour of reaction intermediates. Through investigating the edge-to-surface ratio of Cu NC

catalysts, Wang *et al.* demonstrated the significance of the Cu(100) facet in combination with step-like sites along the edge to improve the selectivity of acetic acid production (Fig. 8b).<sup>172</sup> Similarly, Sargent *et al.* investigated the synergistic effect of C<sub>1</sub> and C<sub>2</sub> sites on highly fragmented Cu, which facilitated the coupling of C<sub>1</sub> and C<sub>2</sub> intermediates to promote the formation of CH<sub>3</sub>CH<sub>2</sub>CH<sub>2</sub>OH (Fig. 8c and d). They achieved a selectivity of 20% at a high reaction rate, corresponding to a partial current density of 8.5 mA cm<sup>-2</sup>.<sup>70</sup> In addition to facet orientation, the surface orderliness of Cu also impacts the behaviour of reaction intermediates during ECR. Roldan Cuenya *et al.* observed that highly clean, atomically ordered Cu(111) and Cu(100) single crystal facets predominantly yield H<sub>2</sub> instead of the expected hydrocarbon products. Hydrocarbon products from CO<sub>2</sub> conversion are primarily achieved when there are adequate defects and high-index crystal surfaces.<sup>173</sup> Therefore, constructing non-planar sites and high-energy crystal surfaces is crucial to enhance the catalysts' ability to regulate intermediates. For instance, Huang *et al.* activated Cu nanowires and introduced a highly stepped surface morphology. Experimental findings indicate a positive correlation between the proportion of stepped-surface structure A-(*hkl*) and the faradaic efficiency of C<sub>2</sub>H<sub>4</sub>, which is attributed to the increased adsorption of 2CO\* on the stepped surface [3(100) × (111)] (Fig. 8e).<sup>174</sup> Likewise, Guo *et al.* explored the nature of CO–CO structures adsorbed on high-index Cu surfaces and reaffirmed their contribution to C<sub>2+</sub> products.<sup>175</sup>

Selecting the appropriate crystalline facets is vital in regulating the behaviour of key intermediates, thereby influencing the reaction pathway and product distribution. Additionally, the synergistic effects of specific crystallographic facets should be taken into consideration.<sup>175</sup> Nevertheless, accurate characterization of the catalyst surface morphology is necessary as the catalytic site may not align with our expectations.

#### 4.4. Defect

Constructing defects on Cu catalysts provides a means to modify the coordination environment and electronic structure of Cu without introducing additional elements. Defects, also referred to as ion vacancies, can enhance CO<sub>2</sub> activation and \*C<sub>1</sub> adsorption, thereby promoting the formation of desirable C<sub>2+</sub> products.<sup>176,177</sup> For instance, Zheng *et al.* synthesized a Cu catalyst with abundant defect sites under CO-rich conditions (Cu<sub>DS</sub>), and they demonstrated that the substantial \*CO coverage on the Cu<sub>DS</sub> surface activated the CO<sub>2</sub>–C<sub>2</sub>H<sub>5</sub>OH reaction pathway with its strong adsorption, as depicted in Fig. 9a and b.<sup>178</sup> In certain cases, defects do not act alone as promoters of the CO<sub>2</sub>RR; rather, they synergistically interact with specific crystalline facets like Cu(100), Cu(110), or grain boundaries to precisely modulate the surface intermediates. Cuenya *et al.* achieved oxidation state and morphology tuning of the copper catalysts *via* pulsed CO<sub>2</sub> electrolysis, revealing that the optimal arrangement of Cu(100) domains, defect sites, and surface Cu<sub>2</sub>O promoted the CO<sub>2</sub>RR pathway towards C<sub>2+</sub> products. Specifically, they observed that the enhanced C<sub>2</sub>H<sub>5</sub>OH selectivity correlated with the coexistence of Cu(I) and Cu<sup>0</sup> species,





**Fig. 8** (a) Different  $C_1$  (short dashed) and  $C_{2+}$  (solid) product distributions of the hollow copper fiber (Cu HF, red) and activated Cu HF (green) as a function of current density (left). Activation energy barrier of  $OCCO^*$  and  $OCCOH^*$  from  $CO^*$  (right). Reproduced from ref. 167. Copyright 2022 Royal Society of Chemistry. (b) Reaction energy barriers for the formation of  $*HOCCOH$  from  $*OCCOH$  in synergy with Cu(611) and Cu(100) at  $0 V_{RHE}$  and  $-1 V_{RHE}$ . The insets show the geometry of the system. Orange: Cu, red: O, grey: C, white: H. Reproduced from ref. 171. Copyright 2020 Proceedings of the National Academy of Sciences. (c) HR-TEM images of the crystal facets of HF-Cu, MF-Cu and LF-Cu catalysts; the blue dashed line circles Cu(100), the red dashed line circles Cu(111) facets and the yellow dashed line highlights the interface between the (100) and (111) facets. HR-TEM scale bar, 10 nm. (d) Geometrical schematics representing the Cu(111) and Cu(100) interfaces between Cu(111) and Cu(100) respectively (above). The reaction energy barriers for dimerization and trimerization reactions at the Cu(111) and Cu(100), and the interfaces between Cu(111) and Cu(100). Schematic diagram of a catalyst with highly mixed nanofragments of Cu(200) and Cu(111) facets on which  $C_1$  and  $C_2$  sites are very close together to facilitate  $C_1$ - $C_2$  coupling and coupling into  $C_3$  products (below). Reproduced from ref. 70. Copyright 2019 Nature. (e) Linear correlation between the fraction of surface facet and activation time on A-CuNW surfaces. A-(hkl) ratios correlated with product FEs at approximately  $-0.99$  to  $-1.00 V$  vs. RHE (above). Adsorption energies ( $\Delta G_{ads}$ ) of  $CO^*$  and  $2CO^*$  on Cu(100) and Cu(511). The reaction coordinate of  $C_1$  and  $C_2$  pathways on Cu(100) and Cu(511).  $CO+^*$  represents CO and the active site on the surface before the adsorption of CO;  $CO^*$  represents the active site where CO was adsorbed. Reproduced from ref. 173. Copyright 2020 Nature.

while the extent of the Cu(100) gradient predominantly influenced  $C_2H_4$  production, as depicted in Fig. 9c.<sup>179</sup>

Achieving precise control over the construction of defects on Cu has posed a longstanding challenge for scientists due to the inherent difficulty in precise defect manipulation. In recent years, several studies have documented the introduction and subsequent removal of heteroatoms in Cu-based catalysts as a method to create defects.<sup>98,180</sup> For instance, Zheng *et al.* devised a straightforward lithium electrochemical modulation strategy, which not only generates a high density of double sulphur vacancies but also reduces the Cu-Cu distance, as illustrated in Fig. 9d. Their investigation revealed that the bisulfide vacancies formed within the hexagonal CuS (100) plane served as active electrocatalytic centers for  $CO_2$  electroreduction, promoting the stability of  $CO^*$  and  $OCCO^*$  dimers and facilitating the  $*CO-OCCO^*$  coupling, leading to the formation of the crucial  $*C_3$  intermediate in  $CH_3CH_2CH_2OH$

production. As a result, the catalytic performance of  $CH_3CH_2CH_2OH$ , quantified by its faradaic efficiency, can reach as high as 15.4% in the H-cell along with a partial current density of  $9.9 mA cm^{-2}$  in the flow cell.<sup>98</sup>

Defects can also be created by removing other highly electronegative elements, such as halogens. Palmore *et al.* documented a practical and scalable anodic halogenation method for fabricating Cu-based catalysts with a significant defect density. They also explored the correlation between defect density, surface roughness, and the anodic halogenation conditions of the catalysts. The investigation revealed that the Cu(i)X-derived catalysts (where X = Cl, Br, or I) exhibited exceptional performance in ECR, which can be attributed to the enhanced adsorption of carbonate intermediates on the catalyst surface. The experimental results and characterization data strongly indicate that the abundant defects greatly promote the production of polycarbonate products, while reducing





**Fig. 9** (a) Schematic illustration of the synthesis of a Cu<sub>DS</sub> catalyst under a CO-rich environment, which favours high coverage of the \*CO intermediate and promotes alcohol production, and the subsequent CO<sub>2</sub>RR process. (b) The product distribution of the Cu<sub>DS</sub> catalyst in an H-type cell and flow cell, respectively. Reproduced from ref. 177. Copyright 2021 Elsevier. (c)  $Q_{\text{defects}}/Q_{100}$  and product selectivity as a function of pulsed versus potentiostatic conditions on a Cu(100) electrode; copper stepped surfaces were used for comparison. Voltametric properties of the copper surfaces recorded in 0.1 M NaOH ( $50 \text{ mV s}^{-1}$ ) are shown in the top row. Unless otherwise stated, measurements were performed at a constant potential of  $-1.0 \text{ V}$ , and the pulse conditions are labelled as:  $E_a = 0.6 \text{ V}$ ,  $E_c = -1.0 \text{ V}$ ,  $t_a = 1 \text{ s}$ ,  $t_c$  as indicated, 1 h reaction. Measurements performed under pulsed conditions and continuous constant potential are indicated by shaded areas. Reproduced from ref. 178. Copyright 2020 Nature. (d) Schematic illustration of the formation mechanism of *n*-propanol on the adjacent CuS<sub>x</sub>-DSV, showing the dimerization of CO-CO and coupling of CO-OCCO. Reproduced from ref. 98. Copyright 2021 Nature. (e) Diagram of catalyst roughness and FE of H<sub>2</sub> as a function of halogenation time. (f) Schematic diagram of low coordination copper atoms and surface roughness with the corresponding ECR results. The coordination number for face-centred cubic copper is 12. Reproduced from ref. 180. Copyright 2020 Nature.

roughness mitigates the competition from hydrogen precipitation (Fig. 9e and f).<sup>181</sup> Consequently, this offers a novel avenue for the meticulous design of catalyst defect structures.

Engineering defects enables precise control of reaction intermediates, particularly \*C<sub>1</sub>, and can significantly impact the reaction pathway. Defects can synergistically interact with specific sites like facets and grain boundaries in certain cases. Moreover, there is growing documentation on the precise incorporation of defects into Cu-based catalysts, establishing defect engineering as a strategy capable of precisely modulating the concentration and reaction behaviour of intermediates.

#### 4.5. Chemical state effect

The oxidation state of an atom represents the electron gain or loss in a chemical bond, providing insights into the nature and strength of its covalent or ionic interactions.<sup>182</sup> Oxide-derived copper (OD-Cu) catalysts primarily consist of Cu<sup>+</sup> and Cu<sup>2+</sup> species and are synthesized by incompletely reducing copper oxide precursors.<sup>183–185</sup> Following Kanan *et al.*'s groundbreaking work on the exceptional catalytic performance of annealed Cu for ECR (Fig. 10a),<sup>186</sup> numerous studies have investigated the mechanism and performance of OD-Cu catalysts for electrocatalytic CO<sub>2</sub> reduction.<sup>137,179,187</sup> Jung *et al.*

developed a novel porous Cu/Cu<sub>2</sub>O aerogel with remarkable C<sub>2</sub>H<sub>5</sub>OH productivity in ECR (Fig. 10b–d). They attributed this to the presence of abundant Cu<sup>0</sup>-Cu<sup>+</sup> interfaces and the elevated local pH within the confined porous aerogel network structure, resulting in a high faradaic efficiency (FE<sub>EtOH</sub>) of 41.2% and a partial current density ( $J_{\text{EtOH}}$ ) of  $32.55 \text{ mA cm}^{-2}$ .<sup>188</sup> The valence effect often synergizes with other factors to modulate the behaviour of intermediates and enhance the performance of Cu-based catalysts in ECR. An exemplary case of this synergy is the unique and stable OD-Cu (Cu<sub>4</sub>O) catalyst, characterized by a hierarchical pore and nanograin-boundary structure. Systematic characterization analysis and theoretical calculations demonstrated that the atypical OD-Cu enables highly sensitive modulation towards \*CO adsorption and boosts further C-C dimerization, eventually achieving an outstanding faradaic efficiency of 45% towards C<sub>2</sub>H<sub>4</sub> at a partial current density of  $44.7 \text{ mA cm}^{-2}$  in neutral media (Fig. 10e).<sup>189</sup>

Non-zero-valent Cu in its single-atom form demonstrates exceptional control over carbon intermediates, distinct from bulk-scale OD-Cu. Li *et al.* introduced a novel atom-pair catalyst strategy, demonstrating the stabilization of Cu atom-pair sites (Cu<sub>10</sub>-Cu<sub>1</sub><sup>x+</sup>) on Te surface defects of Pd<sub>10</sub>Te<sub>3</sub> alloy nanowires. The authors investigated the mechanism of these catalysts, referred to as the “bi-atomic activating bimolecular”



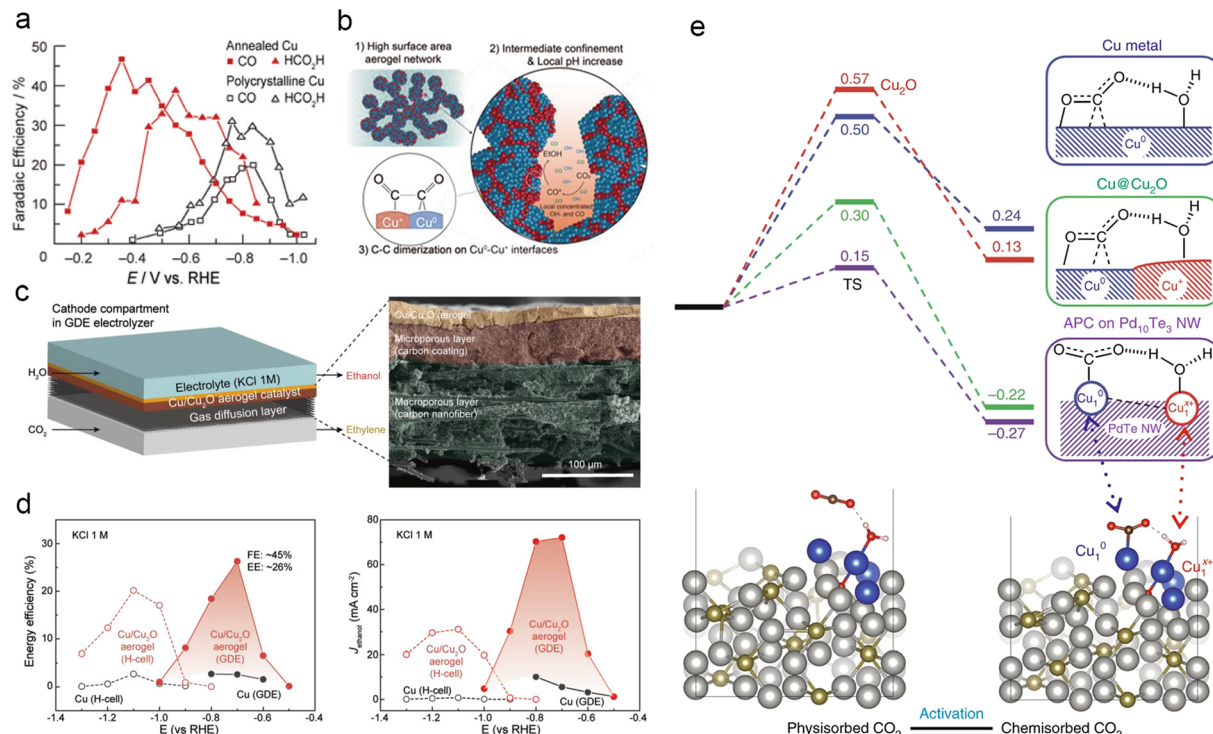


**Fig. 10** (a) Product distribution for CO and HCOOH of polycrystalline Cu and Cu annealed at 500 °C for 12 h (resulting in Cu<sub>2</sub>O layers). Reproduced from ref. 185. Copyright 2012 American Chemical Society. (b) Schematic representation of the mechanism promoting ethanol production on Cu/Cu<sub>2</sub>O aerogels and proposed origin. (c) Schematic diagram of the flow cell reactor and cross-sectional SEM images of the Cu/Cu<sub>2</sub>O aerogel on the GDE. (d) Comparison of EE<sub>EtOH</sub> and J<sub>EtOH</sub> for Cu/Cu<sub>2</sub>O aerogels and Cu films in H-cell and flow-cell reactors, respectively. Reproduced from ref. 187. Copyright 2021 Wiley-VCH. (e) Free energy curves of CO<sub>2</sub> activation on Cu, Cu@Cu<sub>2</sub>O and APCs of Cu<sub>10</sub>–Cu<sub>1</sub><sup>x+</sup> on Pd<sub>10</sub>Te<sub>3</sub> nanowires, respectively (at –0.78 V vs. RHE) (above). Conformations of physisorbed and chemisorbed CO<sub>2</sub> on Cu-APC (below). Reproduced from ref. 188. Copyright 2019 Nature.

mechanism. Experimental results and density functional theory (DFT) simulations reveal that Cu<sub>1</sub><sup>x+</sup> improves H<sub>2</sub>O adsorption and stabilizes chemisorbed CO<sub>2</sub> molecules on adjacent Cu<sub>10</sub>, facilitating protonation and subsequent reduction of the absorbed CO<sub>2</sub>. The kinetics and thermodynamic favourability of Cu atom-pair sites enable the catalyst to attain a faradaic efficiency of over 92% for CO while negligibly impacting the hydrogen evolution reaction.<sup>190</sup>

Despite the extensive research highlighting the exceptional performance of OD-Cu surfaces,<sup>170,187,191</sup> Cu<sup>0</sup>–Cu<sup>+</sup> interfaces<sup>132</sup> and single-atom pairs of Cu in CO<sub>2</sub> electrolysis, certain questions remain unanswered: can oxidized Cu be sustained under highly negative voltages?<sup>192</sup> Moreover, is oxidized Cu the true catalytic site for CO<sub>2</sub> reduction?<sup>193,194</sup> Addressing these questions is crucial since they have implications for designing and optimizing Cu-based catalysts in ECR. While a consensus on these questions has yet to be reached, further research and discussions are anticipated to provide insights.<sup>195,196</sup>

## 5. Local catalytic environment engineering

In addition to catalyst structure construction, another approach to catalyst design for CO<sub>2</sub> electrolysis is the modulation of the local catalytic environment, which pertains to the specific

conditions of active sites. This strategy encompasses several principles, including the substrate effect, co-catalyst effect (tandem catalyst effect), surface additive effect, reactant coverage effect, and local electrolyte microenvironment effect (Table 3). These factors impact the adsorption, activation, and reaction of multiple intermediates on the catalyst surface, therefore influencing the selectivity and efficiency of CO<sub>2</sub> electrolysis.

### 5.1. Substrate effect

The substrate on which the metal nanoparticles are loaded is one of the factors that can modulate the local catalytic environment of active sites in ECR.<sup>198</sup> The substrate can influence the catalytic performance of metal nanoparticles in multiple ways. First, the substrate can facilitate efficient electron transfer, thereby modulating the electronic structure of the catalyst surface.<sup>183,199</sup> Second, highly porous substrates can restrict the domain of metal nanoparticles, preventing their reduction or agglomeration.<sup>200,201</sup> These characteristics significantly impact the modulation of intermediates' behaviour, thus influencing the selectivity and efficiency of CO<sub>2</sub> electrolysis.<sup>202,203</sup>

Carbon materials are commonly employed as substrates of Cu-based catalysts due to their high electrical conductivity, easily controlled morphological structure and long-lasting stability. For instance, Lv *et al.* synthesized silk fibroin (SF)-

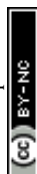


Table 2 Summary of the ECR performance of various Cu-based electrocatalysts

| Catalyst  | Electrolyte                          | Cell type | $E$ (V vs. RHE) | $j$ (mA cm <sup>-2</sup> ) | Main C <sub>2+</sub> product                                     | FE (%)       | Ref. |
|---|--------------------------------------|-----------|-----------------|----------------------------|--|--------------|------|
| <b>Grain boundary</b>   |                                      |           |                 |                            |  |              |      |
| Cu/CNT  | 0.1 M KOH                            | H-Cell    | -0.3            |                            | C <sub>2</sub> H <sub>5</sub> OH, CH <sub>3</sub> COOH           | 72           | 131  |
| CuO nanosheets  | 3 M KOH                              | H-Cell    | -0.52           | 173                        | C <sub>2</sub> H <sub>4</sub>                                    | 62.5         | 132  |
| GB-Cu   | 1 M KOH                              | Flow cell | -1.0–-1.3       | 52                         | C <sub>2</sub> H <sub>4</sub> , C <sub>2</sub> H <sub>5</sub> OH | 73.2         | 136  |
| CuO-FC  | 1 M KOH                              | Flow cell | -1              | 300                        | C <sub>2</sub>   | 74           | 137  |
| R-Cu-5  | 0.1 M KHCO <sub>3</sub>              | H-Cell    | -0.9            | 26.2                       | C <sub>2</sub>   | 64.5         | 139  |
| <b>Geometric confinement of pore and hierarchical structure</b> |                                      |           |                 |                            |  |              |      |
| Ag-Cu nanoenzyme  | 0.1 M KHCO <sub>3</sub>              | H-Cell    | -0.65           | 5 <sup>a</sup>             | C <sub>3</sub>   |              | 144  |
|   |                                      |           | -0.8            | 20 <sup>a</sup>            | C <sub>2</sub>   |              |      |
| Multi-hollow Cu <sub>2</sub> O                                  | 2 M KOH                              | Flow cell | -0.61           | 267 ± 13                   | C <sub>2+</sub>  | 75.2 ± 2.7   | 148  |
| Cu mesopore electrode (30 nm/40 nm)                             | 0.1 M KHCO <sub>3</sub>              | H-Cell    | -1.7            | 5.7                        | C <sub>2</sub> H <sub>4</sub>                                    | 38           | 151  |
| Cu mesopore electrode (30 nm/70 nm)                             |                                      |           |                 | 4.0                        | C <sub>2</sub> H <sub>6</sub>                                    | 46           |      |
| Nanoporous Cu   | 1 M KOH                              | Flow cell | -0.67           | 653                        | C <sub>2+</sub>  | 62           | 156  |
| Hollow OD-Cu  | 0.1 M KHCO <sub>3</sub>              | Flow cell | -1.4            | 14.5                       | C <sub>2</sub>   | 71.1         | 159  |
| Cu-12.5 nm  | 0.4 M KI                             | H-Cell    | -1.3            | 17                         | C <sub>2+</sub>  | 65.7         | 160  |
| Ag@Cu-p4.9  | 1 M KHCO <sub>3</sub>                | Flow cell | -1.2            | 300                        | C <sub>2+</sub>  | 73.7         | 147  |
| Cu <sub>2</sub> O@Cu <sub>2</sub> O YSNPs                       | 1 M KOH                              | Flow cell |                 | 50                         | C <sub>3</sub> H <sub>8</sub> OH                                 | 22.22 ± 0.38 | 81   |
|   |                                      |           |                 | 500                        | C <sub>2+</sub>  | 80.94 ± 4.02 |      |
| Cu <sub>2</sub> O cavity  | 1 M KOH                              | Flow cell | -0.59           | 605 ± 14                   | C <sub>2+</sub>  | 75.6 ± 1.8   | 146  |
| Multi-shelled CuO microboxes                                    | 0.1 M K <sub>2</sub> SO <sub>4</sub> | H-Cell    | -1.05           | 24.2                       | C <sub>2</sub> H <sub>4</sub>                                    | 51.3         | 197  |
| 3-Shell HoMSs   | 0.5 M KHCO <sub>3</sub>              | Flow cell | -0.82           | 513.7 ± 0.7                | C <sub>2+</sub>  | 77.0 ± 0.3%  | 153  |
| <b>Facet</b>  |                                      |           |                 |                            |  |              |      |
| HF-Cu   | 1 M KOH                              | Flow cell | -0.45           | 8.5                        | CH <sub>3</sub> CH <sub>2</sub> CH <sub>2</sub> OH               | 20           | 70   |
| Cu(100)-rich Cu hollow fiber                                    | 0.5 M KHCO <sub>3</sub>              | Flow cell | -1.94           | 2300                       | C <sub>2+</sub>  | 62.8         | 168  |
| D-Cu <sub>2</sub> O/Cu  | 0.1 M KCl                            | H-Cell    | -1.2            |                            | C <sub>2+</sub>  | 70           | 170  |
| HIF-Cu  | 0.1 M KHCO <sub>3</sub>              | H-Cell    | -1.4            |                            | C <sub>2+</sub>  | 43           | 171  |
| Cu NC   | 0.5 M KHCO <sub>3</sub>              | Flow cell | -1.5            | 200                        | CH <sub>3</sub> COOH   | 43           | 172  |
| Cu NWs  | 0.1 M KHCO <sub>3</sub>              | H-Cell    | -1              |                            | C <sub>2</sub> H <sub>4</sub>                                    | 69.79 ± 1.44 | 174  |
| <b>Defect</b>   |                                      |           |                 |                            |  |              |      |
| Cu <sub>DS</sub>  | 0.1 M KHCO <sub>3</sub>              | Flow cell | -1.08           | 100                        | C <sub>2+</sub> alcohol  | 70           | 178  |
| Cu(100) electrode   | 0.1 M KHCO <sub>3</sub>              | H-Cell    | -1              |                            | C <sub>2+</sub>  | 76           | 179  |
| CuCl, CuBr, CuI   | 0.1 M KHCO <sub>3</sub>              | H-Cell    | -1.1            |                            | C <sub>2+</sub>  | 72           | 181  |
| Sb/CuO(V <sub>O</sub> )   | 0.1 M KHCO <sub>3</sub>              | H-Cell    | -1              | 500                        | C <sub>2</sub> H <sub>4</sub>                                    | 89.3 ± 1.1   | 180  |
| CuS <sub>x</sub> -DSV   | 0.1 M KHCO <sub>3</sub>              | H-Cell    | -1.05           | 3.1 ± 0.2                  | CH <sub>3</sub> CH <sub>2</sub> CH <sub>2</sub> OH               | 15.4 ± 1     | 98   |
|   |                                      | Flow cell | -0.85           | 9.9                        |  | —            |      |
| <b>Chemical state effect</b>                                    |                                      |           |                 |                            |  |              |      |
| CuSiO <sub>3</sub> @SiO <sub>2</sub>                            | 0.1 M KHCO <sub>3</sub>              | H-Cell    | -1              | 9                          | C <sub>2+</sub>  | 70           | 183  |
| OD-Cu-45  | 0.1 M KHCO <sub>3</sub>              | H-Cell    | -1.04           | 0.35                       | C <sub>2+</sub>  | 65           | 185  |
| Annealed Cu   | 0.5 M KHCO <sub>3</sub>              | H-Cell    | -0.35           | 2.1                        | CO   | 48           | 186  |
|   |                                      |           | -0.58           | 3.7                        | HCOOH  | 39           |      |
| Cu/Cu <sub>2</sub> O aerogel                                    | 0.1 M KCl                            | H-Cell    | -1              | 32.55                      | C <sub>2</sub> H <sub>5</sub> OH                                 | 41.2         | 188  |
| Cu <sub>4</sub> O   | 0.5 M KHCO <sub>3</sub>              | H-Cell    | -1              | 44.7                       | C <sub>2</sub> H <sub>4</sub>                                    | 45           | 192  |
| Cu-APC  | 0.2 M NaHCO <sub>3</sub>             | H-Cell    | -0.78           | 7.9                        | CO   | 92           | 190  |
| Cu <sub>2</sub> O/CuO-PC  | 1 M KOH                              | Flow cell | -1.58           | 578                        | C <sub>2</sub> H <sub>4</sub>                                    | 65.12        | 195  |

<sup>a</sup> Product formation rate (10<sup>-8</sup> mol s<sup>-1</sup> g<sup>-1</sup>).

derived carbon aerogels (CA) doped with trace Cu nanoparticles (SF-Cu/CA-1) through a facile self-assembly strategy. They observed that the carbon aerogel substrate greatly enhanced the catalytic performance by improving the electron transfer efficiency and increasing the active site exposure area of the catalyst. Additionally, it controlled the rapid desorption of \*CO, leading to a selectivity of 83.06% for CO and a notable inhibition of hydrogen precipitation.<sup>204</sup> Specifically designed carbon

substrates can synergistically interact with metal nanoparticle catalysts, promoting the formation of multi-carbon products. The synergistic effect between graphitic carbon nitride substrates (g-C<sub>3</sub>N<sub>4</sub>) and medium-sized Cu nanoparticles was determined by Han *et al.* They collectively achieved a faradaic efficiency of up to 62.8% at a partial current density of 188 mA cm<sup>-2</sup> for CH<sub>3</sub>COOH during the electrochemical reduction of CO. *In situ* experimental results demonstrated that the Cu/C<sub>3</sub>N<sub>4</sub>





interface enhances the hydrogenation of CO, resulting in the formation of  $^*CHO$  intermediates. The  $^*CHO$  intermediates migrate smoothly to Cu nanoparticles (NPs) for subsequent coupling and protonation, resulting in the formation of  $CH_3-COOH$ . The remarkable stability of the substrate enables Cu (25 nm)-CN-3 to steadily reduce CO at  $100\text{ mA cm}^{-2}$  for over 120 h.<sup>68</sup> The carbon substrate occasionally acts as an intermediate donor in  $CO_2$  electroreduction, enabling the formation of a tandem-like catalyst. Hou *et al.* developed an *in situ*  $^*CO$  generation and spillover strategy by designing a single Ni atom on a pyridinic N-enriched carbon support with a sodalite (SOD) topology, referred to as Ni-SOD/NC. The substrate serves as a donor, supplying adjacent Cu nanoparticles (NPs) with  $^*CO$  intermediates. This strategy resulted in a remarkable  $C_2H_4$  selectivity of 62.5% at an industrial-level partial current density of  $160\text{ mA cm}^{-2}$ .<sup>58</sup> This study showcases the unusual potential of the substrate to function as a tandem catalyst by regulating the intermediates.<sup>205</sup> Additionally, it highlights the significance of Ni-SOD/NC as a medium in forming  $C_2H_4$ .

In addition to carbon materials, covalent frameworks are extensively utilized as substrates due to their exceptional electrical conductivity and ability to stabilize domains. Yang *et al.* developed a Cu-based catalyst confined within a rationally designed covalent triazine framework (CTF-B), exhibiting a  $CuN_2Cl_2$  coordination structure. They achieved a faradaic efficiency of 81.3% for overall  $CO_2$  reduction towards hydrocarbon ( $C_2H_4$  up to 30.6%). Direct experimental evidence substantiated that CTF-B significantly enhances the adsorption of  $^*CO$ , thereby accelerating subsequent C–C coupling on Cu. Additionally, the favourable chemically confined environment of CTF-B plays a crucial role in selectively producing  $CH_3COOH$  as the sole liquid product.<sup>206</sup> Nonetheless, the intricate fabrication process of covalent frameworks restricts their broader utilization in comparison to carbon materials. Utilizing diverse substrates positively influences active site exposure, modulation of catalyst charge environment, and overall system stability. This approach is an effective strategy to regulate intermediate behaviour and obtain high-value chemicals.

## 5.2. Tandem catalyst design

In the electroreduction of  $CO_2$  over Cu to generate multi-carbon products, Cu is frequently hindered by slow thermodynamics or kinetics in specific reaction steps, resulting in inadequate coverage of crucial intermediates and posing challenges in achieving substantial selectivity for desired products. The tandem catalyst strategy offers a solution to this problem by integrating  $C_1$ -producing Au, Ag, or monoatomic catalysts with Cu-based catalysts that exhibit high activity for  $C_{2+}$  products.<sup>72,177</sup> The design of the catalyst structure can significantly influence the direction and duration of intermediate migration, particularly for the crucial CO intermediate.<sup>26</sup> Schuhmann *et al.* mimicked the “substrate channelling effect” of the enzyme by using a nanoparticle catalyst for  $CO_2$  electroreduction. The catalyst featured an Ag core surrounded by a porous Cu shell with multiple active sites. In this setup, CO was initially

generated on the Ag core and subsequently transferred to the adjacent porous Cu shell for subsequent C–C coupling (Fig. 11a). This catalyst configuration greatly enhanced the production of  $C_{2+}$  products at lower overpotentials.<sup>144</sup> Similarly, Huang *et al.* designed Cu@Ag core-shell nanoparticles with a tuneable shell thickness for ECR. They discovered that an optimal Ag shell thickness significantly enhanced the CO absorption at the Ag/Cu interface, thereby facilitating rapid charge transfer. Consequently, the overall selectivity for  $CO_2$  reduction reached 67.6%, and the selectivity for  $C_2H_4$  reached 32.2% (Fig. 11b and c).<sup>207</sup>

Another strategy for achieving a tandem catalyst effect is to directly apply the segmented catalyst layer on the GDE using an airbrushing technique. Wu *et al.* designed segmented gas-diffusion electrodes (s-GDEs), in which the CO selective catalyst layer (CL) Ag NP section at the inlet reduced  $CO_2$  to CO, and the subsequent  $C_{2+}$  selective segment coated with Cu NPs converted CO to  $C_{2+}$  products. This segmented structure significantly prolonged the residence time of the crucial CO intermediate and significantly enhanced the  $CO_2$  conversion rate, as demonstrated in Fig. 11d and e. They also observed a 250% increase in  $j_{C_{2+}}$ , compared to pure Cu by optimizing the Cu : Ag area ratio to 1.00 : 0.05 (Fig. 11f–h). Furthermore, they developed a Cu/Fe–N–C s-GDE demonstrating a tandem effect similar to the Cu/Ag segmented catalyst. The same segmented hypothesis was experimentally confirmed by the work of Zhang.<sup>208</sup> These findings underscore the feasibility and advantages of regulating intermediate transport in the design of cascade catalysts.<sup>209</sup> The cascade catalyst strategy can effectively break down the complex multi-step ECR process into segmented and simplified steps, enabling precise modulation of the behaviour of key intermediates, particularly CO, during the formation of multi-carbon products. However, selecting and designing the structure of cascade catalysts pose significant challenges in achieving desired products.

## 5.3. Surface additive effect

The surface additive strategy typically involves the introduction of molecules onto the catalyst surface, including immobilized organometallic complex catalysts, MOFs, COFs, and metal-free polymer catalysts, to modify the surface charge environment. This approach is commonly referred to as surface functionalization (Fig. 12a).<sup>210</sup> Among the various strategies for surface functionalization, the most common strategy for surface functionalization is introducing the organic molecular polymer due to the flexible and adjustable nature of the preparation. This section will focus on this particular approach.

Applying an organic polymer coating on the catalyst surface enables the modulation of key intermediate coverage at the catalyst–polymer interface during ECR. Zhuang *et al.* reported a facile method to boost the selectivity of polycrystalline Cu towards  $C_{2+}$  products by coating the Cu surface with a 50 nm thick film of polyaniline (Cu/PANI). This resulted in a remarkable increase in the faradaic efficiency (FE) of  $C_{2+}$  hydrocarbons, from 15% to 60%, at  $-1.1\text{ V vs. RHE}$  in  $KHCO_3$  solutions. *In situ* infrared spectroscopy confirmed that the enhanced coverage of





**Fig. 11** (a) Schematic illustration for the mechanism of the cascade reaction on the Ag–Cu nanoenzyme in ECR (left). The mechanism of active (red) or inactive (black) nanoenzyme cascades occurs in a specific potential window (right). Reproduced from ref. 144. Copyright 2019 American Chemical Society. (b) Product distribution of CO and C<sub>2</sub> for the Cu@Ag NPs at –1.1 V vs. RHE, the thickness of the silver shell continually grows to form Cu@Ag-2, Cu@Ag-3 and Cu@Ag-4 NPs. (c) Schematic diagram of tandem catalysis for ECR on Cu/Ag core–shell NPs. Reproduced from ref. 206. Copyright 2021 Wiley-VCH. (d) Schematic of stacked gas-diffusion electrodes (s-GDE), arrows: reaction and mass transport of the proposed tandem reaction process in the catalyst layer. (e) Schematic of the s-GDE preparation procedure. The geometries of six s-GDEs (from E1 to E6) include a constant size of the Ag CL (0.20 cm × 0.50 cm) and a varied size of the Cu CL (0.20–2.00 cm × 0.50 cm) (left). Schematic representation of the decrease in the mass activity of C<sub>2+</sub> and the decrease in CO concentration along the y-axis of the s-GDE (right). (f) Current density–voltage curve for Cu/Ag (1.00 : 0.05) s-GDE and (1.00 : 1.00) s-GDE. The graduated colour axis represents the average \*CO surface coverage in the Cu-CL for a given Cu/Ag area ratio, voltage and C<sub>2+</sub> current density. (g) Simulation curves of Cu CL local  $\theta_{CO}$  for five Cu/Ag area ratios at a C<sub>2+</sub> current density of 550 mA cm<sup>-2</sup>. (h) Average local  $\theta_{CO}$  in Cu-CL versus Cu/Ag area ratios at a C<sub>2+</sub> current density of 550 mA cm<sup>-2</sup>. Reproduced from ref. 208. Copyright 2022 Nature.

\*CO at the Cu/polyaniline interface plays a significant role in improving the selectivity towards C<sub>2+</sub> hydrocarbons (Fig. 12b and c).<sup>211</sup> The surface functionalization strategy was used by Sargent *et al.* to obtain CO from CO<sub>2</sub> electrolysis. They introduced a collaborative catalyst design featuring a molecule–metal catalyst interface through the functionalization of the Cu surface with a series of porphyrin-based metallic complexes. From the *in situ* characterization tests and theoretical calculations, the concentration of \*CO was greatly enhanced at the molecule–metal catalyst interface, facilitating C–C coupling and activating the reaction pathway towards C<sub>2</sub>H<sub>5</sub>OH. They achieved a CO<sub>2</sub>-to-C<sub>2</sub>H<sub>5</sub>OH faradaic efficiency of up to 41% and a partial current density of 124 mA cm<sup>-2</sup> at –0.82 V vs. RHE.<sup>212</sup> This study further highlights the potential of molecular additives to synergistically interact with Cu-based catalysts and modulate the behaviour of intermediates.

The strategy of incorporating molecular additives allows for precise modulation of the local catalytic microenvironment near the surface through the use of organic compounds, thereby enabling the regulation of intermediates and achieving high selectivity for target products.<sup>213,214</sup> Nevertheless, selecting the appropriate additive molecule to modulate the concentration and reaction tendency of desired intermediates can be a challenging task.

#### 5.4. Coverage effect

The coverage effect is an understudied catalyst design approach that controls the behaviour of key intermediates by manipulating the coverage of the substrate (CO<sub>2</sub> or CO) during CO<sub>2</sub> electroreduction. Cuenya *et al.* employed *operando* Raman spectroscopy and DFT modelling to investigate the structural changes of Cu<sub>2</sub>O nanocubes and the dynamics of surface





**Fig. 12** (a) Summary of molecularly enhanced heterogeneous electrocatalysts. Molecular-additive-modified heterogeneous catalysts, immobilized organometallic complex catalysts, MOF and COF catalysts, and metal-free polymer catalysts from top to bottom. Reproduced from ref. 209. Copyright 2020 Nature. (b) Schematic diagram of the ECR process on Cu and Cu-PANI electrodes. (c) ATR-SEIRAS spectra of ECR on the Cu and Cu-PANI electrodes, respectively, experiments were carried out in  $\text{CO}_2$  saturated 0.1 M  $\text{KHCO}_3$ . Reproduced from ref. 210. Copyright 2020 American Chemical Society. (d) Schematic representation of the ECR process on Cu/molecular complex surface, the high concentration of CO generated at the interface favours the ethanol pathway instead of the ethylene pathway. (e) Molecular structure of the FeTPP(Cl) complex. (f) *In situ* Raman spectra of the Cu and FeTPP(Cl)/Cu catalysts under different applied potentials. OCP, open-circuit potential. Reproduced from ref. 211. Copyright 2020 Nature.

intermediates during the process of ECR. They observed that at high coverage of  $\text{CO}_2$ , CO molecules adsorb in a mixture of atop and bridge configurations. These configurations, favoured by structural effects, facilitate  $\text{CO}_{\text{atop}}\text{-CO}_{\text{atop}}$  and  $\text{CO}_{\text{atop}}\text{-CO}_{\text{bridge}}$  coupling while limiting  $\text{CO}_{\text{bridge}}\text{-CO}_{\text{bridge}}$  interactions. The weakly bound atop configuration does not interact with CO, thereby inhibiting CO-CO dissociation and promoting OCCO<sup>-</sup> formation. Additionally, they observed a potential-dependent intensity ratio between the Cu-CO stretching band (P2) and the CO rotation band (P1), which exhibits a volcano-like trend similar to the faradaic efficiency of multi-carbon products in  $\text{CO}_2$  electroreduction (Fig. 13a and c).<sup>215</sup>

Substrate coverage influences the conformation of reaction intermediates and the reaction pathways leading to target products in ECR. Sargent *et al.* discovered that when they decreased the concentration of CO in CO electroreduction, the product distribution was more biased towards  $\text{C}_2\text{H}_4$  production than oxygenates. Based on density functional theory results, they concluded that a lower CO coverage promotes CO dimerization, resulting in a higher density of  $^*\text{C}_2$  intermediates. Conversely, higher CO coverage facilitates the reaction of  $^*\text{C}_2$  intermediates with abundant hydroxide ions, resulting in the

formation of oxygenates. Through modulating coverage to control local CO availability, they achieved desirable product selectivity, achieving a  $\text{C}_2\text{H}_4$  faradaic efficiency of 72% at a partial current density exceeding  $800 \text{ mA cm}^{-2}$  (Fig. 13b, d, g and h).<sup>97</sup> In subsequent studies, they employed a  $^*\text{CO}_2$  modulation strategy to control the behaviour and reaction rate of  $^*\text{CO}$ . Density functional theory calculations showed that a lower  $^*\text{CO}_2$  coverage on the Cu surface reduces the coverage of  $^*\text{CO}$ , promoting the protonation of  $^*\text{CO}$  to  $^*\text{CHO}$  (Fig. 13e and f),<sup>216</sup> thereby facilitating the production of  $\text{CH}_4$  instead of  $\text{C}_2\text{H}_4$ . Consequently, they achieved a faradaic efficiency of  $\text{CH}_4$  of  $(48 \pm 2)\%$  at a partial current density of  $(108 \pm 5) \text{ mA cm}^{-2}$  under a dilute  $\text{CO}_2$  gas stream.<sup>216</sup> These studies offer valuable insights into the direct conversion of diluted  $\text{CO}_2$  or CO feedstock into target products with high selectivity, while also providing an understanding of how to regulate the local microchemical environment of the catalyst surface to modulate the behaviour of intermediates.

### 5.5. Local electrolyte microenvironment effect

Manipulating the local catalytic microenvironment constitutes another category of strategies for influencing the behaviours of



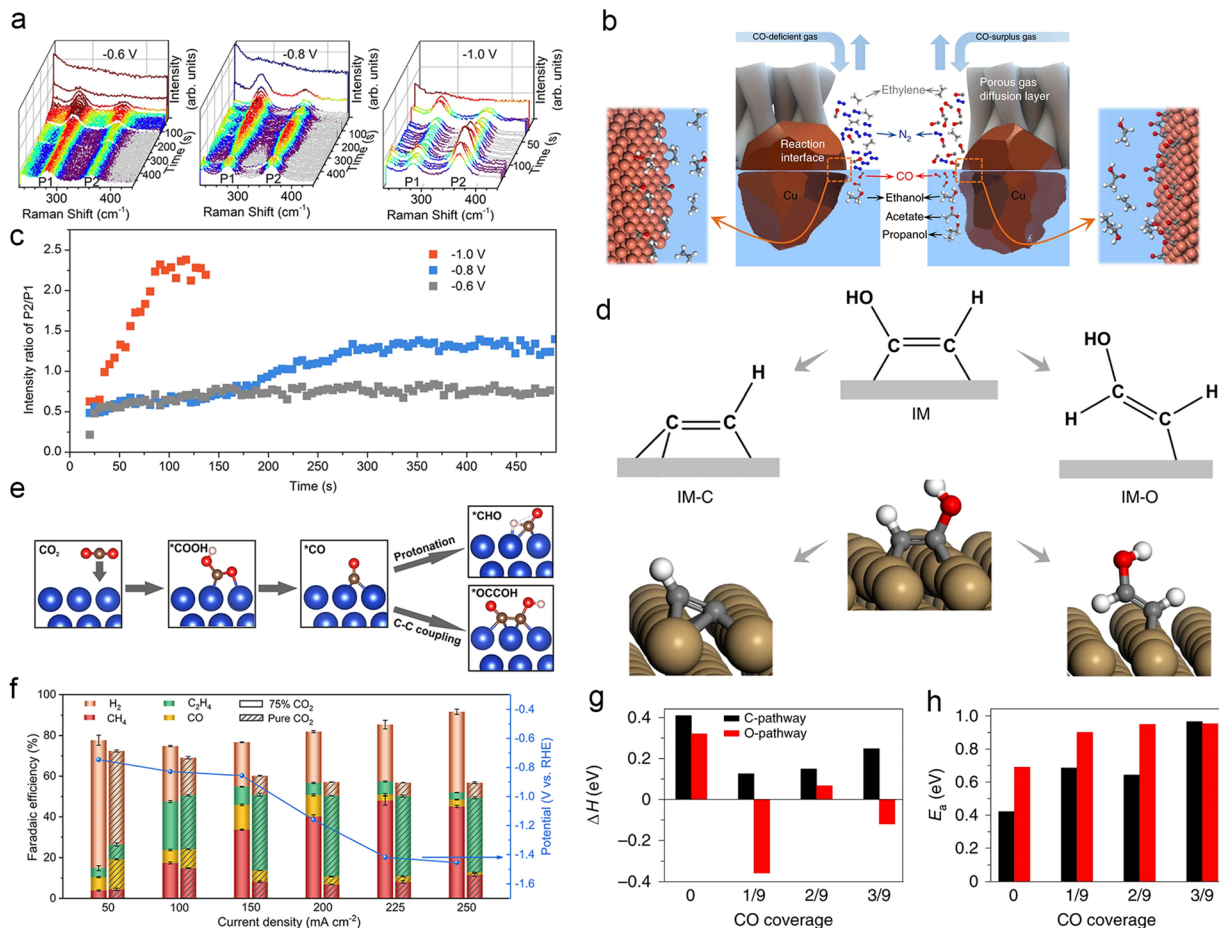


Fig. 13 (a) Raman spectra of ECR processes obtained on Cu<sub>2</sub>O nanocubes at different potentials (−0.6, −0.8, and −1.0 V vs. RHE). (c) P2/P1 peak ratio versus time at corresponding applied potentials. Reproduced from ref. 214. Copyright 2021 American Chemical Society. (b) Schematic diagram of CO reduction at the catalyst–electrolyte interface under CO-deficient and CO-excess conditions, respectively. (d) Schematic diagram of the reaction mechanism for the deoxygenation of \*CHCOH (IM) to form \*CCH (IM-C) and the alternative pathway to form \*CHCHOH (IM-O), with the corresponding geometries of IM, IM-C and IM-O on the Cu(100) surface shown below. (g) Enthalpy changes for the C- and O-pathways under different levels of CO coverage. (h) Activation energy ( $E_a$ ) of these two pathways under different levels of CO coverage. Reproduced from ref. 215. Copyright 2019 Nature. (e) Schematic diagram of the mechanism for the formation of \*CO, \*CHO and \*OCCOH from CO<sub>2</sub>. Red: O, brown: C, indigo: Cu, and pink: H. (f) Distribution of ECR gas products at different applied current densities. Experiments are carried out under pure CO<sub>2</sub> and a concentration of 75% CO<sub>2</sub>. Reproduced from ref. 97. Copyright 2020 American Chemical Society.

reaction intermediates and the selectivity of products. In this section, numerous factors contribute to variations in the microenvironment surrounding catalytic sites. Nonetheless, our primary focus will be on discussing and analysing the electrolyte composition and pH, as they have the most direct and substantial catalytic influence on adsorbed intermediates.<sup>79</sup>

In certain electrocatalytic CO<sub>2</sub>RR systems employing non-aqueous electrolytes, the inclusion of aprotic solvents like ionic liquids and organic solvents has a substantial impact on specific reactants and intermediates.<sup>217</sup> Yang *et al.* examined the influence of electrolyte additives on catalyst surface reconstruction and their electrocatalytic performance. Specifically, the electrolyte additive EDTMPA induces atomic rearrangement on the Cu surface, resulting in the formation of Cu(110) facets. Additionally, it creates an adsorption layer that enhances the utilization of both \*H and \*CO and stabilizes \*CHO intermediates during the rate-determining step of CH<sub>4</sub> generation.<sup>218</sup>

The solvent environment and proton donors also play pivotal roles in determining the CO<sub>2</sub> electroreduction mechanism.<sup>219</sup> Yogesh *et al.* proposed and reported a novel reaction mechanism, based on the lower C<sub>2</sub>H<sub>4</sub> Tafel slope in the dimethyl sulfoxide electrolyte ( $27 \pm 1$  mV dec<sup>-1</sup>) compared to the aqueous electrolyte (119 mV dec<sup>-1</sup>). This mechanism involves multiple quasi-reversible proton- and electron-transfer (PCET) steps preceding a chemical rate-determining step. Moreover, electrolyte molecules serve as carriers for proton donors, such as H<sub>2</sub>O, facilitating their efficient transport to the electrode surface. This process reduces the overpotential for CO<sub>2</sub> reduction to \*CO and indirectly promotes the production of key intermediates.<sup>77</sup>

In certain electrocatalytic CO<sub>2</sub>RR systems using aqueous solution-based electrolytes, elevated electrolyte alkalinity is advantageous for suppressing hydrogen precipitation and enhancing the selectivity of CO<sub>2</sub> conversion to multi-carbon



Table 3 Summary of the ECR performance of various Cu-based electrocatalysts

| Catalyst   | Electrolyte                                     | Cell type | $E$ (V vs. RHE)    | $j$ (mA cm <sup>-2</sup> ) | Main C <sub>2+</sub> product            | FE (%)     | Ref. |
|--|---|-----------|--------------------|----------------------------|---|------------|------|
| <b>Substrate effect</b>                              |   |           |                    |                            |   |            |      |
| CuSiO <sub>3</sub> @SiO <sub>2</sub>                 | 0.1 M KHCO <sub>3</sub>                         | H-Cell    | -1.1               | 9                          | C <sub>2+</sub>                         | ~70        | 183  |
| Cu-g-C <sub>3</sub> N <sub>4</sub> /MoS <sub>2</sub> | 0.5 M KHCO <sub>3</sub>                         | H-Cell    | -0.67              | 78                         | CH <sub>3</sub> OH                      | 19.7       | 202  |
| SF-Cu/CA-1   | 0.1 M KHCO <sub>3</sub>                         | H-Cell    | -1.26              | 29.4                       | CO                                      | 83.06      | 204  |
| Cu/NPC   | 0.2 M KHCO <sub>3</sub>                         | H-Cell    | -1.05              | 12.5                       | C <sub>2+</sub> alcohols                | 73.3       | 205  |
| CTF-Cu   | 0.3 M KCl                                       | H-Cell    | -1.55 <sup>a</sup> |                            | CH <sub>4</sub>                         | 72         | 206  |
| <b>Tandem catalyst strategy</b>                      |   |           |                    |                            |   |            |      |
| Cu@Ag-2 NPs  | 1 M KOH   | Flow cell | -1.1               | 22.7                       | C <sub>2+</sub>                         | 67.6       | 207  |
| Cu/Fe-N-C s-GDE                                      | 0.5 M KOH                                       | Flow cell | 3.38               | 1071.7                     | C <sub>2+</sub>                         | 89.3       | 209  |
| Ag-Cu nanozyme                                       | 0.1 M KHCO <sub>3</sub>                         | H-Cell    | -0.65              | 5 <sup>b</sup>             | C <sub>3</sub>                          |            | 144  |
|  |   |           | -0.8               | 20 <sup>b</sup>            | C <sub>2</sub>                          |            |      |
| <b>Surface additive effect</b>                       |   |           |                    |                            |   |            |      |
| Cu/PANI  | 0.1 M KHCO <sub>3</sub>                         | H-Cell    | -1.2               | 6.2                        | C <sub>2+</sub> hydrocarbons            | 80         | 211  |
| FeTPP[Cl]/Cu   | 1 M KHCO <sub>3</sub>                           | Flow cell | -0.82              | 124                        | C <sub>2</sub> H <sub>5</sub> OH        | 41         | 212  |
| Cu@NH <sub>2</sub>                                   | 1 M KOH   | Flow cell | -0.75              | 150                        | CH <sub>3</sub> COOH                    | 51.5       | 213  |
| CuPPc  | 0.1 M KHCO <sub>3</sub>                         | H-Cell    | -1.25              | 18                         | CH <sub>4</sub>                         | 55         | 214  |
| <b>Coverage effect</b>                               |   |           |                    |                            |   |            |      |
| Cu-PTFE  | 1 M KHCO <sub>3</sub>                           | Flow cell | -1.416             | 108 ± 5                    | CH <sub>4</sub>                         | 48 ± 2     | 216  |
| Cu oxide nanoparticles                               | 1 M KOH   | Flow cell | -0.44              | 800                        | C <sub>2</sub> H <sub>4</sub> (2.5% CO) | 72         | 97   |
| <b>Local electrolyte microenvironment effect</b>     |   |           |                    |                            |   |            |      |
| IL/Cu <sub>3</sub> (BTC) <sub>2</sub>                | 0.1 M KHCO <sub>3</sub>                         | H-Cell    |                    | 34.2                       | C <sub>2</sub> H <sub>4</sub>           | 77.3       | 217  |
| Commercial polycrystalline Cu                        | 0.5 M KHCO <sub>3</sub>                         | Flow cell |                    | 192 ± 6                    | CH <sub>4</sub>                         | 64 ± 2     | 218  |
| Graphite/carbon                                      | 10 M KOH  | Flow cell | -0.165             | 275                        | C <sub>2</sub> H <sub>4</sub>           | 70         | 220  |
| NPs/Cu/PTFE electrode                                |   |           |                    |                            |   |            |      |
| Porous Cu nanosheets                                 | 3 M KCl & 0.05 M H <sub>2</sub> SO <sub>4</sub> | Flow cell | -1.07              | 560 ± 20                   | C <sub>2+</sub>                         | 83.7 ± 1.4 | 221  |

<sup>a</sup> Potential vs. SHE. <sup>b</sup> Product formation rate (10<sup>-8</sup> mol s<sup>-1</sup> g<sup>-1</sup>).

products. Sargent *et al.* determined that within the highly alkaline electrolytic environment (10 M KOH), CO<sub>2</sub> in the electrolyte predominantly localizes at the catalyst layer's immediate reaction interface, extending to the first 120 nm. This is in contrast to the less alkaline catalytic environment (1 M KOH). The limited presence of H\* coverage within this narrow range of catalytic sites results in reduced competition for hydrogen precipitation. Furthermore, even under moderately negative potentials, the localized intensity of the CO<sub>2</sub> reaction enhances the \*CO coverage. This hydroxide-mediated transformation significantly enhances the reaction kinetics of CO dimerization, leading to a substantial improvement in electrocatalytic performance.<sup>220</sup> However, in highly alkaline environments where carbonate is formed from CO<sub>2</sub>, the use of an acidic electrolyte effectively resolves the issue. This mitigates the intense competition for hydrogen precipitation. Huang *et al.* achieved synergistic modulation of the local microenvironment by conducting CO<sub>2</sub> electroreduction in a highly acidic electrolyte (pH ≤ 1). They elucidated the confinement effect, wherein species accumulate in the Helmholtz plane (*e.g.*, K<sup>+</sup> and OH<sup>-</sup>), thereby enhancing the selectivity of multi-carbon products through the kinetic reduction of \*H coverage and the thermodynamic facilitation of CO<sub>2</sub> conversion. Additionally, this effect involves K<sup>+</sup> cation interaction with the critical intermediate \*OCCO.<sup>221</sup> The presence of electrolyte not only influences the

behaviour of reaction intermediates but also alters the catalyst composition. Cui *et al.* depicted the dynamic reduction/oxidation behaviour of the OD-Cu surface. Employing *in situ* spectroscopy and isotope labelling, they unveiled that OH<sup>-</sup> radicals, resulting from swift oxygen exchange between the HCO<sub>3</sub><sup>-</sup> electrolyte and H<sub>2</sub>O, can induce the spontaneous oxidation of the Cu electrode, resulting in the formation of surface CuO<sub>x</sub> species.<sup>196</sup>

Besides modulating intermediates through direct adjustments to the composition and pH of the electrolyte, modifying the catalyst configuration also plays a role in altering the electrolyte composition and governing the behaviour of intermediates.<sup>153,222</sup> This indirect regulatory approach may partially overlap with the previously discussed concept of morphological structure engineering, highlighting the significance and ubiquity of the locally regulated catalytic environment.

## 6. Conclusions

Electrocatalytic reduction of CO<sub>2</sub> to a wide range of high value chemicals is a promising technology for energy storage and conversion. Modulating the concentration and residence time of crucial intermediates over Cu-based catalysts provides new insights into product distributions' regulation. Guided by a number of previous works, numerous investigations on



catalyst composition engineering, catalyst morphology design, and electrolysis equipment and conditions have been conducted, wherein the synergistic effects of some strategies have also been created. With these efforts, the performance of Cu-based catalysts has taken a qualitative leap forward from decades ago. To promote the practical feasibility of the electrocatalytic CO<sub>2</sub> reduction, more elaborate characterisation instruments for observing intermediates and catalyst designs should be built upon and improved to suit more realistic catalytic conditions.

This review focuses on catalyst designs that modulate the reaction process of key intermediates on the catalyst surface. We provided a detailed overview of the basic outline of electrocatalytic CO<sub>2</sub> reduction (ECR) firstly, including the universal reaction apparatus, the commonly used evaluation parameters for electrocatalytic CO<sub>2</sub> reduction (overpotential, current density, faradaic efficiency, Tafel slope and other parameters), and a comprehensive overview of the ECR experimental mechanism based on a wealth of experimental results and theoretical studies subsequently. Drawing from our observations of intermediate reactions on the catalyst surface, we present an overview of advanced catalyst designs aimed at manipulating intermediate behaviour, encompassing their residence time and inclination to engage in various reaction pathways. Categorizing these designs into three primary groups, we differentiate them based on their ability to finely or comprehensively modulate intermediates through various strategies: heteroatom doping (both metallic and non-metallic), morphological structure engineering (involving grain boundaries, pore confinement, hierarchical structures, facets, defects, and chemical states), and local catalytic environment engineering (encompassing the substrate effect, tandem catalyst strategy, surface additives, coverage effect, and local electrolyte microenvironment effect). Although each strategy presents distinct advantages, the synergistic combination of multiple strategies frequently results in enhanced electrocatalytic performance.<sup>157,188,223,224</sup> As an illustration, co-doping the metallic element Ag with the non-metallic element S serves to not only efficiently adjust the electronic structure of the catalyst in favour of CH<sub>3</sub>OH generation but also to effectively suppress the hydrogen precipitation reaction. These synergistic interactions significantly enhanced the selectivity and reactivity of the CH<sub>3</sub>OH product.<sup>225</sup>

Despite the substantial recent enhancements in the electrocatalytic performance of Cu-based catalysts for the CO<sub>2</sub>RR, the development of competent catalyst designs founded on precise reaction mechanisms and the achievement of large-scale industrial applications still pose formidable challenges. In conclusion, we recognize several impending challenges and anticipate shifts in future research priorities:

(1) Firstly, the mechanism underlying CO<sub>2</sub> electroreduction, particularly the formation of C<sub>2+</sub> products, remains enigmatic and demands rigorous exploration. The current CO<sub>2</sub>RR mechanism is primarily derived through retroactive extrapolation of the distribution of catalytic products, in conjunction with theoretical calculations. However, this approach raises concerns about objectivity and veracity. Obtaining immediate data on reaction intermediates through *in situ* catalytic instrumentation can offer

genuine and precise insights into the reaction mechanism. Consequently, progress in high-resolution *in situ* characterization techniques is imperative to discern the nuanced behavioural traits of intricate intermediates and explore their reaction mechanisms. Additionally, it is essential to establish a correlation between the evolution of the catalyst surface and the reaction process, extending beyond the observation of intermediate dynamics alone. This correlation is crucial for identifying the active sites and comprehending the reaction mechanism. Yang *et al.*, based on information about the evolution of AgCu catalysts during the CO<sub>2</sub>RR obtained through time-sequential electron microscopy and elemental mapping studies, confirm that the catalytically active sites consist of the metallic state of Cu and underscore the importance of AgCu phase boundaries in the CO<sub>2</sub>RR.<sup>226</sup> Furthermore, *operando* high-energy-resolution fluorescence detection X-ray absorption spectroscopy (HERFD-XAS) furnishes compelling spectroscopic evidence demonstrating the rupture of chemical bonds between ligands and the surfaces of Cu nanoparticles. This confirms that the true active sites are the undercoordinated metallic Cu nanograins in the CO<sub>2</sub>RR.<sup>227</sup> Furthermore, while simulating reaction scenarios through theoretical calculations significantly aids in structural design and high-throughput catalyst screening, it is crucial to acknowledge that mechanistic investigations cannot rely solely on theoretical calculations.

(2) Secondly, the microenvironment of the electrocatalytic system is still under-researched. The interplay between the catalyst, electrolyte, and gas reactant at the three-phase interface has a complex and significant effect on the dehydrogenation and coupling of the reaction intermediates, which demands further exploration. Investigating the interaction between the local reaction environment and mass/electron transfer within this interface will shed light on the influence of microenvironments on electrocatalytic activity and selectivity.

For example, the CO<sub>2</sub> concentration in waste gases emitted from modern industrial production is typically low, typically ranging from 6% to 15%. However, the current electrocatalytic system employs highly purified reactant feedstock, which not only significantly reduces the efficiency of CO<sub>2</sub> feedstock utilization but also increases the cost and energy consumption associated with the purification process. To attain high-performance CO<sub>2</sub> electroreduction for the production of valuable chemicals at nearly realistic feed concentrations, it becomes imperative to investigate the reaction microenvironment under conditions of dilute CO<sub>2</sub> feed and develop catalyst designs that enhance crucial intermediates. At present, experimental investigations into low-purity CO<sub>2</sub> feeds primarily focus on discerning and quantifying variations in the adsorption strength of intermediates under different feedstock coverages, while the evolution of catalytic active sites during the reduction process has received limited attention.<sup>216,228–230</sup> Indeed, feedstocks with varying coverages are susceptible to interacting differently with active sites in a complex local catalytic microenvironment, leading to changes or transfers of active sites. Therefore, comprehending the impact of the microenvironment on the catalytic reaction is essential for unravelling the catalytic mechanism and enhancing catalytic performance.



(3) Kinetics studies of electrocatalytic processes have received less attention compared to their thermodynamic counterparts. Product distribution is not solely influenced by thermodynamic energy barriers but also by kinetic factors. However, most existing research has relied on higher-order theoretical calculations and simulations to analyse changes in the thermodynamic energy barriers of reaction steps in electrocatalytic processes. A comprehensive and structured kinetic theory simulation system is still lacking, limiting investigations to a superficial understanding of reaction rates in general. Electrochemical parameters such as reaction rate and Tafel slope which evaluate electrocatalytic kinetics could demonstrate a wealth of potential information about the rate-determining step during the reaction process.<sup>231</sup> Establishing a correlation between the kinetic mechanism underlying these parameters and the thermodynamic DFT simulations is of critical importance for a profound comprehension of the electrocatalytic mechanism. In addition, the study of the kinetics of catalytic reactions can help to increase the rate of catalytic reactions, and thus gradually approach the industrialization requirement of high current or even realize the industrialization of catalytic reactions.

(4) The potential of machine learning and computational chemistry in ECR remains largely untapped. In the realm of ECR, these tools can aid in catalyst screening. Machine learning enables the construction of a robust, large-scale catalyst performance database by swiftly evaluating theoretical studies and facilitating rational catalyst design. This expedites the discovery and optimization of highly efficient and selective catalysts. On the other hand, computational chemistry simulates the electrocatalytic microenvironment, catalyst surface morphology, and reactant adsorption configuration to predict catalyst performance, thus guiding the experimental design and minimizing trial-and-error endeavours. Nevertheless, using machine learning and computational chemistry in ECR guarantees further exploration.

In conclusion, electrocatalytic conversion of CO<sub>2</sub> into valuable chemicals and fuels holds promise as an environmentally friendly technology capable of mitigating the greenhouse effect and advancing carbon neutrality. Nevertheless, its advancement continues to face substantial challenges, including the unclear formation mechanism of CO<sub>2</sub> electroreduction to C<sub>2+</sub> products, the insufficiently studied electrocatalytic microenvironments in these systems, and the relatively uncharted territory of dynamics research and machine learning. Overcoming these challenges requires the application of advanced, synergistic catalyst strategies, improved product analysis techniques, and state-of-the-art *in situ* characterization technologies. Predictably, a new trend in obtaining higher-order CO<sub>2</sub>RR products will involve the design of efficient Cu-based catalysts with a focus on modulating the behaviour of reaction intermediates.

## Data availability

This review article does not include any experimental or computational data.

## Author contributions

L. Xie conceptualized the work, performed the investigations and wrote the manuscript. Y. J., W. Z. and S. D. provided resources and supervised the work. Y. Z. and J. Z. were involved in funding acquisition and project administration. All authors have given approval to the final version of the manuscript.

## Conflicts of interest

There are no conflicts to declare.

## Acknowledgements

Y. Z. is thankful for the support from the Natural Science Foundation of Jiangsu Province (BK20220405), National Natural Science Foundation of China (22276100), Key Laboratory for Organic Electronics & Information Displays (GZR2022010010), Nanjing Science and Technology Innovation Project for Chinese Scholars Studying Abroad (NJKCZYZZ2022-01), Research Fund for Jiangsu Distinguished Professors (RK030STP22001), and the Research startup fund of NJUPT (NY221006). W. Z. would like to acknowledge the support from the Natural Science Foundation of Jiangsu Province (BK20210189) and National Natural Science Foundation of China (22176086).

## Notes and references

- 1 Y. Zhao, M. Xi, Q. Zhang, Z. Dong, M. Ma, K. Zhou, W. Xu, J. Xing, B. Zheng, Z. Wen, X. Liu, C. P. Nielsen, Y. Liu, Y. Pan and L. Zhang, Decline in bulk deposition of air pollutants in China lags behind reductions in emissions, *Nat. Geosci.*, 2022, 15, 190–195.
- 2 P. Smith, J. Adams, D. J. Beerling, T. Beringer, K. V. Calvin, S. Fuss, B. Griscom, N. Hagemann, C. Kammann, F. Kraxner, J. C. Minx, A. Popp, P. Renforth, J. L. V. Vicente and S. Keesstra, Land-Management Options for Greenhouse Gas Removal and Their Impacts on Ecosystem Services and the Sustainable Development Goals, *Annu. Rev. Environ. Resour.*, 2019, 44, 255–286.
- 3 Z. Liu, B. Xu, Y.-J. Jiang, Y. Zhou, X. Sun, Y. Wang and W. Zhu, Photocatalytic Conversion of Methane: Current State of the Art, Challenges, and Future Perspectives, *ACS Environ. Au*, 2023, 3, 252–276.
- 4 K. de Kleijne, S. V. Hanssen, L. van Dinteren, M. A. J. Huijbregts, R. van Zelm and H. de Coninck, Limits to Paris compatibility of CO<sub>2</sub> capture and utilization, *One Earth*, 2022, 5, 168–185.
- 5 Q. Zhao, P. Yu, R. Mahendran, W. Huang, Y. Gao, Z. Yang, T. Ye, B. Wen, Y. Wu, S. Li and Y. Guo, Global climate change and human health: Pathways and possible solutions, *Eco-Environ. Health*, 2022, 1, 53–62.
- 6 S. Valluri, V. Claremboux and S. Kawatra, Opportunities and challenges in CO<sub>2</sub> utilization, *J. Environ. Sci.*, 2022, 113, 322–344.
- 7 J. Kim, B. K. Sovacool, M. Bazilian, S. Griffiths, J. Lee, M. Yang and J. Lee, Decarbonizing the iron and steel



- industry: A systematic review of sociotechnical systems, technological innovations, and policy options, *Energy Res. Social Sci.*, 2022, **89**, 102565.
- 8 P. De Luna, C. Hahn, D. Higgins, S. A. Jaffer, T. F. Jaramillo and E. H. Sargent, What would it take for renewably powered electrosynthesis to displace petrochemical processes?, *Science*, 2019, **364**, 6438.
- 9 C. Hepburn, E. Adlen, J. Beddington, E. A. Carter, S. Fuss, N. Mac Dowell, J. C. Minx, P. Smith and C. K. Williams, The technological and economic prospects for CO<sub>2</sub> utilization and removal, *Nature*, 2019, **575**, 87–97.
- 10 L. Li, X. Li, Y. Sun and Y. Xie, Rational design of electrocatalytic carbon dioxide reduction for a zero-carbon network, *Chem. Soc. Rev.*, 2022, **51**, 1234–1252.
- 11 M. Rafiq, X. Hu, Z. Ye, A. Qayum, H. Xia, L. Hu, F. Lu and P. K. Chu, Recent advances in structural engineering of 2D hexagonal boron nitride electrocatalysts, *Nano Energy*, 2022, **91**, 106661.
- 12 R. Shi, Z. Wang, Y. Zhao, G. I. N. Waterhouse, Z. Li, B. Zhang, Z. Sun, C. Xia, H. Wang and T. Zhang, Room-temperature electrochemical acetylene reduction to ethylene with high conversion and selectivity, *Nat. Catal.*, 2021, **4**, 565–574.
- 13 H. Xie, T. Wang, J. Liang, Q. Li and S. Sun, Cu-based nanocatalysts for electrochemical reduction of CO<sub>2</sub>, *Nano Today*, 2018, **21**, 41–54.
- 14 L.-X. Liu, J. Fu, L.-P. Jiang, J.-R. Zhang, W. Zhu and Y. Lin, Highly Efficient Photoelectrochemical Reduction of CO<sub>2</sub> at Low Applied Voltage Using 3D Co-Pi/BiVO<sub>4</sub>/SnO<sub>2</sub> Nanosheet Array Photoanodes, *ACS Appl. Mater. Interfaces*, 2019, **11**, 26024–26031.
- 15 X. Yang, K. Li, G. Wang, X. Li, P. Zhou, S. Ding, Z. Lyu, Y.-C. Chang, Y. Zhou and W. Zhu, 2D Catalysts for CO<sub>2</sub> Photoreduction: Discussing Structure Efficiency Strategies and Prospects for Scaled Production Based on Current Progress, *Chem. –Eur. J.*, 2022, **28**, e202201881.
- 16 G. Wang, X. Li, X. Yang, L.-X. Liu, Y. Cai, Y. Wu, S. Wang, H. Li, Y. Zhou, Y. Wang and Y. Zhou, Metal-Based Aerogels Catalysts for Electrocatalytic CO<sub>2</sub> Reduction, *Chem. –Eur. J.*, 2022, **28**, e202201834.
- 17 X. Fu, T. Ren, S. Jiao, Z. Tian, J. Yang and Q. Li, Development strategies and improved photocatalytic CO<sub>2</sub> reduction performance of metal halide perovskite nanocrystals, *J. Energy Chem.*, 2023, **83**, 397–422.
- 18 T. L. Biel-Nielsen, T. A. Hatton, S. N. B. Villadsen, J. S. Jakobsen, J. L. Bonde, A. M. Spormann and P. L. Fosbøl, Electrochemistry-Based CO<sub>2</sub> Removal Technologies, *ChemSusChem*, 2023, **16**, e202202345.
- 19 T. Stolar, A. Prašnikar, V. Martinez, B. Karadeniz, A. Bjelić, G. Mali, T. Friščić, B. Likozar and K. Užarević, Scalable Mechanochemical Amorphization of Bimetallic Cu–Zn MOF-74 Catalyst for Selective CO<sub>2</sub> Reduction Reaction to Methanol, *ACS Appl. Mater. Interfaces*, 2021, **13**, 3070–3077.
- 20 L.-L. Ling, W. Yang, P. Yan, M. Wang and H.-L. Jiang, Light-Assisted CO<sub>2</sub> Hydrogenation over Pd<sub>3</sub>Cu@UiO-66 Promoted by Active Sites in Close Proximity, *Angew. Chem., Int. Ed.*, 2022, **61**, e202116396.
- 21 H. Huang, R. Shi, Z. Li, J. Zhao, C. Su and T. Zhang, Triphase Photocatalytic CO<sub>2</sub> Reduction over Silver-Decorated Titanium Oxide at a Gas–Water Boundary, *Angew. Chem., Int. Ed.*, 2022, **61**, e202200802.
- 22 Y. Dai and Y. Xiong, Control of selectivity in organic synthesis via heterogeneous photocatalysis under visible light, *Nano Res. Energy*, 2022, **1**, e9120006.
- 23 X. Tan, C. Yu, Y. Ren, S. Cui, W. Li and J. Qiu, Recent advances in innovative strategies for the CO<sub>2</sub> electroreduction reaction, *Energy Environ. Sci.*, 2021, **14**, 765–780.
- 24 K. M. Choi, D. Kim, B. Rungtaweivoranit, C. A. Trickett, J. T. D. Barmanbek, A. S. Alshammari, P. Yang and O. M. Yaghi, Plasmon-Enhanced Photocatalytic CO<sub>2</sub> Conversion within Metal–Organic Frameworks under Visible Light, *J. Am. Chem. Soc.*, 2017, **139**, 356–362.
- 25 H. Du, J. Fu, L.-X. Liu, S. Ding, Z. Lyu, Y.-C. Chang, X. Jin, F. O. Kengara, B. Song, Q. Min, J.-J. Zhu, D. Du, C. Gu, Y. Lin, J.-S. Hu and W. Zhu, Recent progress in electrochemical reduction of carbon monoxide toward multi-carbon products, *Mater. Today*, 2022, **59**, 182–199.
- 26 J. Liu, X. Guo, Z. Lyu, R.-B. Song, P. Zhou, S. Ding, Y. Zhou, L.-P. Jiang, Y. Lin and W. Zhu, A novel tandem reactor design based on nano-Cu electrocatalysts and microbial biocatalysts for converting CO<sub>2</sub> into ethylene and acetate, *Green Chem.*, 2023, **25**, 5712–5720.
- 27 K. Li, Y. Cai, X. Yang, S. Wang, C. Teng, Y. Tian, Q. Min and W. Zhu, H<sub>2</sub>S Involved Photocatalytic System: A Novel Syngas Production Strategy by Boosting the Photoreduction of CO<sub>2</sub> While Recovering Hydrogen from the Environmental Toxicant, *Adv. Funct. Mater.*, 2022, **32**, 2113002.
- 28 J. Ahn, S. Park, D. Oh, Y. Lim, J. S. Nam, J. Kim, W. Jung and I.-D. Kim, Rapid Joule Heating Synthesis of Oxide-Socketed High-Entropy Alloy Nanoparticles as CO<sub>2</sub> Conversion Catalysts, *ACS Nano*, 2023, **17**, 12188–12199.
- 29 T. Tang, Z. Wang and J. Guan, Optimizing the Electrocatalytic Selectivity of Carbon Dioxide Reduction Reaction by Regulating the Electronic Structure of Single-Atom M–N–C Materials, *Adv. Funct. Mater.*, 2022, **32**, 2111504.
- 30 J. Wang, Q. Hao, H. Zhong, K. Li and X. Zhang, Ligand centered electrocatalytic efficient CO<sub>2</sub> reduction reaction at low overpotential on single-atom Ni regulated molecular catalyst, *Nano Res.*, 2022, **15**, 5816–5823.
- 31 J. Liu, D. Yang, Y. Zhou, G. Zhang, G. Xing, Y. Liu, Y. Ma, O. Terasaki, S. Yang and L. Chen, Tricycloquinazoline-Based 2D Conductive Metal–Organic Frameworks as Promising Electrocatalysts for CO<sub>2</sub> Reduction, *Angew. Chem., Int. Ed.*, 2021, **60**, 14473–14479.
- 32 M. Jun, C. Kwak, S. Y. Lee, J. Joo, J. M. Kim, D. J. Im, M. K. Cho, H. Baik, Y. J. Hwang, H. Kim and K. Lee, Microfluidics-Assisted Synthesis of Hierarchical Cu<sub>2</sub>O Nanocrystal as C<sub>2</sub>-Selective CO<sub>2</sub> Reduction Electrocatalyst, *Small Methods*, 2022, **6**, 2200074.





- 33 Y. Wu, H. Du, P. Li, X. Zhang, Y. Yin and W. Zhu, Heterogeneous Electrocatalysis of Carbon Dioxide to Methane, *Methane*, 2023, **2**, 148–175.
- 34 Y. Yu, J. Wang, Q. Chen, J. Urpelainen, Q. Ding, S. Liu and B. Zhang, Decarbonization efforts hindered by China's slow progress on electricity market reforms, *Nat Sustainability*, 2023, **6**, 1006–1015.
- 35 J. Liu, Y. Cai, R. Song, S. Ding, Z. Lyu, Y.-C. Chang, H. Tian, X. Zhang, D. Du, W. Zhu, Y. Zhou and Y. Lin, Recent progress on single-atom catalysts for CO<sub>2</sub> electroreduction, *Mater. Today*, 2021, **48**, 95–114.
- 36 S. Jin, Z. Hao, K. Zhang, Z. Yan and J. Chen, Advances and Challenges for the Electrochemical Reduction of CO<sub>2</sub> to CO: From Fundamentals to Industrialization, *Angew. Chem., Int. Ed.*, 2021, **60**, 20627–20648.
- 37 S. Malkhandi and B. S. Yeo, Electrochemical conversion of carbon dioxide to high value chemicals using gas-diffusion electrodes, *Curr. Opin. Chem. Eng.*, 2019, **26**, 112–121.
- 38 G. Wen, B. Ren, X. Wang, D. Luo, H. Dou, Y. Zheng, R. Gao, J. Gostick, A. Yu and Z. Chen, Continuous CO<sub>2</sub> electrolysis using a CO<sub>2</sub> exsolution-induced flow cell, *Nat. Energy*, 2022, **7**, 978–988.
- 39 T. Yamamoto, D. A. Tryk, A. Fujishima and H. Ohata, Production of syngas plus oxygen from CO<sub>2</sub> in a gas-diffusion electrode-based electrolytic cell, *Electrochim. Acta*, 2002, **47**, 3327–3334.
- 40 T. Burdyny and W. A. Smith, CO<sub>2</sub> reduction on gas-diffusion electrodes and why catalytic performance must be assessed at commercially-relevant conditions, *Energy Environ. Sci.*, 2019, **12**, 1442–1453.
- 41 F. Li, D. R. MacFarlane and J. Zhang, Recent advances in the nanoengineering of electrocatalysts for CO<sub>2</sub> reduction, *Nanoscale*, 2018, **10**, 6235–6260.
- 42 Y. Hori, I. Takahashi, O. Koga and N. Hoshi, Selective Formation of C<sub>2</sub> Compounds from Electrochemical Reduction of CO<sub>2</sub> at a Series of Copper Single Crystal Electrodes, *J. Phys. Chem. B*, 2002, **106**, 15–17.
- 43 Y. Hori, I. Takahashi, O. Koga and N. Hoshi, Electrochemical reduction of carbon dioxide at various series of copper single crystal electrodes, *J. Mol. Catal. A: Chem.*, 2003, **199**, 39–47.
- 44 D. W. DeWulf, T. Jin and A. J. Bard, Electrochemical and Surface Studies of Carbon Dioxide Reduction to Methane and Ethylene at Copper Electrodes in Aqueous Solutions, *J. Electrochem. Soc.*, 1989, **136**, 1686.
- 45 T. K. Todorova, M. W. Schreiber and M. Fontecave, Mechanistic Understanding of CO<sub>2</sub> Reduction Reaction (CO<sub>2</sub>RR) Toward Multicarbon Products by Heterogeneous Copper-Based Catalysts, *ACS Catal.*, 2020, **10**, 1754–1768.
- 46 D. Hursán and C. Janáky, Operando characterization of continuous flow CO<sub>2</sub> electrolyzers: current status and future prospects, *Chem. Commun.*, 2023, **59**, 1395–1414.
- 47 Y. Kim, S. Park, S.-J. Shin, W. Choi, B. K. Min, H. Kim, W. Kim and Y. J. Hwang, Time-resolved observation of C–C coupling intermediates on Cu electrodes for selective electrochemical CO<sub>2</sub> reduction, *Energy Environ. Sci.*, 2020, **13**, 4301–4311.
- 48 M. He, X. Chang, T.-H. Chao, C. Li, W. A. Goddard III, M.-J. Cheng, B. Xu and Q. Lu, Selective Enhancement of Methane Formation in Electrochemical CO<sub>2</sub> Reduction Enabled by a Raman-Inactive Oxygen-Containing Species on Cu, *ACS Catal.*, 2022, **12**, 6036–6046.
- 49 Z. Pan, K. Wang, K. Ye, Y. Wang, H.-Y. Su, B. Hu, J. Xiao, T. Yu, Y. Wang and S. Song, Intermediate Adsorption States Switch to Selectively Catalyze Electrochemical CO<sub>2</sub> Reduction, *ACS Catal.*, 2020, **10**, 3871–3880.
- 50 Z.-Z. Wu, X.-L. Zhang, Z.-Z. Niu, F.-Y. Gao, P.-P. Yang, L.-P. Chi, L. Shi, W.-S. Wei, R. Liu, Z. Chen, S. Hu, X. Zheng and M.-R. Gao, Identification of Cu(100)/Cu(111) Interfaces as Superior Active Sites for CO Dimerization During CO<sub>2</sub> Electroreduction, *J. Am. Chem. Soc.*, 2022, **144**, 259–269.
- 51 F. Shao, J. K. Wong, Q. H. Low, M. Iannuzzi, J. Li and J. Lan, In situ spectroelectrochemical probing of CO redox landscape on copper single-crystal surfaces, *Proc. Natl. Acad. Sci. U. S. A.*, 2022, **119**, e2118166119.
- 52 X. Tan, K. Sun, Z. Zhuang, B. Hu, Y. Zhang, Q. Liu, C. He, Z. Xu, C. Chen, H. Xiao and C. Chen, Stabilizing Copper by a Reconstruction-Resistant Atomic Cu–O–Si Interface for Electrochemical CO<sub>2</sub> Reduction, *J. Am. Chem. Soc.*, 2023, **145**, 8656–8664.
- 53 Y. Yang, S. Louisia, S. Yu, J. Jin, I. Roh, C. Chen, M. V. Fonseca Guzman, J. Feijóo, P.-C. Chen, H. Wang, C. J. Pollock, X. Huang, Y.-T. Shao, C. Wang, D. A. Muller, H. D. Abruña and P. Yang, Operando studies reveal active Cu nanograins for CO<sub>2</sub> electroreduction, *Nature*, 2023, **614**, 262–269.
- 54 Y. Zheng, H. Yao, R. Di, Z. Xiang, Q. Wang, F. Lu, Y. Li, G. Yang, Q. Ma and Z. Zhang, Water coordinated on Cu(I)-based catalysts is the oxygen source in CO<sub>2</sub> reduction to CO, *Nat. Commun.*, 2022, **13**, 2577.
- 55 B. Deng, X. Zhao, Y. Li, M. Huang, S. Zhang and F. Dong, Active site identification and engineering during the dynamic evolution of copper-based catalysts for electrocatalytic CO<sub>2</sub> reduction, *Sci. China: Chem.*, 2023, **66**, 78–95.
- 56 S. Zhao, Y. Yang and Z. Tang, Insight into Structural Evolution, Active Sites, and Stability of Heterogeneous Electrocatalysts, *Angew. Chem., Int. Ed.*, 2022, **61**, e202110186.
- 57 Y. Jiang, X. Wang, D. Duan, C. He, J. Ma, W. Zhang, H. Liu, R. Long, Z. Li, T. Kong, X. J. Loh, L. Song, E. Ye and Y. Xiong, Structural Reconstruction of Cu<sub>2</sub>O Superparticles toward Electrocatalytic CO<sub>2</sub> Reduction with High C<sub>2</sub><sup>+</sup> Products Selectivity, *Adv. Sci.*, 2022, **9**, 2105292.
- 58 J. Chen, D. Wang, X. Yang, W. Cui, X. Sang, Z. Zhao, L. Wang, Z. Li, B. Yang, L. Lei, J. Zheng, L. Dai and Y. Hou, Accelerated Transfer and Spillover of Carbon Monoxide through Tandem Catalysis for Kinetics-boosted Ethylene Electrosynthesis, *Angew. Chem., Int. Ed.*, 2023, **62**, e202215406.
- 59 J. Li, H. Zeng, X. Dong, Y. Ding, S. Hu, R. Zhang, Y. Dai, P. Cui, Z. Xiao, D. Zhao, L. Zhou, T. Zheng, J. Xiao, J. Zeng and C. Xia, Selective CO<sub>2</sub> electrolysis to CO using



- isolated antimony alloyed copper, *Nat. Commun.*, 2023, **14**, 340.
- 60 K. J. P. Schouten, Y. Kwon, C. J. M. van der Ham, Z. Qin and M. T. M. Koper, A new mechanism for the selectivity to C1 and C2 species in the electrochemical reduction of carbon dioxide on copper electrodes, *Chem. Sci.*, 2011, **2**, 1902–1909.
- 61 X. Lv, L. Shang, S. Zhou, S. Li, Y. Wang, Z. Wang, T.-K. Sham, C. Peng and G. Zheng, Electron-Deficient Cu Sites on Cu<sub>3</sub>Ag<sub>1</sub> Catalyst Promoting CO<sub>2</sub> Electroreduction to Alcohols, *Adv. Energy Mater.*, 2020, **10**, 2001987.
- 62 H.-L. Zhu, J.-R. Huang, X.-W. Zhang, C. Wang, N.-Y. Huang, P.-Q. Liao and X.-M. Chen, Highly Efficient Electroconversion of CO<sub>2</sub> into CH<sub>4</sub> by a Metal–Organic Framework with Trigonal Pyramidal Cu(I)N<sub>3</sub> Active Sites, *ACS Catal.*, 2021, **11**, 11786–11792.
- 63 L. Zhang, X.-X. Li, Z.-L. Lang, Y. Liu, J. Liu, L. Yuan, W.-Y. Lu, Y.-S. Xia, L.-Z. Dong, D.-Q. Yuan and Y.-Q. Lan, Enhanced Cuprophilic Interactions in Crystalline Catalysts Facilitate the Highly Selective Electroreduction of CO<sub>2</sub> to CH<sub>4</sub>, *J. Am. Chem. Soc.*, 2021, **143**, 3808–3816.
- 64 K. Nakata, T. Ozaki, C. Terashima, A. Fujishima and Y. Einaga, High-Yield Electrochemical Production of Formaldehyde from CO<sub>2</sub> and Seawater, *Angew. Chem., Int. Ed.*, 2014, **53**, 871–874.
- 65 J. Li, Y. Kuang, Y. Meng, X. Tian, W.-H. Hung, X. Zhang, A. Li, M. Xu, W. Zhou, C.-S. Ku, C.-Y. Chiang, G. Zhu, J. Guo, X. Sun and H. Dai, Electroreduction of CO<sub>2</sub> to Formate on a Copper-Based Electrocatalyst at High Pressures with High Energy Conversion Efficiency, *J. Am. Chem. Soc.*, 2020, **142**, 7276–7282.
- 66 L. Fan, C. Xia, P. Zhu, Y. Lu and H. Wang, Electrochemical CO<sub>2</sub> reduction to high-concentration pure formic acid solutions in an all-solid-state reactor, *Nat. Commun.*, 2020, **11**, 3633.
- 67 T. T. H. Hoang, S. Verma, S. Ma, T. T. Fister, J. Timoshenko, A. I. Frenkel, P. J. A. Kenis and A. A. Gewirth, Nanoporous Copper–Silver Alloys by Additive-Controlled Electrodeposition for the Selective Electroreduction of CO<sub>2</sub> to Ethylene and Ethanol, *J. Am. Chem. Soc.*, 2018, **140**, 5791–5797.
- 68 X. Yan, M. Zhang, Y. Chen, Y. Wu, R. Wu, Q. Wan, C. Liu, T. Zheng, R. Feng, J. Zhang, C. Chen, C. Xia, Q. Zhu, X. Sun, Q. Qian and B. Han, Synergy of Cu/C<sub>3</sub>N<sub>4</sub> Interface and Cu Nanoparticles Dual Catalytic Regions in Electrolysis of CO to Acetic Acid, *Angew. Chem., Int. Ed.*, 2023, **62**, e202301507.
- 69 M. Li, N. Song, W. Luo, J. Chen, W. Jiang and J. Yang, Engineering Surface Oxophilicity of Copper for Electrochemical CO<sub>2</sub> Reduction to Ethanol, *Adv. Sci.*, 2023, **10**, 2204579.
- 70 Y. Pang, J. Li, Z. Wang, C.-S. Tan, P.-L. Hsieh, T.-T. Zhuang, Z.-Q. Liang, C. Zou, X. Wang, P. De Luna, J. P. Edwards, Y. Xu, F. Li, C.-T. Dinh, M. Zhong, Y. Lou, D. Wu, L.-J. Chen, E. H. Sargent and D. Sinton, Efficient electrocatalytic conversion of carbon monoxide to propanol using fragmented copper, *Nat. Catal.*, 2019, **2**, 251–258.
- 71 S. Payra, S. Kanungo and S. Roy, Controlling C–C coupling in electrocatalytic reduction of CO<sub>2</sub> over Cu<sub>1–x</sub>Zn<sub>x</sub>/C, *Nanoscale*, 2022, **14**, 13352–13361.
- 72 B. Cao, F.-Z. Li and J. Gu, Designing Cu-Based Tandem Catalysts for CO<sub>2</sub> Electroreduction Based on Mass Transport of CO Intermediate, *ACS Catal.*, 2022, **12**, 9735–9752.
- 73 L.-X. Liu, X. Li, Y. Cai, H. Du, F. Liu, J.-R. Zhang, J. Fu and W. Zhu, Hierarchical S-modified Cu porous nanoflakes for efficient CO<sub>2</sub> electroreduction to formate, *Nanoscale*, 2022, **14**, 13679–13688.
- 74 K. Xiang, F. Shen, Y. Fu, L. Wu, Z. Wang, H. Yi, X. Liu, P. Wang, M. Liu, Z. Lin and H. Liu, Boosting CO<sub>2</sub> electroreduction towards C<sub>2</sub><sup>+</sup> products via CO\* intermediate manipulation on copper-based catalysts, *Environ. Sci.: Nano*, 2022, **9**, 911–953.
- 75 C. Guo, Y. Guo, Y. Shi, X. Lan, Y. Wang, Y. Yu and B. Zhang, Electrocatalytic Reduction of CO<sub>2</sub> to Ethanol at Close to Theoretical Potential via Engineering Abundant Electron-Donating Cu<sup>δ+</sup> Species, *Angew. Chem., Int. Ed.*, 2022, **61**, e202205909.
- 76 M. Zhuansun, Y. Liu, R. Lu, F. Zeng, Z. Xu, Y. Wang, Y. Yang, Z. Wang, G. Zheng and Y. Wang, Promoting CO<sub>2</sub> Electroreduction to Multi-Carbon Products by Hydrophobicity-Induced Electro-Kinetic Retardation, *Angew. Chem., Int. Ed.*, 2023, **62**, e202309875.
- 77 A. T. Chu and Y. Surendranath, Aprotic Solvent Exposes an Altered Mechanism for Copper-Catalyzed Ethylene Electrosynthesis, *J. Am. Chem. Soc.*, 2022, **144**, 5359–5365.
- 78 Y. Jiang, D. Zhong, L. Wang, J. Li, G. Hao, J. Li and Q. Zhao, Roughness Effect of Cu on Electrocatalytic CO<sub>2</sub> Reduction towards C<sub>2</sub>H<sub>4</sub>, *Chem. – Asian J.*, 2022, **17**, e202200380.
- 79 H. H. Heenen, H. Shin, G. Kastlunger, S. Overa, J. A. Gauthier, F. Jiao and K. Chan, The mechanism for acetate formation in electrochemical CO(2) reduction on Cu: selectivity with potential, pH, and nanostructuring, *Energy Environ. Sci.*, 2022, **15**, 3978–3990.
- 80 G. Cao, X. Cao, M. Shan, M. Li, X. Zhu, J. Han, Q. Ge and H. Wang, Surface cavity effect on C<sub>2</sub>H<sub>4</sub> formation from electrochemical reduction of CO<sub>2</sub> as studied using Cu<sub>2</sub>O cubes, *J. Solid State Electrochem.*, 2022, **26**, 1527–1540.
- 81 H. Du, L.-X. Liu, P. Li, Q. Min, S. Guo and W. Zhu, Enriching Reaction Intermediates in Multishell Structured Copper Catalysts for Boosted Propanol Electrosynthesis from Carbon Monoxide, *ACS Nano*, 2023, **17**, 8663–8670.
- 82 H. Takeda, Y. Monma and O. Ishitani, Highly Functional Dinuclear CuI-Complex Photosensitizers for Photocatalytic CO<sub>2</sub> Reduction, *ACS Catal.*, 2021, **11**, 11973–11984.
- 83 H. Yuan, B. Cheng, J. Lei, L. Jiang and Z. Han, Promoting photocatalytic CO<sub>2</sub> reduction with a molecular copper purpurin chromophore, *Nat. Commun.*, 2021, **12**, 1835.
- 84 M. Wang, V. Nikolaou, A. Loiodice, I. D. Sharp, A. Llobet and R. Buonsanti, Tandem electrocatalytic CO<sub>2</sub> reduction



- with Fe-porphyrins and Cu nanocubes enhances ethylene production, *Chem. Sci.*, 2022, **13**, 12673–12680.
- 85 A. A. Peterson, F. Abild-Pedersen, F. Studt, J. Rossmeisl and J. K. Nørskov, How copper catalyzes the electroreduction of carbon dioxide into hydrocarbon fuels, *Energy Environ. Sci.*, 2010, **3**, 1311–1315.
- 86 F. Calle-Vallejo and M. T. M. Koper, Theoretical Considerations on the Electroreduction of CO to C<sub>2</sub> Species on Cu(100) Electrodes, *Angew. Chem., Int. Ed.*, 2013, **52**, 7282–7285.
- 87 P. Hirunsit, W. Soodsawang and J. Limtrakul, CO<sub>2</sub> Electrochemical Reduction to Methane and Methanol on Copper-Based Alloys: Theoretical Insight, *J. Phys. Chem. C*, 2015, **119**, 8238–8249.
- 88 Q. Kong, X. An, Q. Liu, L. Xie, J. Zhang, Q. Li, W. Yao, A. Yu, Y. Jiao and C. Sun, Copper-based catalysts for the electrochemical reduction of carbon dioxide: progress and future prospects, *Mater. Horiz.*, 2023, **10**, 698–721.
- 89 F. A. Armstrong and J. Hirst, Reversibility and efficiency in electrocatalytic energy conversion and lessons from enzymes, *Proc. Natl. Acad. Sci. U. S. A.*, 2011, **108**, 14049–14054.
- 90 S. Nitopi, E. Bertheussen, S. B. Scott, X. Liu, A. K. Engstfeld, S. Horch, B. Seger, I. E. L. Stephens, K. Chan, C. Hahn, J. K. Nørskov, T. F. Jaramillo and I. Chorkendorff, Progress and Perspectives of Electrochemical CO<sub>2</sub> Reduction on Copper in Aqueous Electrolyte, *Chem. Rev.*, 2019, **119**, 7610–7672.
- 91 L. Wang, S. A. Nitopi, E. Bertheussen, M. Orazov, C. G. Morales-Guio, X. Liu, D. C. Higgins, K. Chan, J. K. Nørskov, C. Hahn and T. F. Jaramillo, Electrochemical Carbon Monoxide Reduction on Polycrystalline Copper: Effects of Potential, Pressure, and pH on Selectivity toward Multicarbon and Oxygenated Products, *ACS Catal.*, 2018, **8**, 7445–7454.
- 92 W. Ma, X. He, W. Wang, S. Xie, Q. Zhang and Y. Wang, Electrocatalytic reduction of CO<sub>2</sub> and CO to multi-carbon compounds over Cu-based catalysts, *Chem. Soc. Rev.*, 2021, **50**, 12897–12914.
- 93 W. Ma, S. Xie, T. Liu, Q. Fan, J. Ye, F. Sun, Z. Jiang, Q. Zhang, J. Cheng and Y. Wang, Electrocatalytic reduction of CO<sub>2</sub> to ethylene and ethanol through hydrogen-assisted C–C coupling over fluorine-modified copper, *Nat. Catal.*, 2020, **3**, 478–487.
- 94 A. J. Garza, A. T. Bell and M. Head-Gordon, Mechanism of CO<sub>2</sub> Reduction at Copper Surfaces: Pathways to C<sub>2</sub> Products, *ACS Catal.*, 2018, **8**, 1490–1499.
- 95 X. Wang, J. F. de Araújo, W. Ju, A. Bagger, H. Schmies, S. Kühn, J. Rossmeisl and P. Strasser, Mechanistic reaction pathways of enhanced ethylene yields during electroreduction of CO<sub>2</sub>–CO co-feeds on Cu and Cu-tandem electrocatalysts, *Nat. Nanotechnol.*, 2019, **14**, 1063–1070.
- 96 T. Cheng, H. Xiao and W. A. Goddard, Full atomistic reaction mechanism with kinetics for CO reduction on Cu(100) from ab initio molecular dynamics free-energy calculations at 298 K, *Proc. Natl. Acad. Sci. U. S. A.*, 2017, **114**, 1795–1800.
- 97 J. Li, Z. Wang, C. McCallum, Y. Xu, F. Li, Y. Wang, C. M. Gabardo, C.-T. Dinh, T.-T. Zhuang, L. Wang, J. Y. Howe, Y. Ren, E. H. Sargent and D. Sinton, Constraining CO coverage on copper promotes high-efficiency ethylene electroproduction, *Nat. Catal.*, 2019, **2**, 1124–1131.
- 98 C. Peng, G. Luo, J. Zhang, M. Chen, Z. Wang, T.-K. Sham, L. Zhang, Y. Li and G. Zheng, Double sulfur vacancies by lithium tuning enhance CO<sub>2</sub> electroreduction to n-propanol, *Nat. Commun.*, 2021, **12**, 1580.
- 99 X. Wang, Z. Wang, T.-T. Zhuang, C.-T. Dinh, J. Li, D.-H. Nam, F. Li, C.-W. Huang, C.-S. Tan, Z. Chen, M. Chi, C. M. Gabardo, A. Seifitokaldani, P. Todorović, A. Proppe, Y. Pang, A. R. Kirmani, Y. Wang, A. H. Ip, L. J. Richter, B. Scheffel, A. Xu, S.-C. Lo, S. O. Kelley, D. Sinton and E. H. Sargent, Efficient upgrading of CO to C<sub>3</sub> fuel using asymmetric C–C coupling active sites, *Nat. Commun.*, 2019, **10**, 5186.
- 100 E. L. Clark and A. T. Bell, Direct Observation of the Local Reaction Environment during the Electrochemical Reduction of CO<sub>2</sub>, *J. Am. Chem. Soc.*, 2018, **140**, 7012–7020.
- 101 X. Chang, A. Malkani, X. Yang and B. Xu, Mechanistic Insights into Electroreductive C–C Coupling between CO and Acetaldehyde into Multicarbon Products, *J. Am. Chem. Soc.*, 2020, **142**, 2975–2983.
- 102 V. S. S. Mosali, A. M. Bond and J. Zhang, Alloying strategies for tuning product selectivity during electrochemical CO<sub>2</sub> reduction over Cu, *Nanoscale*, 2022, **14**, 15560–15585.
- 103 X. Hong, H. Zhu, D. Du, Q. Zhang and Y. Li, Research Progress of Copper-Based Bimetallic Electrocatalytic Reduction of CO<sub>2</sub>, *Catalysts*, 2023, **13**, 376.
- 104 H. Tabassum, X. Yang, R. Zou and G. Wu, Surface engineering of Cu catalysts for electrochemical reduction of CO<sub>2</sub> to value-added multi-carbon products, *Chem Catal.*, 2022, **2**, 1561–1593.
- 105 F. Jia, X. Yu and L. Zhang, Enhanced selectivity for the electrochemical reduction of CO<sub>2</sub> to alcohols in aqueous solution with nanostructured Cu–Au alloy as catalyst, *J. Power Sources*, 2014, **252**, 85–89.
- 106 F. Hu, L. Yang, Y. Jiang, C. Duan, X. Wang, L. Zeng, X. Lv, D. Duan, Q. Liu, T. Kong, J. Jiang, R. Long and Y. Xiong, Ultrastable Cu Catalyst for CO<sub>2</sub> Electroreduction to Multicarbon Liquid Fuels by Tuning C–C Coupling with Cu/Ti Subsurface, *Angew. Chem., Int. Ed.*, 2021, **60**, 26122–26127.
- 107 M. Fang, Y. Ji, Y. Pi, P. Wang, Z. Hu, J.-F. Lee, H. Pang, Y. Li, Q. Shao and X. Huang, Aluminum-Doped Mesoporous Copper Oxide Nanofibers Enabling High-Efficiency CO<sub>2</sub> Electroreduction to Multicarbon Products, *Chem. Mater.*, 2022, **34**, 9023–9030.
- 108 T. Zheng, C. Liu, C. Guo, M. Zhang, X. Li, Q. Jiang, W. Xue, H. Li, A. Li, C.-W. Pao, J. Xiao, C. Xia and J. Zeng, Copper-catalysed exclusive CO<sub>2</sub> to pure formic acid conversion via single-atom alloying, *Nat. Nanotechnol.*, 2021, **16**, 1386–1393.



- 109 Y. Xie, P. Ou, X. Wang, Z. Xu, Y. C. Li, Z. Wang, J. E. Huang, J. Wicks, C. McCallum, N. Wang, Y. Wang, T. Chen, B. T. W. Lo, D. Sinton, J. C. Yu, Y. Wang and E. H. Sargent, High carbon utilization in CO<sub>2</sub> reduction to multi-carbon products in acidic media, *Nat. Catal.*, 2022, **5**, 564–570.
- 110 A. Xu, S.-F. Hung, A. Cao, Z. Wang, N. Karmodak, J. E. Huang, Y. Yan, A. Sedighian Rasouli, A. Ozden, F.-Y. Wu, Z.-Y. Lin, H.-J. Tsai, T.-J. Lee, F. Li, M. Luo, Y. Wang, X. Wang, J. Abed, Z. Wang, D.-H. Nam, Y. C. Li, A. H. Ip, D. Sinton, C. Dong and E. H. Sargent, Copper/alkaline earth metal oxide interfaces for electrochemical CO<sub>2</sub>-to-alcohol conversion by selective hydrogenation, *Nat. Catal.*, 2022, **5**, 1081–1088.
- 111 D. Higgins, A. T. Landers, Y. Ji, S. Nitopi, C. G. Morales-Guio, L. Wang, K. Chan, C. Hahn and T. F. Jaramillo, Guiding Electrochemical Carbon Dioxide Reduction toward Carbonyls Using Copper Silver Thin Films with Interphase Miscibility, *ACS Energy Lett.*, 2018, **3**, 2947–2955.
- 112 L. Wang, D. C. Higgins, Y. Ji, C. G. Morales-Guio, K. Chan, C. Hahn and T. F. Jaramillo, Selective reduction of CO to acetaldehyde with CuAg electrocatalysts, *Proc. Natl. Acad. Sci. U. S. A.*, 2020, **117**, 12572–12575.
- 113 C. Zhu, A. Chen, J. Mao, G. Wu, S. Li, X. Dong, G. Li, Z. Jiang, Y. Song, W. Chen and W. Wei, Cu–Pd Bimetallic Gas Diffusion Electrodes for Electrochemical Reduction of CO<sub>2</sub> to C<sub>2</sub><sup>+</sup> Products, *Small Struct.*, 2023, **4**, 2200328.
- 114 Z. Wei, S. Yue, S. Gao, M. Cao and R. Cao, Synergetic effects of gold-doped copper nanowires with low Au content for enhanced electrocatalytic CO<sub>2</sub> reduction to multicarbon products, *Nano Res.*, 2023, **16**, 7777–7783.
- 115 D. Tan, B. Wulan, J. Ma, X. Cao and J. Zhang, Electrochemical-driven reconstruction for efficient reduction of carbon dioxide into alcohols, *Chem Catal.*, 2023, **3**, 100512.
- 116 M. Zheng, P. Wang, X. Zhi, K. Yang, Y. Jiao, J. Duan, Y. Zheng and S.-Z. Qiao, Electrocatalytic CO<sub>2</sub>-to-C<sub>2</sub><sup>+</sup> with Ampere-Level Current on Heteroatom-Engineered Copper via Tuning \*CO Intermediate Coverage, *J. Am. Chem. Soc.*, 2022, **144**, 14936–14944.
- 117 G. Iijima, H. Yamaguchi, T. Inomata, H. Yoto, M. Ito and H. Masuda, Methanethiol SAMs Induce Reconstruction and Formation of Cu<sup>+</sup> on a Cu Catalyst under Electrochemical CO<sub>2</sub> Reduction, *ACS Catal.*, 2020, **10**, 15238–15249.
- 118 J. M. Wang, Q. Y. Zhu, J. H. Lee, T. G. Woo, Y. X. Zhang, W.-D. Jang and T. K. Kim, Asymmetric gradient orbital interaction of hetero-diatomic active sites for promoting C – C coupling, *Nat. Commun.*, 2023, **14**, 3808.
- 119 Y. Shi, Y. Wang, C.-L. Dong, T. T. T. Nga, D. Wei, J. Wang, X. Zhao, M. Wang, K. Zhang, M. Li, F. Dong and S. Shen, Localized Geometry Determined Selectivity of Iodide-Derived Copper for Electrochemical CO<sub>2</sub> Reduction, *Adv. Energy Mater.*, 2023, **13**, 2203896.
- 120 H. Lu, L. Li, Q. Wu, S. Mu, R. Zhao, X. Zheng, C. Long, Q. Li, H. Liu and C. Cui, Cu<sup>+</sup>-Mediated CO Coordination for Promoting C–C Coupling for CO<sub>2</sub> and CO Electroreduction, *ACS Appl. Mater. Interfaces*, 2023, **15**, 13228–13237.
- 121 R. Wang, J. Liu, Q. Huang, L.-Z. Dong, S.-L. Li and Y.-Q. Lan, Partial Coordination-Perturbed Bi-Copper Sites for Selective Electroreduction of CO<sub>2</sub> to Hydrocarbons, *Angew. Chem., Int. Ed.*, 2021, **60**, 19829–19835.
- 122 C. Peng, G. Luo, Z. Xu, S. Yan, J. Zhang, M. Chen, L. Qian, W. Wei, Q. Han and G. Zheng, Lithiation-Enabled High-Density Nitrogen Vacancies Electrocatalyze CO<sub>2</sub> to C<sub>2</sub> Products, *Adv. Mater.*, 2021, **33**, 2103150.
- 123 K. K. Patra, S. Park, H. Song, B. Kim, W. Kim and J. Oh, Operando Spectroscopic Investigation of a Boron-Doped CuO Catalyst and Its Role in Selective Electrochemical C–C Coupling, *ACS Appl. Energy Mater.*, 2020, **3**, 11343–11349.
- 124 J. Zhang, X. Mao, B. Pan, J. Xu, X. Ding, N. Han, L. Wang, Y. Wang and Y. Li, Surface promotion of copper nanoparticles with alumina clusters derived from layered double hydroxide accelerates CO<sub>2</sub> reduction to ethylene in membrane electrode assemblies, *Nano Res.*, 2023, **16**, 4685–4690.
- 125 M. Li, Y. Ma, J. Chen, R. Lawrence, W. Luo, M. Sacchi, W. Jiang and J. Yang, Residual Chlorine Induced Cationic Active Species on a Porous Copper Electrocatalyst for Highly Stable Electrochemical CO<sub>2</sub> Reduction to C<sub>2</sub><sup>+</sup>, *Angew. Chem., Int. Ed.*, 2021, **60**, 11487–11493.
- 126 L. Wang, S. Nitopi, A. B. Wong, J. L. Snider, A. C. Nielander, C. G. Morales-Guio, M. Orazov, D. C. Higgins, C. Hahn and T. F. Jaramillo, Electrochemically converting carbon monoxide to liquid fuels by directing selectivity with electrode surface area, *Nat. Catal.*, 2019, **2**, 702–708.
- 127 X. Feng, K. Jiang, S. Fan and M. W. Kanan, Grain-Boundary-Dependent CO<sub>2</sub> Electroreduction Activity, *J. Am. Chem. Soc.*, 2015, **137**, 4606–4609.
- 128 S. Liu, J. Xiao, X. F. Lu, J. Wang, X. Wang and X. W. Lou, Efficient Electrochemical Reduction of CO<sub>2</sub> to HCOOH over Sub-2 nm SnO<sub>2</sub> Quantum Wires with Exposed Grain Boundaries, *Angew. Chem., Int. Ed.*, 2019, **58**, 8499–8503.
- 129 D. Cheng, G. Zhang, L. Li, X. Shi, S. Zhen, Z.-J. Zhao and J. Gong, Guiding catalytic CO<sub>2</sub> reduction to ethanol with copper grain boundaries, *Chem. Sci.*, 2023, **14**, 7966–7972.
- 130 H. S. Jeon, J. Timoshenko, C. Rettenmaier, A. Herzog, A. Yoon, S. W. Chee, S. Oener, U. Hejral, F. T. Haase and B. Roldan Cuenya, Selectivity Control of Cu Nanocrystals in a Gas-Fed Flow Cell through CO<sub>2</sub> Pulsed Electroreduction, *J. Am. Chem. Soc.*, 2021, **143**, 7578–7587.
- 131 X. Feng, K. Jiang, S. Fan and M. W. Kanan, A Direct Grain-Boundary-Activity Correlation for CO Electroreduction on Cu Nanoparticles, *ACS Cent. Sci.*, 2016, **2**, 169–174.
- 132 J. Zhang, Y. Wang, Z. Li, S. Xia, R. Cai, L. Ma, T. Zhang, J. Ackley, S. Yang, Y. Wu and J. Wu, Grain Boundary-Derived Cu<sup>+</sup>/Cu<sup>0</sup> Interfaces in CuO Nanosheets for Low Overpotential Carbon Dioxide Electroreduction to Ethylene, *Adv. Sci.*, 2022, **9**, 2200454.
- 133 Q. Wu, R. Du, P. Wang, G. I. N. Waterhouse, J. Li, Y. Qiu, K. Yan, Y. Zhao, W.-W. Zhao, H.-J. Tsai, M.-C. Chen, S.-F. Hung, X. Wang and G. Chen, Nanograin-Boundary-



- Abundant Cu<sub>2</sub>O-Cu Nanocubes with High C<sub>2</sub><sup>+</sup> Selectivity and Good Stability during Electrochemical CO<sub>2</sub> Reduction at a Current Density of 500 mA/cm<sup>2</sup>, *ACS Nano*, 2023, **17**, 12884–12894.
- 134 Y. Oh, J. Park, Y. Kim, M. Shim, T.-S. Kim, J. Y. Park and H. R. Byon, Coverage of capping ligands determining the selectivity of multi-carbon products and morphological evolution of Cu nanocatalysts in electrochemical reduction of CO<sub>2</sub>, *J. Mater. Chem. A*, 2021, **9**, 11210–11218.
- 135 P. Qi, L. Zhao, Z. Deng, H. Sun, H. Li, Q. Liu, X. Li, Y. Lian, J. Cheng, J. Guo, Y. Cui and Y. Peng, Revisiting the Grain and Valence Effect of Oxide-Derived Copper on Electrocatalytic CO<sub>2</sub> Reduction Using Single Crystal Cu(111) Foils, *J. Phys. Chem. Lett.*, 2021, **12**, 3941–3950.
- 136 Z. Chen, T. Wang, B. Liu, D. Cheng, C. Hu, G. Zhang, W. Zhu, H. Wang, Z.-J. Zhao and J. Gong, Grain-Boundary-Rich Copper for Efficient Solar-Driven Electrochemical CO<sub>2</sub> Reduction to Ethylene and Ethanol, *J. Am. Chem. Soc.*, 2020, **142**, 6878–6883.
- 137 C. Yang, H. Shen, A. Guan, J. Liu, T. Li, Y. Ji, A. M. Al-Enizi, L. Zhang, L. Qian and G. Zheng, Fast cooling induced grain-boundary-rich copper oxide for electrocatalytic carbon dioxide reduction to ethanol, *J. Colloid Interface Sci.*, 2020, **570**, 375–381.
- 138 Z.-x. Yang, X. Wen, L.-j. Gao, J. Zhang, R.-p. Wei, X.-m. Pan and G.-m. Xiao, Facilitating CO<sub>2</sub> electroreduction to C<sub>2</sub>H<sub>4</sub> through facile regulating {100} & {111} grain boundary of Cu<sub>2</sub>O, *Catal. Commun.*, 2023, **174**, 106595.
- 139 C. Chen, X. Sun, X. Yan, Y. Wu, M. Liu, S. Liu, Z. Zhao and B. Han, A strategy to control the grain boundary density and Cu<sup>+</sup>/Cu<sup>0</sup> ratio of Cu-based catalysts for efficient electroreduction of CO<sub>2</sub> to C<sub>2</sub> products, *Green Chem.*, 2020, **22**, 1572–1576.
- 140 Q. Lei, H. Zhu, K. Song, N. Wei, L. Liu, D. Zhang, J. Yin, X. Dong, K. Yao, N. Wang, X. Li, B. Davaasuren, J. Wang and Y. Han, Investigating the Origin of Enhanced C<sub>2</sub><sup>+</sup> Selectivity in Oxide-/Hydroxide-Derived Copper Electrodes during CO<sub>2</sub> Electroreduction, *J. Am. Chem. Soc.*, 2020, **142**, 4213–4222.
- 141 H. Sun, L. Chen, L. Xiong, K. Feng, Y. Chen, X. Zhang, X. Yuan, B. Yang, Z. Deng, Y. Liu, M. H. Rummeli, J. Zhong, Y. Jiao and Y. Peng, Promoting ethylene production over a wide potential window on Cu crystallites induced and stabilized via current shock and charge delocalization, *Nat. Commun.*, 2021, **12**, 6823.
- 142 D. Zhong, L. Zhang, Q. Zhao, D. Cheng, W. Deng, B. Liu, G. Zhang, H. Dong, X. Yuan, Z. Zhao, J. Li and J. Gong, Concentrating and activating carbon dioxide over AuCu aerogel grain boundaries, *J. Chem. Phys.*, 2020, **152**(204703).
- 143 X. Liu, J. Li, Y. Xue, M. Gong, C. R. Cabrera, L. Yao and Z. Hu, Electrochemical CO<sub>2</sub> reduction to C<sub>2</sub><sup>+</sup> products with Cu-oleylamine based nanoparticles synthesized by simple thermal treatment, *Fuel*, 2023, **348**, 128498.
- 144 P. B. O'Mara, P. Wilde, T. M. Benedetti, C. Andronescu, S. Cheong, J. J. Gooding, R. D. Tilley and W. Schuhmann, Cascade Reactions in Nanozymes: Spatially Separated Active Sites inside Ag-Core-Porous-Cu-Shell Nanoparticles for Multistep Carbon Dioxide Reduction to Higher Organic Molecules, *J. Am. Chem. Soc.*, 2019, **141**, 14093–14097.
- 145 J. Liu, J. Fu, Y. Zhou, W. Zhu, L.-P. Jiang and Y. Lin, Controlled Synthesis of EDTA-Modified Porous Hollow Copper Microspheres for High-Efficiency Conversion of CO<sub>2</sub> to Multicarbon Products, *Nano Lett.*, 2020, **20**, 4823–4828.
- 146 L.-X. Liu, Y. Cai, H. Du, X. Lu, X. Li, F. Liu, J. Fu and J.-J. Zhu, Enriching the Local Concentration of CO Intermediates on Cu Cavities for the Electrocatalytic Reduction of CO<sub>2</sub> to C<sub>2</sub><sup>+</sup> Products, *ACS Appl. Mater. Interfaces*, 2023, **15**, 16673–16679.
- 147 Y. Zhong, X. Kong, Z. Song, Y. Liu, L. Peng, L. Zhang, X. Luo, J. Zeng and Z. Geng, Adjusting Local CO Confinement in Porous-Shell Ag@Cu Catalysts for Enhancing C–C Coupling toward CO<sub>2</sub> Electroreduction, *Nano Lett.*, 2022, **22**, 2554–2560.
- 148 P.-P. Yang, X.-L. Zhang, F.-Y. Gao, Y.-R. Zheng, Z.-Z. Niu, X. Yu, R. Liu, Z.-Z. Wu, S. Qin, L.-P. Chi, Y. Duan, T. Ma, X.-S. Zheng, J.-F. Zhu, H.-J. Wang, M.-R. Gao and S.-H. Yu, Protecting Copper Oxidation State via Intermediate Confinement for Selective CO<sub>2</sub> Electroreduction to C<sub>2</sub><sup>+</sup> Fuels, *J. Am. Chem. Soc.*, 2020, **142**, 6400–6408.
- 149 Y. Pan, H. Li, J. Xiong, Y. Yu, H. Du, S. Li, Z. Wu, S. Li, J. Lai and L. Wang, Protecting the state of Cu clusters and nanoconfinement engineering over hollow mesoporous carbon spheres for electrocatalytical C–C coupling, *Appl. Catal., B*, 2022, **306**, 121111.
- 150 D. Tan, B. Wulan, X. Cao and J. Zhang, Strong interactions of metal-support for efficient reduction of carbon dioxide into ethylene, *Nano Energy*, 2021, **89**, 106460.
- 151 K. D. Yang, W. R. Ko, J. H. Lee, S. J. Kim, H. Lee, M. H. Lee and K. T. Nam, Morphology-Directed Selective Production of Ethylene or Ethane from CO<sub>2</sub> on a Cu Mesopore Electrode, *Angew. Chem., Int. Ed.*, 2017, **56**, 796–800.
- 152 F. L. P. Veenstra, N. Ackerl, A. J. Martín and J. Pérez-Ramírez, Laser-Microstructured Copper Reveals Selectivity Patterns in the Electrocatalytic Reduction of CO<sub>2</sub>, *Chem*, 2020, **6**, 1707–1722.
- 153 C. Liu, M. Zhang, J. Li, W. Xue, T. Zheng, C. Xia and J. Zeng, Nanoconfinement Engineering over Hollow Multi-Shell Structured Copper towards Efficient Electrocatalytical C–C coupling, *Angew. Chem., Int. Ed.*, 2022, **61**, e202113498.
- 154 S. Popović, M. Smiljanić, P. Jovanović, J. Vavra, R. Buonsanti and N. Hodnik, Stability and Degradation Mechanisms of Copper-Based Catalysts for Electrochemical CO<sub>2</sub> Reduction, *Angew. Chem., Int. Ed.*, 2020, **59**, 14736–14746.
- 155 F. Franco, C. Rettenmaier, H. S. Jeon and B. Roldan Cuenya, Transition metal-based catalysts for the electrochemical CO<sub>2</sub> reduction: from atoms and molecules to nanostructured materials, *Chem. Soc. Rev.*, 2020, **49**, 6884–6946.



- 156 J.-J. Lv, M. Jouny, W. Luc, W. Zhu, J.-J. Zhu and F. Jiao, A Highly Porous Copper Electrocatalyst for Carbon Dioxide Reduction, *Adv. Mater.*, 2018, **30**, 1803111.
- 157 J.-Y. Kim, D. Hong, J.-C. Lee, H. G. Kim, S. Lee, S. Shin, B. Kim, H. Lee, M. Kim, J. Oh, G.-D. Lee, D.-H. Nam and Y.-C. Joo, Quasi-graphitic carbon shell-induced Cu confinement promotes electrocatalytic CO<sub>2</sub> reduction toward C<sub>2</sub><sup>+</sup> products, *Nat. Commun.*, 2021, **12**, 3765.
- 158 W.-G. Cui, Y.-T. Li, L. Yu, H. Zhang and T.-L. Hu, Zeolite-Encapsulated Ultrasmall Cu/ZnOx Nanoparticles for the Hydrogenation of CO<sub>2</sub> to Methanol, *ACS Appl. Mater. Interfaces*, 2021, **13**, 18693–18703.
- 159 J. Liu, Q. Fan, X. Chen, S. Kuang, T. Yan, H. Liu, S. Zhang and X. Ma, Hollow Copper Nanocubes Promoting CO<sub>2</sub> Electroreduction to Multicarbon Products, *Ind. Eng. Chem. Res.*, 2022, **61**, 18250–18257.
- 160 Z. Chen, Y. Song, Z. Zhang, Y. Cai, H. Liu, W. Xie and D. Deng, Mechanically induced Cu active sites for selective C-C coupling in CO<sub>2</sub> electroreduction, *J. Energy Chem.*, 2022, **74**, 198–202.
- 161 C. Xiao and J. Zhang, Architectural Design for Enhanced C<sub>2</sub> Product Selectivity in Electrochemical CO<sub>2</sub> Reduction Using Cu-Based Catalysts: A Review, *ACS Nano*, 2021, **15**, 7975–8000.
- 162 D. Tan, J. Zhang, L. Yao, X. Tan, X. Cheng, Q. Wan, B. Han, L. Zheng and J. Zhang, Multi-shelled CuO microboxes for carbon dioxide reduction to ethylene, *Nano Res.*, 2020, **13**, 768–774.
- 163 F. Chang, M. Xiao, R. Miao, Y. Liu, M. Ren, Z. Jia, D. Han, Y. Yuan, Z. Bai and L. Yang, Copper-Based Catalysts for Electrochemical Carbon Dioxide Reduction to Multicarbon Products, *Electrochem. Energy Rev.*, 2022, **5**, 4.
- 164 R. He, Y.-C. Wang, X. Wang, Z. Wang, G. Liu, W. Zhou, L. Wen, Q. Li, X. Wang, X. Chen, J. Zeng and J. G. Hou, Facile synthesis of pentacle gold-copper alloy nanocrystals and their plasmonic and catalytic properties, *Nat. Commun.*, 2014, **5**, 4327.
- 165 Y. Zhao, X.-G. Zhang, N. Bodappa, W.-M. Yang, Q. Liang, P. M. Radjenovica, Y.-H. Wang, Y.-J. Zhang, J.-C. Dong, Z.-Q. Tian and J.-F. Li, Elucidating electrochemical CO<sub>2</sub> reduction reaction processes on Cu(hkl) single-crystal surfaces by in situ Raman spectroscopy, *Energy Environ. Sci.*, 2022, **15**, 3968–3977.
- 166 K. J. P. Schouten, Z. Qin, E. Pérez Gallent and M. T. M. Koper, Two Pathways for the Formation of Ethylene in CO Reduction on Single-Crystal Copper Electrodes, *J. Am. Chem. Soc.*, 2012, **134**, 9864–9867.
- 167 Y. Huang, A. D. Handoko, P. Hirunsit and B. S. Yeo, Electrochemical Reduction of CO<sub>2</sub> Using Copper Single-Crystal Surfaces: Effects of CO\* Coverage on the Selective Formation of Ethylene, *ACS Catal.*, 2017, **7**, 1749–1756.
- 168 C. Zhu, Y. Song, X. Dong, G. Li, A. Chen, W. Chen, G. Wu, S. Li, W. Wei and Y. Sun, Ampere-level CO<sub>2</sub> reduction to multicarbon products over a copper gas penetration electrode, *Energy Environ. Sci.*, 2022, **15**, 5391–5404.
- 169 R. Du, Q. Wu, S. Zhang, P. Wang, Z. Li, Y. Qiu, K. Yan, G. I. N. Waterhouse, P. Wang, J. Li, Y. Zhao, W.-W. Zhao, X. Wang and G. Chen, Cu-C(O) Interfaces Deliver Remarkable Selectivity and Stability for CO<sub>2</sub> Reduction to C<sub>2</sub><sup>+</sup> Products at Industrial Current Density of 500 mA cm<sup>-2</sup>, *Small*, 2023, **19**, 2301289.
- 170 F. Chang, J. Wei, Y. Liu, W. Wang, L. Yang and Z. Bai, Surface/interface reconstruction in-situ on Cu<sub>2</sub>O catalysts with high exponential facets toward enhanced electrocatalysis CO<sub>2</sub> reduction to C<sub>2</sub><sup>+</sup> products, *Appl. Surf. Sci.*, 2023, **611**, 155773.
- 171 C. Han, V. Kundi, Z. Ma, C. Y. Toe, P. Kumar, C. Tsounis, J. Jiang, S. Xi, Z. Han, X. Lu, R. Amal and J. Pan, Differentiating the Impacts of Cu<sub>2</sub>O Initial Low- and High-Index Facets on Their Reconstruction and Catalytic Performance in Electrochemical CO<sub>2</sub> Reduction Reaction, *Adv. Funct. Mater.*, 2023, **33**, 2210938.
- 172 P. Zhu, C. Xia, C.-Y. Liu, K. Jiang, G. Gao, X. Zhang, Y. Xia, Y. Lei, H. N. Alshareef, T. P. Senftle and H. Wang, Direct and continuous generation of pure acetic acid solutions via electrocatalytic carbon monoxide reduction, *Proc. Natl. Acad. Sci. U. S. A.*, 2021, **118**, e2010868118.
- 173 F. Scholten, K.-L. C. Nguyen, J. P. Bruce, M. Heyde and B. Roldan Cuenya, Identifying Structure-Selectivity Correlations in the Electrochemical Reduction of CO<sub>2</sub>: A Comparison of Well-Ordered Atomically Clean and Chemically Etched Copper Single-Crystal Surfaces, *Angew. Chem., Int. Ed.*, 2021, **60**, 19169–19175.
- 174 C. Choi, S. Kwon, T. Cheng, M. Xu, P. Tieu, C. Lee, J. Cai, H. M. Lee, X. Pan, X. Duan, W. A. Goddard and Y. Huang, Highly active and stable stepped Cu surface for enhanced electrochemical CO<sub>2</sub> reduction to C<sub>2</sub>H<sub>4</sub>, *Nat. Catal.*, 2020, **3**, 804–812.
- 175 M. Song, Z. Jiao, W. Jing, Y. Liu and L. Guo, Revealing the Nature of C-C Coupling Sites on a Cu Surface for CO<sub>2</sub> Reduction, *J. Phys. Chem. Lett.*, 2022, **13**, 4434–4440.
- 176 G. Jiang, D. Han, Z. Han, J. Gao, X. Wang, Z. Weng and Q.-H. Yang, Rational Manipulation of Intermediates on Copper for CO<sub>2</sub> Electroreduction Toward Multicarbon Products, *Trans. Tianjin Univ.*, 2022, **28**, 265–291.
- 177 Z. Ni, P. Wang, F. Quan, R. Guo, C. Liu, X. Liu, W. Mu, X. Lei and Q. Li, Design strategy of a Cu-based catalyst for optimizing the performance in the electrochemical CO<sub>2</sub> reduction reaction to multicarbon alcohols, *Nanoscale*, 2022, **14**, 16376–16393.
- 178 Z. Gu, H. Shen, Z. Chen, Y. Yang, C. Yang, Y. Ji, Y. Wang, C. Zhu, J. Liu, J. Li, T.-K. Sham, X. Xu and G. Zheng, Efficient Electrocatalytic CO<sub>2</sub> Reduction to C<sub>2</sub><sup>+</sup> Alcohols at Defect-Site-Rich Cu Surface, *Joule*, 2021, **5**, 429–440.
- 179 R. M. Arán-Ais, F. Scholten, S. Kunze, R. Rizo and B. Roldan Cuenya, The role of in situ generated morphological motifs and Cu(i) species in C<sub>2</sub><sup>+</sup> product selectivity during CO<sub>2</sub> pulsed electroreduction, *Nat. Energy*, 2020, **5**, 317–325.
- 180 S. Chu, C. Kang, W. Park, Y. Han, S. Hong, L. Hao, H. Zhang, T. W. B. Lo, A. W. Robertson, Y. Jung, B. Han and Z. Sun, Single atom and defect engineering of CuO for efficient electrochemical reduction of CO<sub>2</sub> to C<sub>2</sub>H<sub>4</sub>, *SmartMat*, 2022, **3**, 194–205.



- 181 T. Kim and G. T. R. Palmore, A scalable method for preparing Cu electrocatalysts that convert CO<sub>2</sub> into C<sub>2</sub>+ products, *Nat. Commun.*, 2020, **11**, 3622.
- 182 A. Walsh, A. A. Sokol, J. Buckeridge, D. O. Scanlon and C. R. A. Catlow, Oxidation states and ionicity, *Nat. Mater.*, 2018, **17**, 958–964.
- 183 D. Wang, L. Li, Q. Xia, S. Hong, L. Hao, A. W. Robertson and Z. Sun, Boosting CO<sub>2</sub> Electroreduction to Multicarbon Products via Tuning of the Copper Surface Charge, *ACS Sustain. Chem. Eng.*, 2022, **10**, 11451–11458.
- 184 N. Hongrutai, S. Watmanee, P. Pinthong and J. Panpranot, Electrochemical reduction of carbon dioxide on the oxide-containing electrocatalysts, *J. CO<sub>2</sub> Util.*, 2022, **64**, 102194.
- 185 G. Liu, P. Adesina, N. Nasiri, H. Wang, Y. Sheng, S. Wu, M. Kraft, A. A. Lapkin, J. W. Ager and R. Xu, Elucidating Reaction Pathways of the CO<sub>2</sub> Electroreduction via Tailorable Tortuosities and Oxidation States of Cu Nanostructures, *Adv. Funct. Mater.*, 2022, **32**, 2204993.
- 186 C. W. Li and M. W. Kanan, CO<sub>2</sub> Reduction at Low Overpotential on Cu Electrodes Resulting from the Reduction of Thick Cu<sub>2</sub>O Films, *J. Am. Chem. Soc.*, 2012, **134**, 7231–7234.
- 187 H. Mistry, A. S. Varela, C. S. Bonifacio, I. Zegkinoglou, I. Sinev, Y.-W. Choi, K. Kisslinger, E. A. Stach, J. C. Yang, P. Strasser and B. R. Cuenya, Highly selective plasma-activated copper catalysts for carbon dioxide reduction to ethylene, *Nat. Commun.*, 2016, **7**, 12123.
- 188 C. Kim, K. M. Cho, K. Park, J. Y. Kim, G.-T. Yun, F. M. Toma, I. Gereige and H.-T. Jung, Cu/Cu<sub>2</sub>O Interconnected Porous Aerogel Catalyst for Highly Productive Electrosynthesis of Ethanol from CO<sub>2</sub>, *Adv. Funct. Mater.*, 2021, **31**, 2102142.
- 189 W. Zhang, C. Huang, Q. Xiao, L. Yu, L. Shuai, P. An, J. Zhang, M. Qiu, Z. Ren and Y. Yu, Atypical Oxygen-Bearing Copper Boosts Ethylene Selectivity toward Electrocatalytic CO<sub>2</sub> Reduction, *J. Am. Chem. Soc.*, 2020, **142**, 11417–11427.
- 190 J. Jiao, R. Lin, S. Liu, W.-C. Cheong, C. Zhang, Z. Chen, Y. Pan, J. Tang, K. Wu, S.-F. Hung, H. M. Chen, L. Zheng, Q. Lu, X. Yang, B. Xu, H. Xiao, J. Li, D. Wang, Q. Peng, C. Chen and Y. Li, Copper atom-pair catalyst anchored on alloy nanowires for selective and efficient electrochemical reduction of CO<sub>2</sub>, *Nat. Chem.*, 2019, **11**, 222–228.
- 191 J. Lan, T. Liao, T. Zhang and L. W. Chung, Reaction Mechanism of Cu(I)-Mediated Reductive CO<sub>2</sub> Coupling for the Selective Formation of Oxalate: Cooperative CO<sub>2</sub> Reduction To Give Mixed-Valence Cu<sub>2</sub>(CO<sub>2</sub>•<sup>-</sup>) and Nucleophilic-Like Attack, *Inorg. Chem.*, 2017, **56**, 6809–6819.
- 192 J. Wang, H.-C. Chen, H.-Y. Tan, C. M. Tan, Y. Zhu and H. M. Chen, Strong Correlation between the Dynamic Chemical State and Product Profile of Carbon Dioxide Electroreduction, *ACS Appl. Mater. Interfaces*, 2022, **14**, 22681–22696.
- 193 Z.-Z. Wu, F.-Y. Gao and M.-R. Gao, Regulating the oxidation state of nanomaterials for electrocatalytic CO<sub>2</sub> reduction, *Energy Environ. Sci.*, 2021, **14**, 1121–1139.
- 194 C. Liu, M. P. Lourenço, S. Hedström, F. Cavalca, O. Diaz-Morales, H. A. Duarte, A. Nilsson and L. G. M. Pettersson, Stability and Effects of Subsurface Oxygen in Oxide-Derived Cu Catalyst for CO<sub>2</sub> Reduction, *J. Phys. Chem. C*, 2017, **121**, 25010–25017.
- 195 J. Wang, Y. Chen, S. Zhang, C. Yang, J.-Y. Zhang, Y. Su, G. Zheng and X. Fang, Controllable States and Porosity of Cu-Carbon for CO<sub>2</sub> Electroreduction to Hydrocarbons, *Small*, 2022, **18**, 2202238.
- 196 S. Mu, H. Lu, Q. Wu, L. Li, R. Zhao, C. Long and C. Cui, Hydroxyl radicals dominate reoxidation of oxide-derived Cu in electrochemical CO<sub>2</sub> reduction, *Nat. Commun.*, 2022, **13**, 3694.
- 197 D. Tan, J. Zhang, L. Yao, X. Tan, X. Cheng, Q. Wan, B. Han, L. Zheng and J. Zhang, Multi-shelled CuO microboxes for carbon dioxide reduction to ethylene, *Nano Res.*, 2020, **13**, 768–774.
- 198 M. Suominen and T. Kallio, What We Currently Know about Carbon-Supported Metal and Metal Oxide Nanomaterials in Electrochemical CO<sub>2</sub> Reduction, *ChemElectroChem*, 2021, **8**, 2397–2406.
- 199 I. C. Gerber and P. Serp, A Theory/Experience Description of Support Effects in Carbon-Supported Catalysts, *Chem. Rev.*, 2020, **120**, 1250–1349.
- 200 M. Ding, Y. Tang and A. Star, Understanding Interfaces in Metal-Graphitic Hybrid Nanostructures, *J. Phys. Chem. Lett.*, 2013, **4**, 147–160.
- 201 P. Grosse, D. Gao, F. Scholten, I. Sinev, H. Mistry and B. Roldan Cuenya, Dynamic Changes in the Structure, Chemical State and Catalytic Selectivity of Cu Nanocubes during CO<sub>2</sub> Electroreduction: Size and Support Effects, *Angew. Chem., Int. Ed.*, 2018, **57**, 6192–6197.
- 202 N. Hussain, M. A. Abdelkareem, H. Alawadhi, K. Elsaid and A. G. Olabi, Synthesis of Cu-g-C<sub>3</sub>N<sub>4</sub>/MoS<sub>2</sub> composite as a catalyst for electrochemical CO<sub>2</sub> reduction to alcohols, *Chem. Eng. Sci.*, 2022, **258**, 117757.
- 203 A. Anzai, M.-H. Liu, K. Ura, T. G. Noguchi, A. Yoshizawa, K. Kato, T. Sugiyama and M. Yamauchi, Cu Modified TiO<sub>2</sub> Catalyst for Electrochemical Reduction of Carbon Dioxide to Methane, *Catalysts*, 2022, **12**, 478.
- 204 S. Gong, X. Xiao, W. Wang, D. K. Sam, R. Lu, Y. Xu, J. Liu, C. Wu and X. Lv, Silk fibroin-derived carbon aerogels embedded with copper nanoparticles for efficient electrocatalytic CO<sub>2</sub>-to-CO conversion, *J. Colloid Interface Sci.*, 2021, **600**, 412–420.
- 205 H. Han, Y. Noh, Y. Kim, S. Park, W. Yoon, D. Jang, S. M. Choi and W. B. Kim, Selective electrochemical CO<sub>2</sub> conversion to multicarbon alcohols on highly efficient N-doped porous carbon-supported Cu catalysts, *Green Chem.*, 2020, **22**, 71–84.
- 206 L. Ma, W. Hu, B. Mei, H. Liu, B. Yuan, J. Zang, T. Chen, L. Zou, Z. Zou, B. Yang, Y. Yu, J. Ma, Z. Jiang, K. Wen and H. Yang, Covalent Triazine Framework Confined Copper Catalysts for Selective Electrochemical CO<sub>2</sub> Reduction: Operando Diagnosis of Active Sites, *ACS Catal.*, 2020, **10**, 4534–4542.
- 207 S. Zhang, S. Zhao, D. Qu, X. Liu, Y. Wu, Y. Chen and W. Huang, Electrochemical Reduction of CO<sub>2</sub> Toward C<sub>2</sub> Valuables on Cu@Ag Core-Shell Tandem Catalyst with Tunable Shell Thickness, *Small*, 2021, **17**, 2102293.



- 208 C. G. Morales-Guio, E. R. Cave, S. A. Nitopi, J. T. Feaster, L. Wang, K. P. Kuhl, A. Jackson, N. C. Johnson, D. N. Abram, T. Hatsukade, C. Hahn and T. F. Jaramillo, Improved CO<sub>2</sub> reduction activity towards C<sub>2</sub><sup>+</sup> alcohols on a tandem gold on copper electrocatalyst, *Nat. Catal.*, 2018, **1**, 764–771.
- 209 T. Zhang, J. C. Bui, Z. Li, A. T. Bell, A. Z. Weber and J. Wu, Highly selective and productive reduction of carbon dioxide to multicarbon products via in situ CO management using segmented tandem electrodes, *Nat. Catal.*, 2022, **5**, 202–211.
- 210 D.-H. Nam, P. De Luna, A. Rosas-Hernández, A. Thevenon, F. Li, T. Agapie, J. C. Peters, O. Shekhah, M. Eddaoudi and E. H. Sargent, Molecular enhancement of heterogeneous CO<sub>2</sub> reduction, *Nat. Mater.*, 2020, **19**, 266–276.
- 211 X. Wei, Z. Yin, K. Lyu, Z. Li, J. Gong, G. Wang, L. Xiao, J. Lu and L. Zhuang, Highly Selective Reduction of CO<sub>2</sub> to C<sub>2</sub><sup>+</sup> Hydrocarbons at Copper/Polyaniline Interfaces, *ACS Catal.*, 2020, **10**, 4103–4111.
- 212 F. Li, Y. C. Li, Z. Wang, J. Li, D.-H. Nam, Y. Lum, M. Luo, X. Wang, A. Ozden, S.-F. Hung, B. Chen, Y. Wang, J. Wicks, Y. Xu, Y. Li, C. M. Gabardo, C.-T. Dinh, Y. Wang, T.-T. Zhuang, D. Sinton and E. H. Sargent, Cooperative CO<sub>2</sub>-to-ethanol conversion via enriched intermediates at molecule–metal catalyst interfaces, *Nat. Catal.*, 2020, **3**, 75–82.
- 213 Y. Wang, J. Zhao, C. Cao, J. Ding, R. Wang, J. Zeng, J. Bao and B. Liu, Amino-Functionalized Cu for Efficient Electrochemical Reduction of CO to Acetate, *ACS Catal.*, 2023, **13**, 3532–3540.
- 214 K. Zhang, J. Xu, T. Yan, L. Jia, J. Zhang, C. Shao, L. Zhang, N. Han and Y. Li, Molecular Modulation of Sequestered Copper Sites for Efficient Electroreduction of Carbon Dioxide to Methane, *Adv. Funct. Mater.*, 2023, **33**, 2214062.
- 215 C. Zhan, F. Dattila, C. Rettenmaier, A. Bergmann, S. Köhl, R. García-Muelas, N. López and B. R. Cuenya, Revealing the CO Coverage-Driven C–C Coupling Mechanism for Electrochemical CO<sub>2</sub> Reduction on Cu<sub>2</sub>O Nanocubes via Operando Raman Spectroscopy, *ACS Catal.*, 2021, **11**, 7694–7701.
- 216 X. Wang, A. Xu, F. Li, S.-F. Hung, D.-H. Nam, C. M. Gabardo, Z. Wang, Y. Xu, A. Ozden, A. S. Rasouli, A. H. Ip, D. Sinton and E. H. Sargent, Efficient Methane Electrosynthesis Enabled by Tuning Local CO<sub>2</sub> Availability, *J. Am. Chem. Soc.*, 2020, **142**, 3525–3531.
- 217 Y. Sha, J. Zhang, X. Cheng, M. Xu, Z. Su, Y. Wang, J. Hu, B. Han and L. Zheng, Anchoring Ionic Liquid in Copper Electrocatalyst for Improving CO<sub>2</sub> Conversion to Ethylene, *Angew. Chem., Int. Ed.*, 2022, **61**, e202200039.
- 218 Z. Han, D. Han, Z. Chen, J. Gao, G. Jiang, X. Wang, S. Lyu, Y. Guo, C. Geng, L. Yin, Z. Weng and Q.-H. Yang, Steering surface reconstruction of copper with electrolyte additives for CO<sub>2</sub> electroreduction, *Nat. Commun.*, 2022, **13**, 3158.
- 219 P. B. Joshi, N. Karki and A. J. Wilson, Electrocatalytic CO<sub>2</sub> Reduction in Acetonitrile Enhanced by the Local Environment and Mass Transport of H<sub>2</sub>O, *ACS Energy Lett.*, 2022, **7**, 602–609.
- 220 C.-T. Dinh, T. Burdyny, M. G. Kibria, A. Seifitokaldani, C. M. Gabardo, F. P. García de Arquer, A. Kiani, J. P. Edwards, P. De Luna, O. S. Bushuyev, C. Zou, R. Quintero-Bermudez, Y. Pang, D. Sinton and E. H. Sargent, CO<sub>2</sub> electroreduction to ethylene via hydroxide-mediated copper catalysis at an abrupt interface, *Science*, 2018, **360**, 783–787.
- 221 Z. Ma, Z. Yang, W. Lai, Q. Wang, Y. Qiao, H. Tao, C. Lian, M. Liu, C. Ma, A. Pan and H. Huang, CO<sub>2</sub> electroreduction to multicarbon products in strongly acidic electrolyte via synergistically modulating the local microenvironment, *Nat. Commun.*, 2022, **13**, 7596.
- 222 X. Zi, Y. Zhou, L. Zhu, Q. Chen, Y. Tan, X. Wang, M. Sayed, E. Pensa, R. A. Geioushy, K. Liu, J. Fu, E. Cortés and M. Liu, Breaking K<sup>+</sup> Concentration Limit on Cu Nanoneedles for Acidic Electrocatalytic CO<sub>2</sub> Reduction to Multi-Carbon Products, *Angew. Chem., Int. Ed.*, 2023, **62**, e202309351.
- 223 X. Zhang, X. Sun, S.-X. Guo, A. M. Bond and J. Zhang, Formation of lattice-dislocated bismuth nanowires on copper foam for enhanced electrocatalytic CO<sub>2</sub> reduction at low overpotential, *Energy Environ. Sci.*, 2019, **12**, 1334–1340.
- 224 W. Xiong, D. Si, J. Yi, Y. Huang, H. Li and R. Cao, Morphology and composition dependence of multicomponent Cu-based nanoreactor for tandem electrocatalysis CO<sub>2</sub> reduction, *Appl. Catal., B*, 2022, **314**, 121498.
- 225 P. Li, J. Bi, J. Liu, Q. Zhu, C. Chen, X. Sun, J. Zhang and B. Han, In situ dual doping for constructing efficient CO<sub>2</sub>-to-methanol electrocatalysts, *Nat. Commun.*, 2022, **13**, 1965.
- 226 P.-C. Chen, C. Chen, Y. Yang, A. L. Maulana, J. Jin, J. Feijoo and P. Yang, Chemical and Structural Evolution of AgCu Catalysts in Electrochemical CO<sub>2</sub> Reduction, *J. Am. Chem. Soc.*, 2023, **145**, 10116–10125.
- 227 J. Feijoo, Y. Yang, M. V. Fonseca Guzman, A. Vargas, C. Chen, C. J. Pollock and P. Yang, Operando High-Energy-Resolution X-ray Spectroscopy of Evolving Cu Nanoparticle Electrocatalysts for CO<sub>2</sub> Reduction, *J. Am. Chem. Soc.*, 2023, **145**, 20208–20213.
- 228 X. Wang, P. Ou, J. Wicks, Y. Xie, Y. Wang, J. Li, J. Tam, D. Ren, J. Y. Howe, Z. Wang, A. Ozden, Y. Z. Finfrock, Y. Xu, Y. Li, A. S. Rasouli, K. Bertens, A. H. Ip, M. Graetzel, D. Sinton and E. H. Sargent, Gold-in-copper at low \*CO coverage enables efficient electromethanation of CO<sub>2</sub>, *Nat. Commun.*, 2021, **12**, 3387.
- 229 H. Song, J. T. Song, B. Kim, Y. C. Tan and J. Oh, Activation of C<sub>2</sub>H<sub>4</sub> reaction pathways in electrochemical CO<sub>2</sub> reduction under low CO<sub>2</sub> partial pressure, *Appl. Catal., B*, 2020, **272**, 119049.
- 230 Y. Xu, J. P. Edwards, J. Zhong, C. P. O'Brien, C. M. Gabardo, C. McCallum, J. Li, C.-T. Dinh, E. H. Sargent and D. Sinton, Oxygen-tolerant electroproduction of C<sub>2</sub> products from simulated flue gas, *Energy Environ. Sci.*, 2020, **13**, 554–561.
- 231 M. Schreier, Y. Yoon, M. N. Jackson and Y. Surendranath, Competition between H and CO for Active Sites Governs Copper-Mediated Electrosynthesis of Hydrocarbon Fuels, *Angew. Chem., Int. Ed.*, 2018, **57**, 10221–10225.

